DOCTORAL DISSERTATION
博士論文

Current-spin conversion in Dirac semimetal thin film heterostructures (ディラック半金属薄膜ヘテロ構造における電流-スピン流変換)

A Dissertation Submitted for the Degree of
Doctor of Philosophy, December 2020
令和2年12月博士(理学)申請

Department of Physics, Graduate School of Science, The University of Tokyo
東京大学大学院理学系研究科 物理学専攻

CHI ZHENDONG
池震棟

Abstract

Current-induced spin-transfer torque (STT) is an effective method to control the magnetization of ferromagnetic metal (FM) thin films by the current, paving the way for designing spintronic devices with low power consumption, fast speed, and high density. Recently, a new type of current-induced torque has been observed in heavy metal (HM)/FM and topological insulator (TI)/FM thin film heterostructures. The torque, known as spin-orbit torque (SOT), is of particular interest owing to the high efficiency in manipulating the magnetization of FM layers. The SOT is attributed to current-induced spin accumulations at the interface of HM/FM and TI/FM heterostructures, which originates from the spin Hall effect (SHE) and/or the Rashba-Edelstein effect (REE). Therefore, identifying materials with considerable current-spin conversion efficiency and clarifying their origin are critical to developing our understanding on these materials and realizing efficient current-induced SOT for application.

In this thesis, I present current-spin conversion in Bi-based material thin films by characterizing the current-induced SOT using Bi-based material/FM thin film heterostructures. An alternating ultrathin layer deposition (AULD) method is proposed to grow Bi-based alloy with controllable concentration. First, I demonstrate appreciable current-spin conversion efficiency, exceeding an unity, in polycrystalline $Bi_{1-x}Sb_x$ alloy thin films. The $Bi_{1-x}Sb_x$ thickness, composition, and facet orientation dependences of the spin Hall conductivity (SHC) of the alloy indicate large current-spin conversion is primarily due to the intrinsic SHE in $Bi_{1-x}Sb_x$. The topological surface state of $Bi_{1-x}Sb_x$, if present, plays little role in current-spin conversion. Strikingly, the SHC of $Bi_{1-x}Sb_x$ increases markedly with temperature, following the temperature dependence of carrier density. Based on an analysis of spin current mobility, we suggest the thermally-excited massive Dirac electrons at the L-valley significantly contribute to this enhancement.

Second, I show the investigation on current-induced SOT in carrier-doped Bi/CoFeB thin film heterostructures to highlight the importance of massive Dirac carriers, including electrons and holes, to current-spin conversion. The Fermi level positioning is tunable by substituting Bi with Te and Sn. The current-spin conversion efficiency of pristine Bi is found to reach ~ 2.7, which is the largest spin Hall angle detected so far. It is found that the SHC of Bi exhibits a plateau when the Fermi level is close to the Dirac point. Subsequently, the value drops dramatically with increasing electron and hole doping

induced by Te and Sn substitution. The SHC of Bi is also demonstrated to be robust against the change of Bi thin film crystallographic orientation and resistivity. These results indicate the current-spin conversion of Bi, dominated by the intrinsic SHE, is correlated with the Fermi level positioning.

Third, I introduce the study on the structure, magnetic anisotropy and current-spin conversion in $Pt_{1-x}Bi_x$/Co/MgO trilayer systems. Bi atoms behave as impurities in the Pt host and the magnetic easy axis of an ultrathin Co layer in the trilayer points out-of-plane when the doping level x is smaller than ~ 0.5. $Pt_{1-x}Bi_x$ thin film converts to a Pt-$PtBi_2$ mixture for x beyond ~ 0.6. In this regime, the easy axis of the ultrathin Co layer changes from out-of-plane to in-plane. The resistivity of Pt-rich $Pt_{1-x}Bi_x$ increases with doping, whereas the SHC is hardly influenced by x. These results suggest Bi doping is an effective strategy to enhance the current-spin conversion efficiency of Pt.

These studies provide the first experimental evidence that Dirac-like electronic band structure, which contains non-zero Berry curvature, is strongly correlated to the SHE. The findings advance understanding on the current-spin conversion process on Dirac materials and open pathways to develop material systems that allow generation of significant spin current.

List of abbreviations

AC Alternative current
AHE Anomalous Hall effect
ANE Anomalous Nernst effect
ARPES Angle-resolved photoemission spectroscopy
AULD Alternating ultrathin layer deposition
DC Direct current
DL-SOT Damping-like spin-orbit torque
FL-SHC Field-like spin Hall conductivity
FL-SOT Field-like spin-orbit torque
FM Ferromagnetic metal
HAADF-STEM High-angle annular dark-field scanning transmission electron microscopy
HM Heavy metal
IMA In-plane magnetic anisotropy
ISHE Inverse spin Hall effect
LLG Landau-Lifshitz-Gilbert
MBE Molecular beam epitaxy
MRAM Magnetic random access memory
NM Normal metal
ONE Ordinary Nernst effect
PHE Planar Hall effect
PMA Perpendicular magnetic anisotropy
REE Rashba-Edelstein effect
RF Radio frequency
SHC Spin Hall conductivity
SHE Spin Hall effect
SOT Spin-orbit torque
SSE Spin Seebeck effect
STT Spin-transfer torque
TI Topological insulator
TSS Topological surface state

VSM	Vibrating sample magnetometer
XRD	X-ray diffraction

Contents

List of abbreviations

1 Introduction 1
1.1 Spin transfer torque . . . 1
1.2 Spin-orbit torque . . . 4
1.2.1 Heavy metal/ferromagnetic metal heterostructures . . . 4
1.2.2 Topological insulator/ferromagnetic metal heterostructures . . . 10
1.3 Bismuth and the alloy . . . 13
1.3.1 Bismuth . . . 14
1.3.2 Bismuth-antimony alloy . . . 16
1.4 Objective and outlines of this thesis . . . 19

2 Experimental methods 21
2.1 Radio frequency mangetron sputtering thin film deposition . . . 21
2.2 X-ray diffraction . . . 23
2.3 Vibrating sample magnetometer measurement . . . 23
2.4 Device fabrication . . . 24
2.5 Direct current transport measurement . . . 27
2.6 Harmonic Hall resistance technique . . . 30
2.6.1 In-plane magnetization system . . . 33
2.6.2 Out-of-plane magnetization system . . . 35

3 Current-spin conversion in BiSb alloy thin films 37
3.1 Introduction . . . 37
3.2 Sample description . . . 38
3.3 Structural and magnetization characterization . . . 38
3.4 Current-spin conversion characterization . . . 42
3.4.1 BiSb thickness dependence . . . 43
3.4.2 BiSb composition dependence . . . 49
3.4.3 Facet dependence . . . 52

3.4.4 Temperature dependence 53
3.5 Discussion 59
3.6 Conclusion 62

4 Current-spin conversion in carrier-doped Bi thin films 65
4.1 Introduction 65
4.2 Sample description 66
4.3 Structure and magnetization characterization 67
4.4 Direct current transport measurement 69
4.5 Current-spin conversion characterization 72
4.6 Discussion 77
4.6.1 Robustness of SHC in Bi 77
4.6.2 Current-spin conversion in Te-rich $Bi_{1-x}Te_x$ thin films . . 79
4.7 Conclusion 81

5 Structure, magnetic anisotropy and current-spin conversion in $Pt_{1-x}Bi_x$/Co/MgO trilayers 83
5.1 Introduction 83
5.2 Sample description 84
5.3 Structural characterization 84
5.4 Magnetic properties 85
5.5 Current-spin conversion characterization 86
5.6 Conclusion 92

6 Summary & Outlook 93

Acknowledgments

List of publications

References

Chapter 1

Introduction

1.1 Spin transfer torque

Spintronics is a field that studies the role of electron spin degree of freedom plays in solid-state physics. The discovery of the giant magnetoresistance at the end of the 1980s [1, 2] is considered the beginning of this field. In giant magnetoresistance, the resistance of a ferromagnetic metal (FM)/non-magnetic metal (NM)/FM structure, often referred to as a spin valve, is lower when the magnetizations of the two FM layers are parallel compared to the antiparallel alignment. Similar to giant magnetoresistance, the tunneling resistance in FM/insulator/FM magnetic tunnel junction also depends on the magnetization alignment, an effect referred to the tunneling magnetoresistance. The two magnetic states of the FM layers in spin valve and magnetic tunnel junction are tunable by applying a magnetic field and they can serve as binary information. Therefore, the spin valve and magnetic tunnel junction are regarded as promising candidates for realizing magnetic random access memory (MRAM): the next-generation non-volatile memory for replacing silicon-based devices. However, the need of a magnetic field to control the magnetization configurations in spin valve or magnetic tunnel junction is an issue for device integration since it requires large current, resulting in high power consumption.

To address this issue, current-induced spin-transfer torque (STT) has been proposed to control the magnetization of FM thin films. Before describing STT in detail, the concept of spin current is introduced first. Electrons in conductors can be driven by electric field due to Fermi level shift, resulting in a flow of electrons, i.e., the current. An electron spin is an intrinsic form of angular momentum and contains two intrinsic states: up spin (↑) and down spin (↓). Based on the two-channel model, the flow of electrons can be divided into two components, defined as $\boldsymbol{j}_\uparrow$ and $\boldsymbol{j}_\downarrow$. If a difference in the magnitude exists in these components, a net spin angular momentum will be transferred

by the current. Such current is called a spin current. Thus, spin current $\boldsymbol{j}_\mathrm{s}$ and current $\boldsymbol{j}_\mathrm{c}$ can be written as

$$\boldsymbol{j}_\mathrm{s} = \boldsymbol{j}_\uparrow - \boldsymbol{j}_\downarrow;\ \boldsymbol{j}_\mathrm{c} = \boldsymbol{j}_\uparrow + \boldsymbol{j}_\downarrow. \tag{1.1}$$

In general, $\boldsymbol{j}_\uparrow$ and $\boldsymbol{j}_\downarrow$ take the same flowing direction and $\boldsymbol{j}_\mathrm{s}$ is referred to as spin-polarized current. A special situation occurs when $\boldsymbol{j}_\uparrow$ and $\boldsymbol{j}_\downarrow$ own opposite flowing directions. If their magnitudes are equal to each other, $\boldsymbol{j}_\mathrm{c}$ will disappear and $\boldsymbol{j}_\mathrm{s}$ is equal to $2\boldsymbol{j}_{\uparrow(\downarrow)}$. Spin current is such case is referred to as pure spin current.

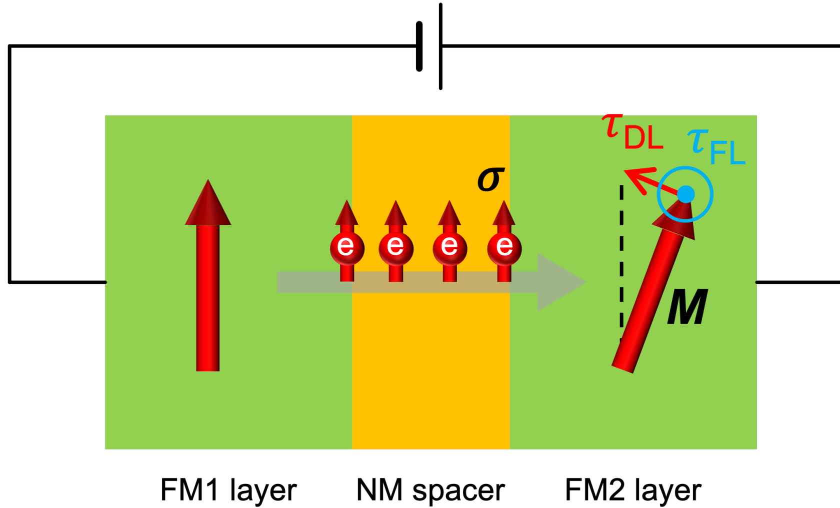

Figure 1.1: Schematic illustration of the spin-transfer torque in FM/NM/FM structure.

The schematic of STT is illustrated in Fig. 1.1, where FM/NM/FM trilayer is used as an example. A flow of electron with non-zero spin polarization, i.e., a spin-polarized current, is transferred from FM1 layer to FM2 layer and accumulated in FM2 layer after crossing the NM spacer by an electric field perpendicular to the plane of the structure. The spin polarization unit vector is $\boldsymbol{\sigma}$. Considering that $\boldsymbol{\sigma}$ is not parallel with the local moment $\boldsymbol{M}$ in the FM2 layer, it will be rotated to form a collinear state with $\boldsymbol{M}$ due to s-d interaction. As a counteraction, a torque will be transferred from the electron to $\boldsymbol{M}$ and control the direction of $\boldsymbol{M}$, which is defined as STT.

Slonczewski [3] and Berger [4] first predicted STT in 1996. Later, Zhang *et al.* pointed out that two components, an adiabatic damping-like torque

τ_{DL} and a non-adiabatic field-like torque τ_{FL}, contribute to the STT [5]. The dynamics of $\boldsymbol{M}$ can be described by adding the STT terms into the Landau-Lifshitz-Gilbert (LLG) equation, which reads as

$$\frac{\partial \boldsymbol{m}}{\partial t} = -\gamma \boldsymbol{m} \times \boldsymbol{H}_{\mathrm{eff}} + \alpha \boldsymbol{m} \times \frac{\partial \boldsymbol{m}}{\partial t} - \tau_{\mathrm{DL}} \cdot (\boldsymbol{m} \times (\boldsymbol{\sigma} \times \boldsymbol{m})) - \tau_{\mathrm{FL}} \cdot (\boldsymbol{m} \times \boldsymbol{\sigma}), \tag{1.2}$$

where γ is the gyromagnetic ratio, $\boldsymbol{m} = \boldsymbol{M}/M_{\mathrm{s}}$ is the unit vector of $\boldsymbol{M}$, M_{s} is the saturation magnetization of $\boldsymbol{M}$, $\boldsymbol{H}_{\mathrm{eff}}$ is the effective field including external, demagnetizing and exchange contributions, α is the Gilbert damping constant, τ_{DL} and τ_{FL} are the damping-like and field-like torque terms, respectively. The first term on the right side of the equation is used to describe the Lamor procession of $\boldsymbol{m}$ around $\boldsymbol{H}_{\mathrm{eff}}$. The second term is the Gilbert damping torque for relaxing $\boldsymbol{m}$, driving it towards $\boldsymbol{H}_{\mathrm{ext}}$. The third and fourth terms are damping-like and field-like torques, respectively. The directions of these two torques are illustrated in Fig. 1.1. The two STT terms can be merged with the first one in the equation. It gives an effective field description of STT, $\boldsymbol{H}_{\mathrm{DL}}$ and $\boldsymbol{H}_{\mathrm{FL}}$, which read as

$$\boldsymbol{H}_{\mathrm{DL}} = H_{\mathrm{DL}}(\boldsymbol{\sigma} \times \boldsymbol{m}),\ \ \boldsymbol{H}_{\mathrm{FL}} = H_{\mathrm{FL}}\boldsymbol{\sigma}, \tag{1.3}$$

where H_{DL} and H_{FL} are the magnitudes of effective fields induced by damping-like torque and field-like torque, respectively, and defined as $H_{\mathrm{DL}} = \tau_{\mathrm{DL}}/\gamma$ and $H_{\mathrm{FL}} = \tau_{\mathrm{FL}}/\gamma$.

The trajectories of the magnetization with STT is illustrated in Fig. 1.2 [6]. Beyond a critical current, the magnetization can undergo steady procession or reversal. Magnetization switching has been observed in FM/NM/FM structures where the FM layer exhibits in-plane (IMA) or perpendicular magnetic anisotropy (PMA) [7, 8]. Therefore, STT can solve the problem for MRAM applications where a magnetic field is no longer necessary to write information. In the macrospin model, the critical current I_{critical} for switching the magnetization of FM layer in FM/NM/FM structures reads as [9]

$$I_{\mathrm{critical,STT}} = \frac{2e}{\hbar}\frac{\alpha\mu_0 M_{\mathrm{s}} V}{\eta} H_{\mathrm{eff}}, \tag{1.4}$$

where e is the elementary charge, $\hbar$ is the reduced Planck constant, V is the volume of the STT device, μ_0 is the vacuum permeability, and η is the efficiency of damping-like torque. One can find that $I_{\mathrm{critical,STT}}$ decreases with decreasing the device size. It suggests that the energy consumption for switching the magnetization by current-induced STT is lower for smaller devices, suitable for very large scale integration.

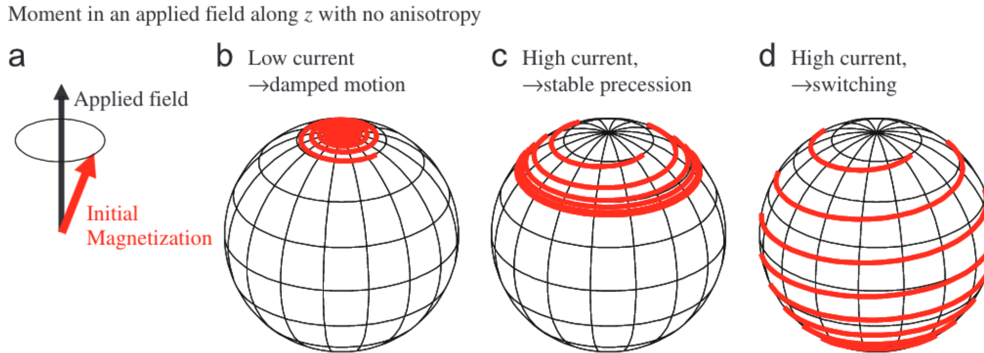

Figure 1.2: Trajectories of magnetization driven by the spin-transfer torque in its dynamics. (a) The initial configuration of the magnetization under an applied magnetic field along the z-axis. There is a small misalignment between the magnetization orientation and the magnetic field. (b) For currents below a threshold, the magnetization spirals back toward the z-axis because of damping. (c,d) For currents beyond a threshold, the damping becomes negative due to its cancellation by STT. It can result in a steady procession (c) or magnetization reversal (d). The figure is extracted from Ref. [6].

Another important application of STT is current-induced magnetic domain wall motion in FM nanowires. In the case of FM/NM/FM structures, the magnetic misalignment of the two FM layers, i.e., a nonuniform magnetic configuration, is significant for realizing STT-induced magnetization switching. Domain wall, as the boundaries connecting magnetic domains with different orientations, is a typical texture with magnetic misalignment in spatial. Different experimental methods have been employed to observe domain wall motion in FM nanowires, e.g., magneto-optical Kerr effect magnetometer [10,11], magnetic force microscopy [12], anomalous Hall effect (AHE) [13,14], and nanowire resistance measurement [15]. Current-induced domain wall motion is considered as for another type of information storage memory device, known as the magnetic racetrack memory [16].

1.2 Spin-orbit torque

1.2.1 Heavy metal/ferromagnetic metal heterostructures

Besides STT, significant effort has been put to look for new types of current-induced torque using different materials. The spin Hall effect (SHE) [17] in heavy metal (HM) allows conversion of charge current to pure spin current.

Similar to the spin-polarized current, pure spin current from HM due to the SHE can exert a torque on the magnetization in HM/FM heterostructures. Because of the spin-orbit coupling origin of the SHE, such torque is referred to as spin-orbit torque (SOT). The basic concepts of the SHE and the SOT induced by the SHE in HM/FM heterostructures will be described here.

SHE and its reciprocal effect, the inverse spin Hall effect (ISHE), are schematically illustrated in Fig. 1.3. Dyakonov and Perel first proposed SHE in 1971 [18] and it was reformulated in 1999 [19]. In SHE, a charge current in non-magnetic material with spin-orbit coupling generates a transverse pure spin current polarized perpendicular to the plane defined by the charge and pure spin current. In ISHE, a charge current can be induced orthogonally by a pure spin current.

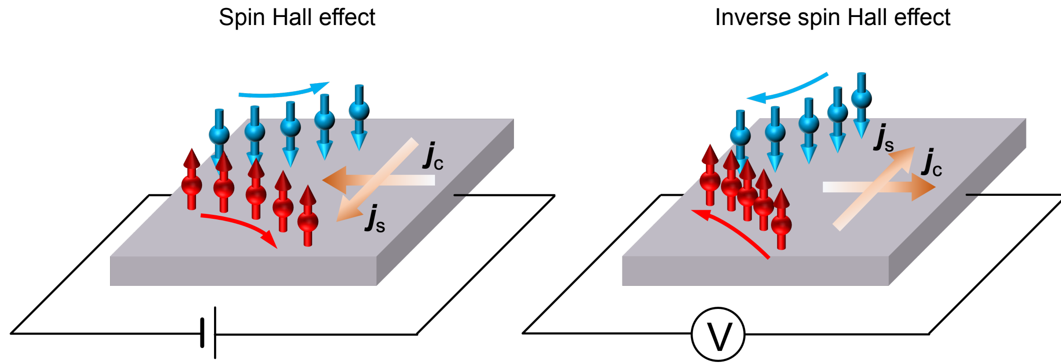

Figure 1.3: Schematic illustration of spin Hall effect and inverse spin Hall effect.

The figure of merit used to describe current-spin conversion in SHE is the spin Hall angle θ_{SH}, which reads as

$$\theta_{\mathrm{SH}} = \frac{2e}{\hbar}\frac{\sigma_{\mathrm{SH}}}{\sigma_{xx}}. \tag{1.5}$$

where σ_{xx} is the conductivity of NM and σ_{SH} is the spin Hall conductivity (SHC). The prefactor $2e/\hbar$ is used to set θ_{SH} as a dimensionless quantity. σ_{SH} represents the conductivity of transverse spin current. In terms of spin current, Eq. 1.5 cab be rewritten as

$$\theta_{\mathrm{SH}} = \frac{2e}{\hbar}\frac{\sigma_{\mathrm{SH}}}{\sigma_{xx}} = \frac{2e}{\hbar}\frac{j_{\mathrm{s}}}{j_{\mathrm{c}}}, \tag{1.6}$$

where E is the applied electric fields. In experiments, θ_{SH} and σ_{xx} are measurable quantities. Thus, σ_{SH} is typically obtained by the following relation

$$\sigma_{\mathrm{SH}} = \frac{\hbar}{2e}\theta_{\mathrm{SH}} \cdot \sigma_{xx}. \tag{1.7}$$

Because spin current represents a flow of angular momentum, $\hbar/2e$ is commonly multiplied to $\theta_{\mathrm{SH}} \cdot \sigma_{xx}$.

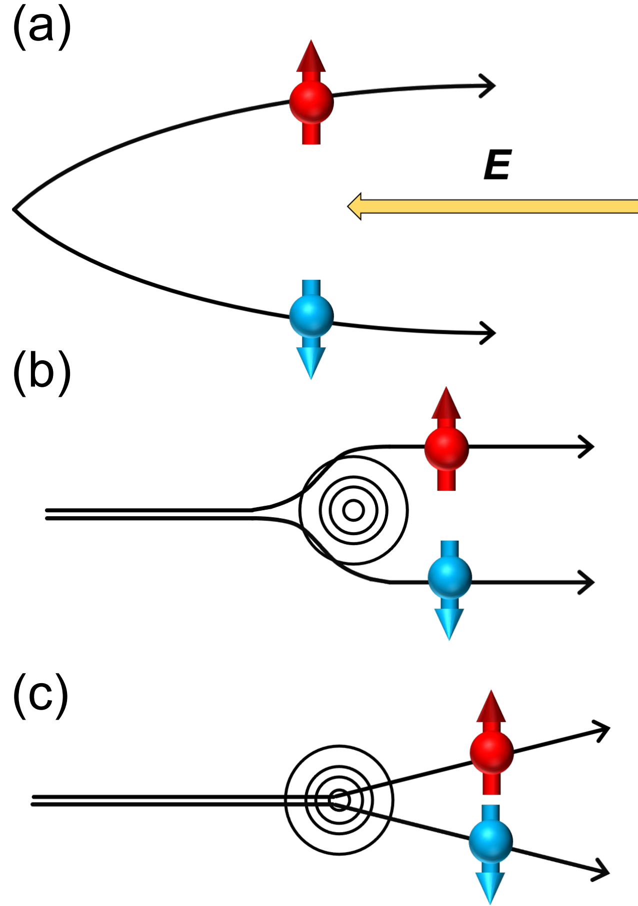

Figure 1.4: Schematic of the origins of the spin (anomalous) Hall effect as: (a) intrinsic mechanism due to Berry curvature; (b) side-jump extrinsic mechanism where the electron has a transverse displacement due to impurity; (c) skew scattering extrinsic mechanism due to the transverse scattering by impurity.

The physics and mechanisms of the SHE are directly borrowed from that of the well-established AHE [20]. Generally, the microscopic mechanisms of SHE (or AHE) are classified into three components: the intrinsic, side-jump, and skew scattering mechanisms, where the latter two are collectively called the extrinsic mechanisms. Thus, σ_{SH} can be written as a combination of these three contributions: $\sigma_{\mathrm{SH}} = \sigma_{\mathrm{SH}}^{\mathrm{int}} + \sigma_{\mathrm{SH}}^{\mathrm{s\text{-}j}} + \sigma_{\mathrm{SH}}^{\mathrm{sk}}$. These three mechanisms are schematically presented in Fig. 1.4.

For the intrinsic mechanism, the deflection of electrons with opposite spins can be described by the curvature of geometrical phase, namely the Berry

curvature [21], in the band structure of materials based on the semiclassical theory [22,23]. Electrons driven by an external electric field in materials with spin-orbit coupling can acquire a transverse anomalous velocity by a non-zero Berry curvature. The Berry curvature is originated from the band structure and does not depend on the scattering of the electron. Therefore, $\sigma_{\mathrm{SH}}^{\mathrm{int}}$ should be independent on the scattering relaxation time τ, i.e., $\sigma_{\mathrm{SH}}^{\mathrm{int}} \propto \tau^0$.

For extrinsic mechanisms, spin current results from the spin-orbit coupling-induced interaction between the conduction electron and impurities of materials. The side-jump can be understood as a transverse displacement of the conduction electron by impurities. The skew scattering is attributed to the asymmetric anomalous velocity of the electron with opposite spin polarization when the electron is scattered by impurities. The difference between these two mechanisms is their relationship with τ. For the side-jump mechanism, it is independent of τ, giving $\sigma_{\mathrm{SH}}^{\mathrm{s\text{-}j}} \propto \tau^0$. For skew scattering, it is proportional to τ, i.e., $\sigma_{\mathrm{SH}}^{\mathrm{sk}} \propto \tau^1$. Because τ is proportional to the conductivity σ_{xx}, contributions of SHE from different mechanisms can be distinguished by scaling the relationship between σ_{SH} and σ_{xx} in materials with different conductivity regimes [24,25].

A critical obstacle to the experimental detection of the SHE is that there is no spin voltage in analogy with the charge voltage, indicating that it cannot be detected by direct electrical measurement. Kato *et al.* observed the SHE for the first time using magneto-optical Kerr effect microscopy [26]. As shown in Fig. 1.5(a), non-zero spin density with different polarization is observed at the edges when an electric current is applied to a GaAs/InGaAs thin film stripe at 30 K. This result is attributed to the spin accumulation induced by the SHE. ISHE provides a means to detect spin current indirectly using electrical methods. A transverse charge current or charge accumulation in materials can be detected after injecting a spin current from an adjacent ferromagnetic material in ISHE experiment. For example, ISHE has been confirmed in Permalloy ($Ni_{89}Fe_{19}$, Py)/Pt bilayers by pumping spin current from the Py layer to the Pt layer via ferromagnetic resonance [27] and Al/CoFe nanowire devices by non-local spin current transport measurement [28].

θ_{SH} is related to the strength of spin-orbit coupling ζ. It is considered that the SHE is stronger in elements with heavier atomic mass Z because of $\zeta \propto Z^4$. Thus, a considerable θ_{SH} is expected in 5*d* HM [31]. The SHE-induced SOT in HM/FM bilayers is first observed in Pt/HM thin film heterostructures at room temperature [29,32,33]. As shown in Fig. 1.6, it has been found that the magnetization of the Co layer in Pt/Co/AlO_x exhibits PMA and can be switched by the SOT under a small in-plane magnetic field [29]. The switching was confirmed by another work showing that the magnetization of Pt/Co/AlO_x

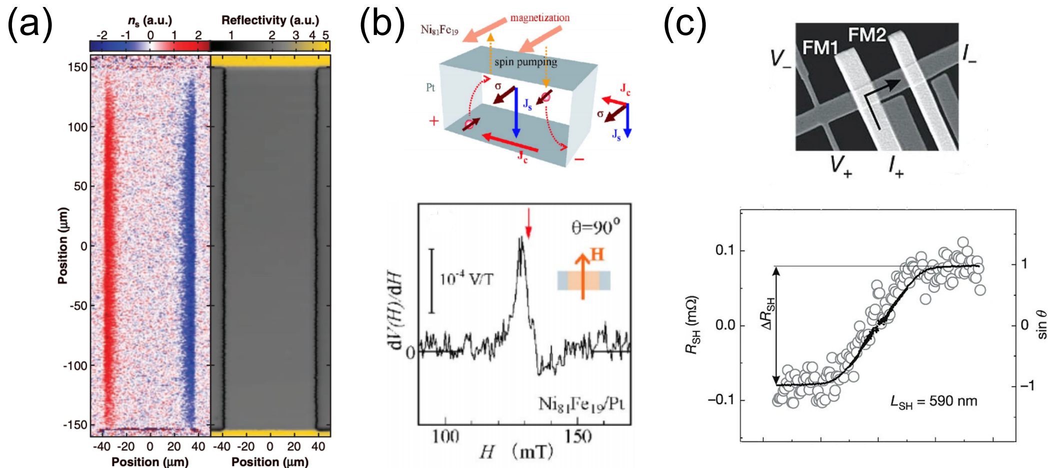

Figure 1.5: (a) Spin density mapping on GaAs/InAs thin film stripe under an electric field at 30 K using magneto-optical Kerr effect microscopy. (b) Ferromagnetic resonance spectra induced by ISHE in Py/Pt bilayers. (c) Scanning electron micrograph of Al/CoFe nanowires and the spin Hall resistance results. Figure (a), (b) and (c) are extracted from Ref. [26], Ref. [28] and Ref. [27], respectively.

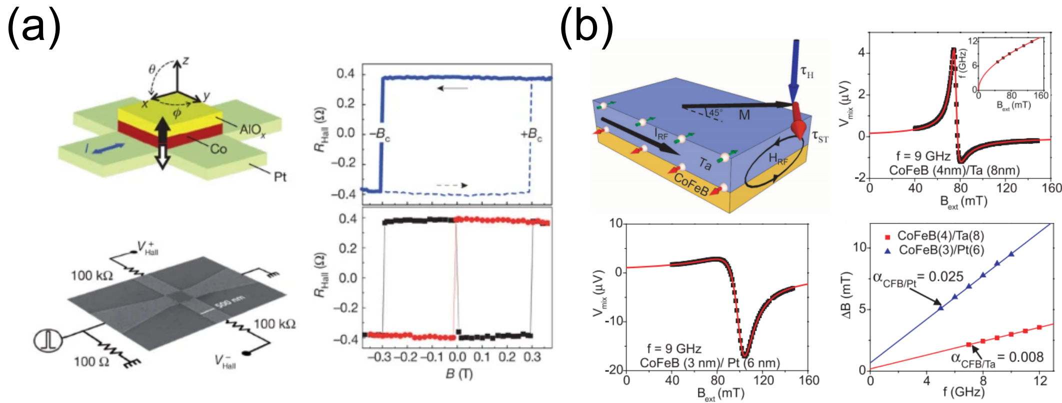

Figure 1.6: (a) Current-induced reversal of the magnetization of Pt/Co/AlOx trilayer. (b) Spin-transfer ferromagnetic resonance spectra for CoFeB/Ta and CoFeB/Pt bilayers. The symmetry part of the spectra related to DL-SOT is found opposite for these two bilayers. Reproduced from Ref. [29] and Ref. [30], respectively.

trilayer has a hysteresis loop as a function of injection current under a small in-plane magnetic field [33]. In a later work, Liu *et al*. observed a strong SOT in

CoFeB/Ta bilayers using the spin-torque ferromagnetic resonance method and a current can switch the magnetization of CoFeB at room temperature [30]. They characterize the efficiency of such torque using θ_{SH} and find the signal of θ_{SH} in Ta is opposite to that of Pt (see Fig. 1.6(b)). The sign and value of the spin Hall angle in Pt and Ta are consistent with the calculation of the intrinsic SHE [31]. After these discoveries, study on current-induced SOT in HM/FM heterostructures has become a focus point in the spintronics field [34–37].

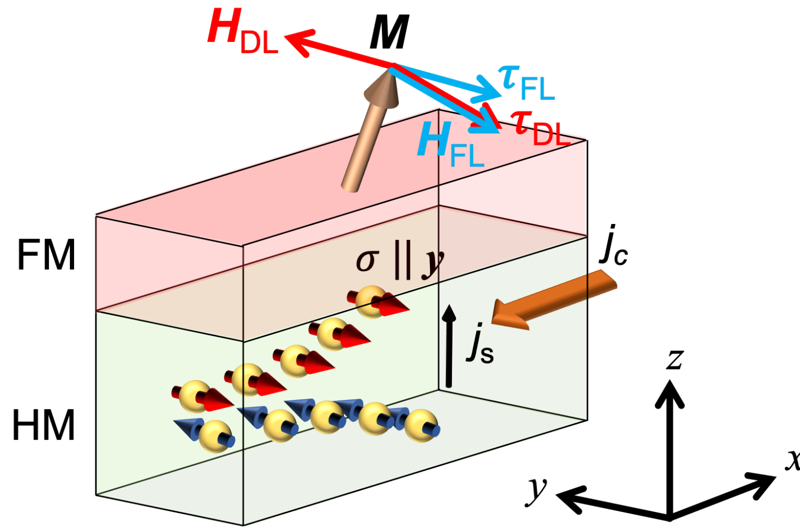

Figure 1.7: Schematic illustration of the geometry of current-induced SOT in the HM/FM bilayer.

The magnetization dynamics with current-induced SOT in HM/FM bilayers can be treated similarly as that with STT. Thus, SOT can be divided into two components: a damping-like SOT (DL-SOT) and a field-like SOT (FL-SOT) in analogy with STT. Schematic illustration of the geometry of the SOT and the corresponding effective fields H_{DL} and H_{FL} (see Eq. 1.3 for the definition), in the HM/FM bilayer are illustrated in Fig. 1.7. According to the definition of the SHE, $\boldsymbol{\sigma}$ of pure spin current flown from the HM layer to the FM layer is parallel to $\boldsymbol{y}$ if we consider a current is applied along the $\boldsymbol{x}$-axis. The corresponding effective fields of these two SOTs have been confirmed in many experiments using the harmonic Hall resistance technique and direct current magneto-transport method [38–41].

When SHE-induced spin current that flows from HM is absorbed by the FM layer and exerts SOT on the magnetization. The efficiency of DL-SOT and FL-SOT per unit current density are defined as ξ_{DL} and ξ_{FL}, respectively.

Specially, ξ_{DL} and ξ_{FL} read as [36]:

$$\xi_{\mathrm{DL(FL)}} = \frac{2e}{\hbar}\frac{\mu_0 H_{\mathrm{DL(FL)}} M_{\mathrm{s}} t_{\mathrm{eff}}}{j_{\mathrm{HM}}}, \tag{1.8}$$

where j_{HM} is the current density that flows in the HM layer and t_{eff} is the effective thickness of the FM layer. In previous studies, it has been found that FL-SOT originates not only from SHE but also from other phenomena, e.g., Rashba-Edelstein induced spin accumulation [42–46]. Thus, the discussion on SHE-induced current-spin conversion detected by SOT is focused on DL-SOT and ξ_{DL} can be used to refer to as current-spin conversion efficiency. In general, a fraction of SHE-induced spin current is absorbed by the FM layer due to spin backflow [47, 48] and/or enhanced spin scattering [46, 49] at the HM/FM interface. The transmittance of spin current at the interface, defined as T, depends on the choice of material. ξ_{DL} is thus related to the intrinsic spin Hall angle θ_{SH} via the following relation

$$\xi_{\mathrm{DL}} = T\theta_{\mathrm{SH}}. \tag{1.9}$$

Note that $T \leq 1$. Therefore, ξ_{DL} will not exceed θ_{SH} and ξ_{DL} provides a lower limit of θ_{SH}.

The strength of ξ_{DL} also depends on the spin diffusion length λ and the HM thickness d. The spin current induced by SHE diffuses within the HM layer. ξ_{DL} therefore increases with increasing d before it saturates [50]. This characteristic feature can be described using the spin diffusion model:

$$\xi_{\mathrm{DL}} = \bar{\xi}_{\mathrm{DL}}[1 - \mathrm{sech}(\frac{d}{\lambda})], \tag{1.10}$$

where $\bar{\xi}_{\mathrm{DL}}$ is the saturation efficiency of DL-SOT. For HMs, the value of λ is around several nanometer [51] and $\bar{\xi}_{\mathrm{DL}}$ can be obtained for thin films with d larger than $\sim 2\lambda$ according to the feature of Eq. 1.10.

1.2.2 Topological insulator/ferromagnetic metal heterostructures

The current-induced SOT in HM/FM thin film heterostructures owing to SHE is an efficient way to manipulate the magnetization of FM layers, putting forward the application of SOT-MRAM. Topological insulator (TI) [54,55] has also been suggested with great potential to generate SOT in TI/FM thin film heterostructures due to the spin-momentum locking property of the topological surface state (TSS) [56–59]. A brief introduction of this mechanism is described here.

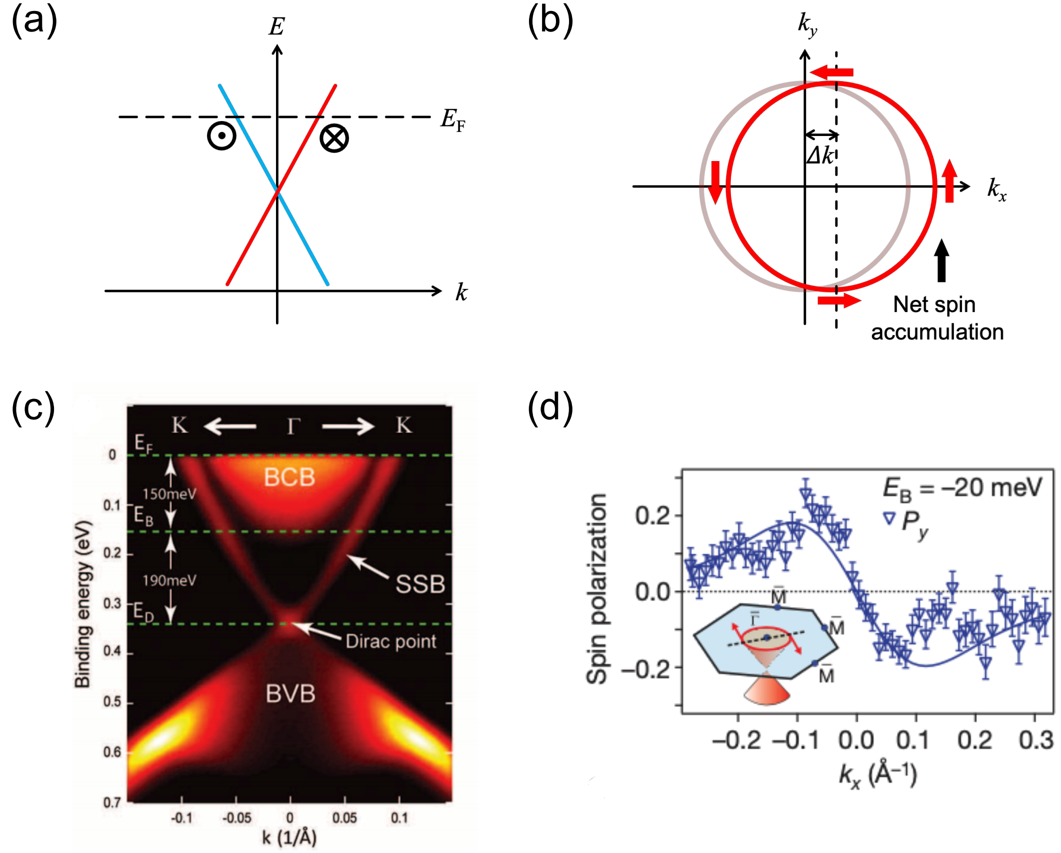

Figure 1.8: (a,b) Schematic illustration of the energy dispersion relationship for TSS (a) and the Fermi contour with a shift due to Rashba-Edelstein effect (b) in TI. (c,d) Band dispersion mapping of Bi_2Se_3 using ARPES (c) and wave vector dependent spin polarization on TSS of Bi_2Te_3 characterized by spin resolved-ARPES. (c) and (d) are respectively from Ref. [52] and Ref. [53].

TI is a type of material with an insulating bulk state but conducting surface state called TSS. The band dispersion of TSS forms a Dirac cone with quasi-massless Dirac electrons in momentum space because of the time-reversal symmetry and nontrivial band topology. The nontrivial band topology is attributed to the inversion of bulk bands due to strong spin-orbit coupling. The behavior of the Dirac electrons can be described using a Hamiltonian, which reads as [54, 55, 60–62]

$$\mathcal{H} = \hbar v_{\mathrm{s}} \left(\boldsymbol{\sigma} \times \boldsymbol{k}\right)_z = \hbar v_{\mathrm{s}} \begin{pmatrix} 0 & k_y + ik_x \\ k_y - ik_x & 0 \end{pmatrix}, \tag{1.11}$$

where v_{s} is the surface electron velocity, $\boldsymbol{k} = (k_x, k_y)$ is the two-dimensional Bloch wave vector and z is the direction normal to TSS. $\boldsymbol{\sigma}$ is the Pauli matrices.

The eigenvalues E and eigenstates $|\psi\rangle$ of the Hamiltonian can be solved as

$$E_{\pm} = \pm\hbar v_{\mathrm{s}}|\boldsymbol{k}|;\ |\psi_{\pm}\rangle = \frac{1}{\sqrt{2}}\begin{pmatrix} 1 \\ \mp i\left(k_x + ik_y\right)/|\boldsymbol{k}| \end{pmatrix} e^{i\boldsymbol{k}\cdot\boldsymbol{r}}, \tag{1.12}$$

where $\boldsymbol{r}$ is the position. One can obtain the spin polarization vector of the Dirac electrons $\boldsymbol{\sigma}_{\mathrm{TSS}}$ at $E_{\pm}$ using $\boldsymbol{\sigma}$ as an operator, which reads as

$$\boldsymbol{\sigma}_{\mathrm{TSS}} = \langle\psi_{\pm}|\boldsymbol{\sigma}|\psi_{\pm}\rangle = \left(\pm\frac{k_y}{|\boldsymbol{k}|}, \mp\frac{k_x}{|\boldsymbol{k}|}, 0\right). \tag{1.13}$$

This result indicates that the spin polarization of Dirac electrons is always orthogonal to $\boldsymbol{k}$ on TSS. This phenomenon is called spin-momentum locking. The energy dispersion relationship and the Fermi contour are schematically illustrated in Figs. 1.8 (a) and (b), respectively. Angle-resolved photoemission spectroscopy (ARPES) and spin-resolved ARPES, powerful photon-in electron-out techniques to characterize the band structure and its spin polarization, have been used to detect the TSS and its spin-momentum locking property experimentally [52, 53, 63–69]. Typical energy dispersion of a three-dimensional TI Bi_2Se_3 mapped by APRES [52] and the spin polarization of TSS observed in Bi_2Te_3 [53] are illustrated in Figs. 1.8 (c) and (d), respectively. These experiments are in good agreement with theoretical prediction [61].

Rashba-Edelstein effect (REE) [70, 71], which is originally proposed in the system with broken inversion symmetry, is a phenomenon that originates from spin-momentum locking. Using TSS as an example, it is schematically illustrated in Fig. 1.8(b). When an in-plane charge current $\boldsymbol{j}_{\mathrm{c}}$, defined along x or say k_x, is applied to TI, it will only flow in the conducting TSS. The Fermi contour of TSS will experience a shift Δk by $\boldsymbol{j}_{\mathrm{c}}$, resulting in more forward-moving electron states occupied than backward-moving states. The non-equilibrium TSS will generate a net spin accumulation, polarized along y-axis, due to spin-momentum locking. In TI/FM thin film heterostructures, the net spin accumulation in TSS can flow into adjacent FM layers, resulting in a torque exerted on the local moment of the FM layer. Spin-momentum locking in TSS is attributed to the spin-orbit coupling eventually. Hence, the torque in TI/FM heterostructures is also referred to as SOT.

Mellnik *et al*. first demonstrated the current-induced SOT due to REE in pristine Bi_2Se_3/Py thin film heterostructures in 2014 [74]. It was found that the torque has a dominant component with the same symmetry of damping-like STT. They estimated ξ_{DL} with a value of $\sim$ 2.0-3.5. This value is over ten times larger than the largest one observed in HM tungsten, which is $\sim$ 0.3 [34]. From then, large ξ_{DL} has been confirmed in different TIs in addition to Bi_2Se_3 [75–78]. Notably, Mahendra *et al*. have reported a giant $\xi_{\mathrm{DL}}\sim$18.6,

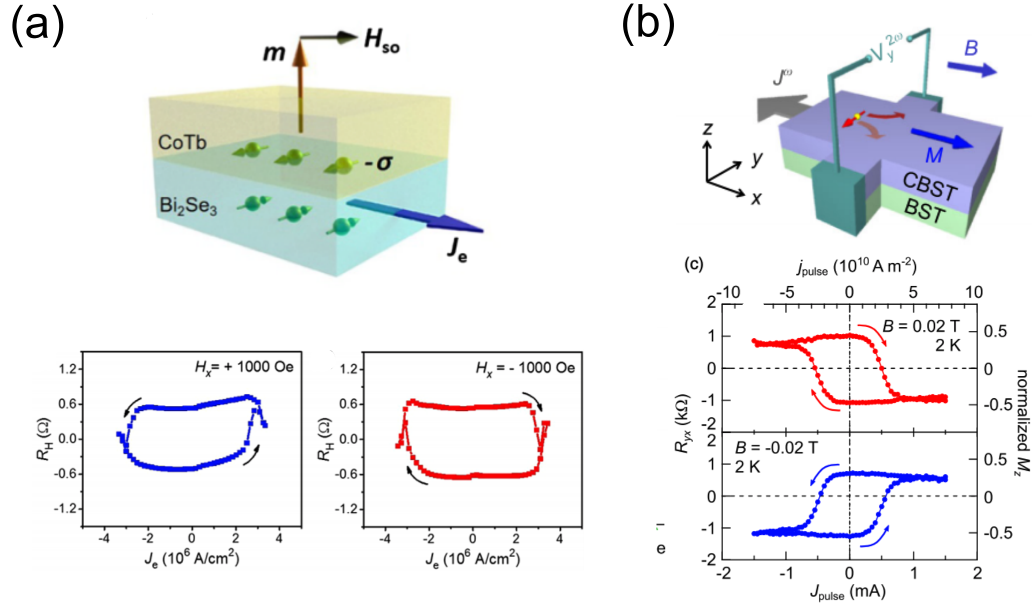

Figure 1.9: (a) Anomalous Hall resistance plotted as a function of injection current density in Bi_2Se_3/CoSb bilayers at room temperature. (b) Anomalous Hall resistance hysteresis loops as a function of the intensity or density of injection current in $Cr_x(Bi_{1-y}Sb_y)_{2-x}Te_3/(Bi_{1-y}Sb_y)_2Te_3$ at 2 K. (a) and (b) are originally from Ref. [72] and Ref. [73], respectively.

in polycrystalline Bi_2Se_3/CoFeB thin film heterostructures and suggested it is due to the quantum confinement [79]. The thin films were deposited using magnetron sputtering, which is a conventional technique for mass production. This discovery overcomes the obstacle for practical application of SOT in TI/FM heterostructures since TI thin films have been only grown by laboratory-based molecular beam epitaxy (MBE) method. However, the mechanism of this result is still under debate. The magnetization switching has also been realized in different TI/FM bilayers exhibiting PMA [72, 73, 75]. Some results are presented in Fig. 1.9.

1.3 Bismuth and the alloy

The generation of SOT in HM/FM and TI/FM thin film heterostructures is attributed to spin accumulation at the interface induced by the current through different mechanisms, i.e., the SHE and/or REE. Therefore, identifying materials with large current-spin conversion efficiency and understanding

its mechanism is crucial to obtain strong SOT and its application. Bismuth, a semimetal with strong spin-orbit coupling, and bismuth-antimony alloy, a TI for antimony concentration between 0.07 and 0.22, are such candidate materials. Some basic properties and former studies on these materials are described here.

1.3.1 Bismuth

Bismuth is a Group-V element with an atomic number 83. The only primordial isotope of bismuth ^{209}Bi is the heaviest naturally occurring atom with approximately infinite radiative lifetime [80]. Crystal Bi exhibits a rhombohedral structure with a space group of $R\bar{3}m$. Its band structure is shown in Fig. 1.10 (a) [81]. Bi is a semimetal hosting an electron valley at the L point and a hole valley at the T point with small carrier concentration but large mobility [82]. The narrow band gap at the L point is $\sim 15\,\text{meV}$. The conduction electrons in Bi at the L point can be described by the Dirac Hamiltonian with an extremely small effective mass [83–85]. Hence, these electrons are called massive Dirac electrons.

Strong SHE is expected in Bi because of its large spin-orbit coupling due to the heavy atomic mass. In theory, Fuseya *et al*. used the Kubo formula to calculate the intrinsic SHC of Bi based on the Dirac-like character of electrons in the L valley [86]. They find intrinsic SHC takes a maximum when the Fermi level is located in the narrow gap at the L point. Fukuzawa *et al*. calculated both the intrinsic and extrinsic SHC of Bi [87]. Their result shows that the intrinsic part of SHC is consistent with the previous work and point out that the extrinsic SHE can be dominant over the intrinsic one when the Fermi level cut the band. A calculation based on the tight-binding model has predicted an appreciable value of the intrinsic SHC in Bi at room temperature as 474 $(\hbar/e)$ $\Omega^{-1}\cdot\text{cm}^{-1}$ [88]. This value is comparable to that of 5d HM [88]. Representative results of these works are summarized in Fig. 1.10.

So far, a number of works have been reported on detecting spin-current conversion in Bi experimentally. However, the results are conflicting. For example, Hou *et al*. measured the spin-current conversion efficiency in Bi/Py bilayers using ferromagnetic resonance-induced spin pumping [89]. They found that the efficiency decreases with increasing Bi thickness and attributed the trend to the ISHE tunable by the Bi/Py interface (Fig. 1.11(a)). Another spin pumping measurement using Bi thin films grown on yttrium-iron-garnet (YIG) substrate by Emoto *et al*. shows that the spin-current conversion efficiency is quite small, with a value of ~ 0.00012 [90]. However, they find the Bi thickness dependence of the spin-current conversion efficiency follows the spin diffusion

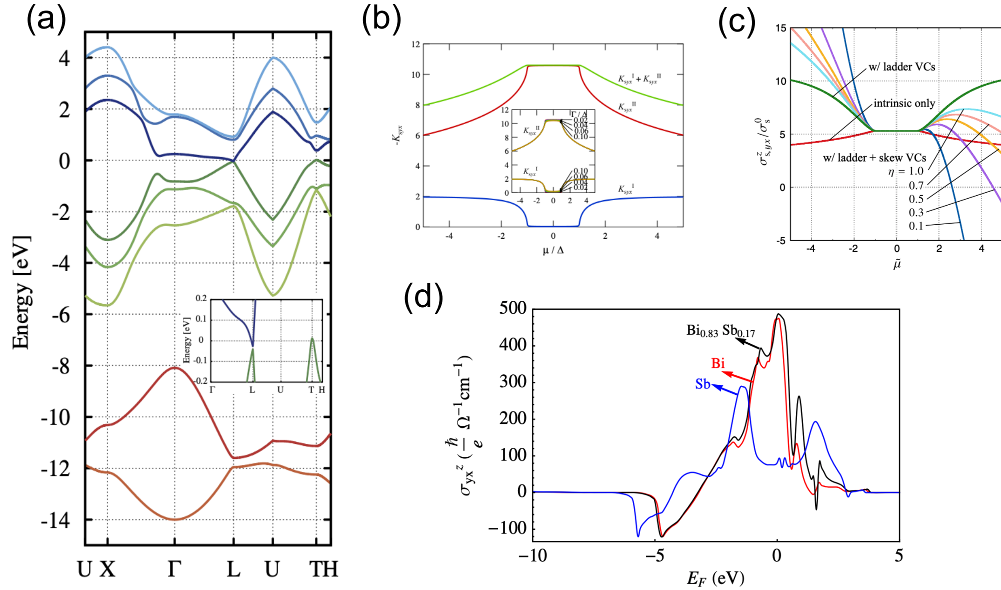

Figure 1.10: (a) Band structure of Bi. The zoomed-in area of Γ-H near Fermi level is shown in the inset. (b) Calculation results of the intrinsic SHC in Bi near the gapped Dirac point. The electrons at the L valley is assumed as massive Dirac electrons. (c) Intrinsic and extrinsic SHC of Bi calculated by using Dirac Hamiltonian to describe electrons at the L point. (d) Fermi level dependence of the intrinsic SHC for Bi, Sb and $Bi_{0.83}Sb_{0.17}$ calculated based on tight-binding model. (a), (b), (c), and (d) are reprinted from Refs. [81], [86], [87], and [88], respectively.

model (Fig. 1.11(b)). Thus, they suggest the spin-current conversion is governed by the bulk ISHE in Bi. A very recent work by the same group observed the current-induced SOT in Py/Bi bilayers using spin torque-ferromagnetic resonance technique [91]. Unlike the previous result, they find the current-spin conversion efficiency is larger ($\sim$ 0.03-0.06) (Fig. 1.11(c)). They infer that the material choice of the ferromagnetic layer can be essential for the characterization of current-spin (spin-current) conversion. Yue *et al.* have used a thermally injected spin current transport technique to detect spin-current conversion in Bi thin films; while they found the efficiency is negligible [92]. Notably, they point out contributions induced by the magnetothermal effect, e.g., the ordinary Nernst effect (ONE), are likely to mix into the spin-current conversion signal (Fig. 1.11(d)). The divergence of the values of current-spin (spin-current) conversion efficiency in Bi urges further experimental studies to conclude it eventually.

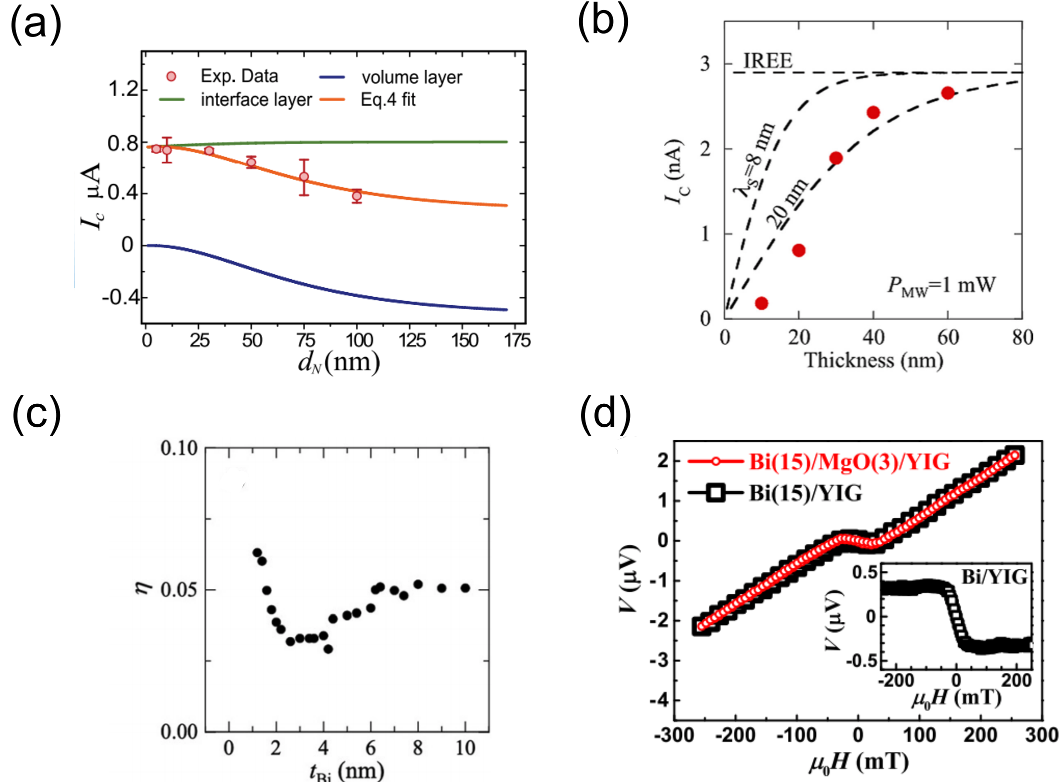

Figure 1.11: (a) Bi thickness dependence of the transverse charge current intensity resulted from spin current injection in Bi/Py bilayers. The signal is dominated by the contribution from surface effect. (b) Spin-injection induced charge current intensity as a function of Bi thickness in YIG/Bi heterostructures. The thickness dependence is in accordance with spin diffusion model. (c) Bi thickness dependence of the current-spin conversion efficiency (Note that η is equivalent to ξ_{DL} defined in Eq. 1.5.) in Py/Bi heterostructures. Sizable efficiency is observed. (d) External magnetic field dependence of the transverse voltage signal induced by a spin current injected and thermal gradient in YIG/Bi heterostructures. The contribution in the signal which is linear to field is attributed ONE. (a) to (d) are originally from Refs. [89], [90], [91], and [92], respectively.

1.3.2 Bismuth-antimony alloy

Antimony is a Group-V element with an atomic number 51. Crystal Sb has a rhombohedral structure, the same as Bi. Bi and Sb form a solid solution throughout the composition according to the phase diagram [93]. For $0.07 < x < 0.22$, $\mathrm{Bi}_{1-x}\mathrm{Sb}_x$ has been predicted as a three-dimensional TI due to band inversion in this regime [94]. The evolution of the band inversion in $\mathrm{Bi}_{1-x}\mathrm{Sb}_x$ with increasing x is schematically illustrated in Fig. 1.12(a). The TSS

of $Bi_{1-x}Sb_x$ has been observed using ARPES [63, 95], shown in Fig. 1.12(b). Besides TSS, energy dispersions of surface state induced by the Rashba effect have also been observed. The observed band structure is different from the results predicted by first-principle calculations [96,97]. Due to the complicated surface states of $Bi_{1-x}Sb_x$, the studies on TI using ARPES has shifted its focus on other materials with the simpler TSS.

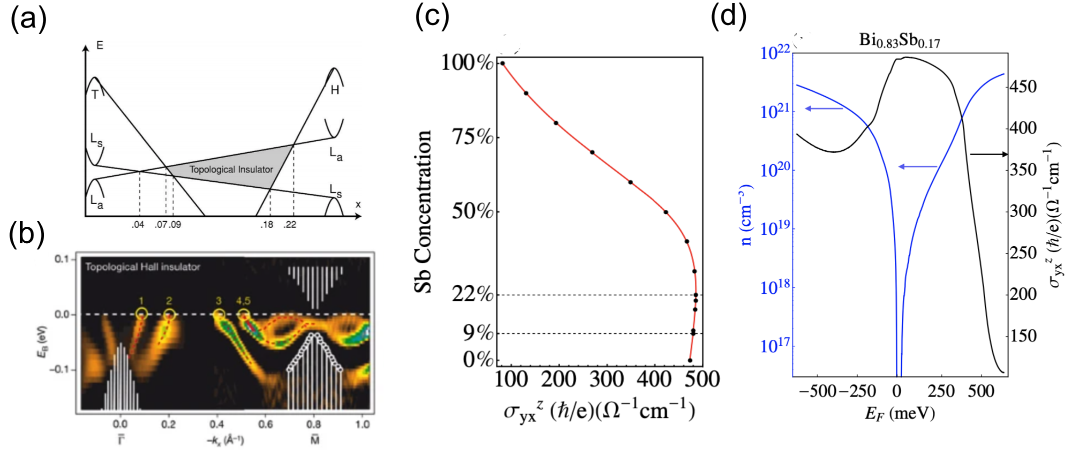

Figure 1.12: (a) Schematic of the evolution of band inversion for $0.07 < x < 0.22$ in $Bi_{1-x}Sb_x$. (b) Energy dispersion mapping along $\bar{\Gamma}$-$\bar{M}$ in k space gathered by ARPES. (c, d) The calculated Sb concentration dependence of the SHC for BiSb alloy (c) and Fermi level dependence of the carrier concentration and SHC in $Bi_{0.83}Sb_{0.17}$ (d) at room temperature. (a) and (b) are extracted from Refs. [94] and [63], respectively. (c) and (d) are reprinted from Ref. [88].

The SHE of $Bi_{1-x}Sb_x$ has been predicted as a function of x by Sahin *et al.* [88]. In their calculation (Fig. 1.12(c)), the SHC of $Bi_{1-x}Sb_x$ initially increases with increasing x. However, it begins to drop with further increasing x, which is attributed to the reduced spin-orbit coupling. Within the regime where band inversion occurs where $Bi_{1-x}Sb_x$ is a TI, the SHC is a little larger than that of Bi. Because of the bulk semiconductor property in this regime, the conductivity is smaller than that of Bi. Thus, they consider that the spin Hall angle of $Bi_{1-x}Sb_x$ in this regime could be larger than that of Bi. They also find the SHC changes as a function of Fermi level for $Bi_{0.83}Sb_{0.17}$, suggesting that voltage-control-of SHE is seemingly to be realized in $Bi_{0.83}Sb_{0.17}$.

Because of the TI character of $Bi_{1-x}Sb_x$ for $0.07 < x < 0.22$, large SOT originated from REE is believed in $Bi_{1-x}Sb_x$/FM thin film heterostructures. Recently, Khang *et al.* have characterized current-induced SOT in $Bi_{0.9}Sb_{0.1}$/MnGa heterostructures grown by MBE [98]. They find the current-spin conversion ef-

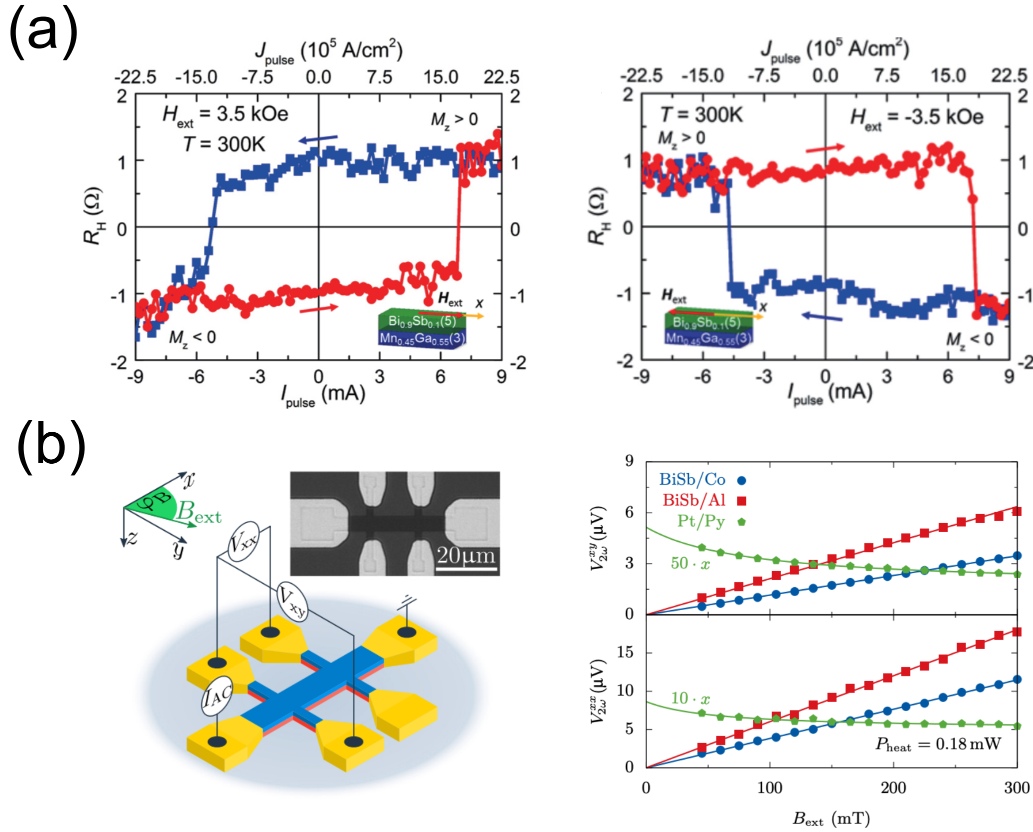

Figure 1.13: (a) Anomalous Hall resistance hysteresis loops as a function of the magnitude of injected current (or current density) under a in-plane magnetic field for the $Bi_{0.90}Sb)0.1$/MaGa heterostructure. The current-induced switching of magnetization is observed with a small current density in $Bi_{0.90}Sb)0.1$. (b) The device geometry for harmonic Hall voltage (V_{xx} and V_{xy}) measurement (left panel) and the field dependence of the second harmonic voltage ($V^{xx}_{2\omega}$ and $V^{xy}_{2\omega}$) (right panel) in BiSb/Co bilayers. The contribution from the ONE is found dominant in the second harmonic voltage. (a) and (b) are originally from Refs. [98] and [99], respectively.

ficiency in $Bi_{0.9}Sb_{0.1}$ has a huge value ~ 52, the largest among all the materials studied so far. They consider the current-induced SOT should be attributed to the TSS of $Bi_{0.9}Sb_{0.1}$. They also demonstrate that the magnetization of MnGa in $Bi_{0.9}Sb_{0.1}$/MnGa heterostructures can be switched by injecting a current with a very little density in $Bi_{0.9}Sb_{0.1}$ compared to HMs (see Fig. 1.13(a)). However, another characterization of SOT in BiSb/Co thin film heterostructures using harmonic Hall resistance technique by Roschewsky *et al*. has found that the contribution from the ordinary Nernst effect (ONE) plays an impor-

tant role in measurement signal [99]. They report negligible current-spin conversion efficiency in the alloy (see Fig. 1.13(b)). This disagreement between the two experiments impel additional studies to confirm current-spin conversion in BiSb. As mentioned above, the ONE contribution has also been reported in the spin-current conversion measurement of YIG/Bi bilayers by Yue *et al*. [92]. These results indicate that careful data analysis is necessary while studying materials containing Bi.

1.4 Objective and outlines of this thesis

The objective of this thesis is to identify current-spin conversion in materials based on Bi and understand its mechanism by charactering the SOT of Bi-based material/FM thin film heterostructures. As mentioned above, the TSS of BiSb alloy has been predicted [94] and confirmed [63]. However, its effect on current-spin conversion needs to be examined [98,99]. Both REE and SHE can result in the current-spin conversion. Considerable SHC has been predicted in BiSb alloy [88], whereas it has not been confirmed yet. Thus, if the SOT is generated in BiSb alloy/FM heterostructures, an important issue needs to be addressed is understanding its mechanism. The procedure of my work is divided into three steps. First, demonstrate the current-spin conversion in BiSb alloy and understand its mechanism. Polycrystalline BiSb alloy/CoFeB thin film heterostructures have been grown for the SOT characterization. I attempt to clarify its mechanism by studying the current-spin conversion of BiSb under different conditions. Second, investigate current-spin conversion in carrier-doped Bi thin films and identify its origin. During the study on BiSb/CoFeB heterostructures, massive Dirac electrons in the L valley of Bi [86, 87] are inferred to play an important role in its current-spin conversion. I characterize the SOT of carrier-doped Bi/CoFeB thin film heterostructures in detail for confirming the assumption. Third, explore the PMA and current-spin conversion in a $Pt_{1-x}Bi_x$/Co/MgO trilayer system. After the demonstration of appreciable current-spin conversion in Bi, looking for a Bi-based system exhibiting PMA will have a practical meaning that devices with PMA is suitable for high-density information storing. I attempt to introduce Bi into Pt/Co/MgO trilayers, a system exhibiting strong PMA [29, 100–102], and study how the PMA and current-spin conversion of the heterostructures vary via changing Bi doping level.

The following chapters provide detailed description of the methods we used in our experiments and the results of current-spin conversion in different Bi-based material thin films, as follows:

Chapter 2 introduces the methods employed in our experiments, includ-

ing sample growth, thin film structure characterization, magnetic property measurement, device fabrication, electrical transport measurement and SOT characterization. We use the harmonic Hall resistance technique to characterize the SOT in our samples. The principle of this technique is presented in detail.

Chapter 3 describes current-spin conversion in BiSb alloy thin films. A current-spin conversion with an efficiency exceeding an unity is observed in BiSb alloy thin films at room temperature. Its mechanism is studied by investigating the efficiency as a function of BiSb alloy thin film thickness, composition, facet, and measurement temperature.

Chapter 4 presents current-spin conversion in pristine and carrier-doped Bi thin films. The carrier doping in Bi is performed by substituting Bi with Te and Sn. The doping results in effective control of the Fermi level and the concentration of massive Dirac electrons in Bi. We demonstrate the relationship between the current-spin conversion of Bi and the Fermi level position in its band structure. The robustness of current-spin conversion in Bi has also been investigated by characterizing the SOT in Bi/FM heterostructures grown under different conditions.

Chapter 5 describes the research on PMA and current-spin conversion in $Pt_{1-x}Bi_x$/Co/MgO trilayers. The structure, magnetic anisotropy and current-spin conversion are studied systematically in the trilayers as a function of the Bi doping level.

Finally, a brief summary of the experimental results concludes this thesis, and some outlooks for further studies are proposed in Chapter 6.

Chapter 2

Experimental methods

2.1 Radio frequency mangetron sputtering thin film deposition

The thin film heterostructures studied in this thesis are grown using radio frequency (RF) magnetron sputtering method at ambient temperature. Magnetron sputtering is a process where atoms or molecules of material are emitted from a target by the collision of high-speed particles. The ejected atoms or molecules are deposited onto a substrate and form thin films.

Schematic of the magnetron sputtering technique is illustrated in Fig. 2.1. After transferring the substrates mounted on a holder into the sputtering chamber with a high base vacuum ($\leq 1 \times 10^{-6}$ Pa), argon (Ar) gas fills the chamber with controlled gas pressure. An RF sputtering power is then applied between the substrates and target. In this case, the substrates and traget can be seen as the anode and cathode in a capacitance. During the first-half positive AC current oscillation cycle in RF, the target works as the cathode. Ar gas is ionized by the high bias voltage and a stable plasma is formed in the chamber. The target is bombarded by the attracted Ar ion and atoms or molecules are ejected, constituting the thin films on the substrates. On the following negative AC current oscillation cycle, the target becomes the anode and attracts more electrons than Ar ions due to their higher mobility. The permanent magnets behind the target are used to trap the electrons on the target and prevent it from hitting the substrate. This process improves the efficiency of Ar gas ion formation in AC current modulation, suppresses the discharge of the plasma and avoids the substrates from overheating. The advantage of an RF sputtering power is that it avoids charge building-up on the targets and insulating materials can be thus deposited. The sputtering rate of materials is tunable by changing the Ar gas pressure and RF sputtering power.

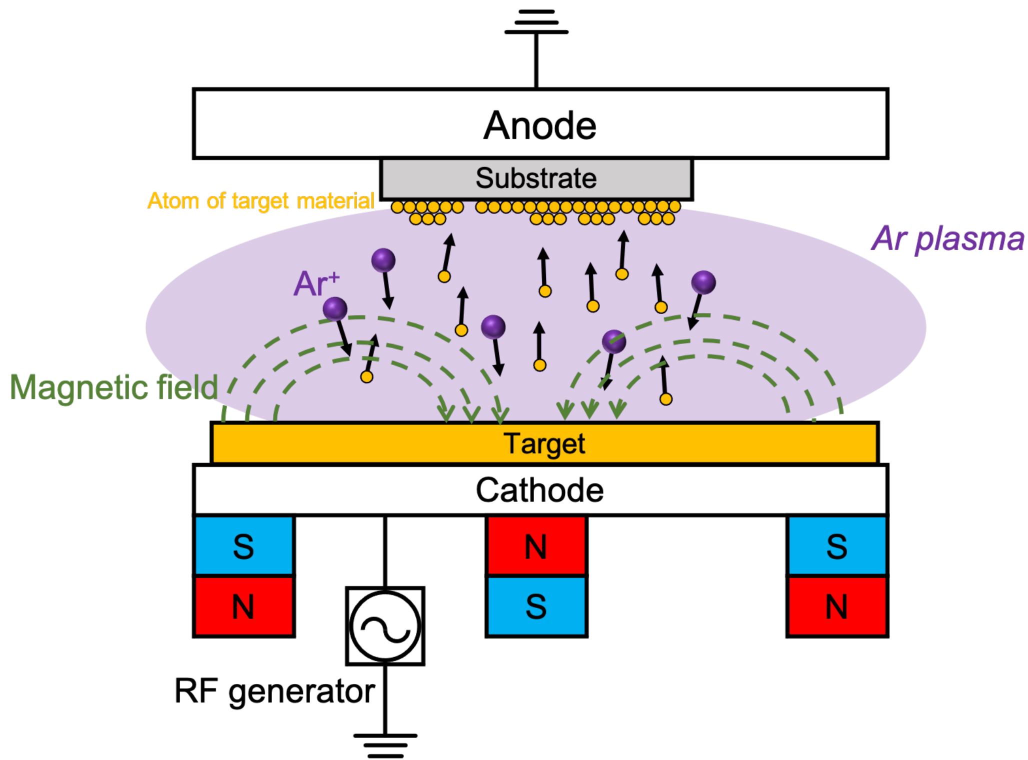

Figure 2.1: Schematic illustration of the RF magnetron sputtering technique.

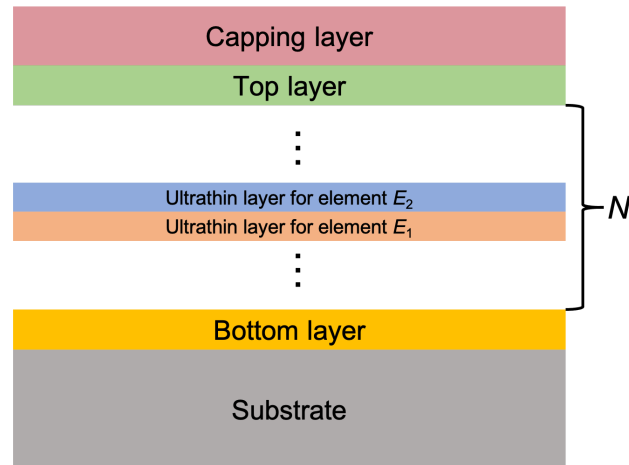

Figure 2.2: Schematic of a heterostructure with layers grown by alternating ultrathin layer deposition (AULD) method.

We establish a method to grow binary compound thin films, which is different from using stoichiometric alloy targets or co-sputtering technique. A heterostructure with the binary compound thin film formed by this method is schematically illustrated in Fig. 2.2. Ultrathin films of the two elements, E_1

and E_2, in the binary compound are deposited alternatively and constitute a bilayer with a repeat number of N. The thickness of each bilayer is set below 1 nm. The mixing of the two elements in the multilayer which leads to formation of an alloy thin film is confirmed using scanning transmission electron microscopy. We refer to this method as alternating ultrathin layer deposition (AULD). AULD allows simple means to control the composition of the alloy.

2.2 X-ray diffraction

The crystalline texture of the thin films grown by RF magnetron sputtering is analyzed using x-ray diffraction (XRD). XRD analysis is based on Bragg's law. The Bragg condition is schematically shown in Fig. 2.3. When two beams of x-ray (regarded as waves) with the same phase and wavelength approach a crystalline thin film with a glancing angle θ, they will be scattered from the lattice planes separated by an interplanar distance d. The two scattered waves remain in phase when the difference between their path lengths is an integer multiple of the wavelength λ. The difference between the path lengths is $2d\sin\theta$. Thus, the constructive interference with strongest intensity, i.e., Bragg peaks, can be observed when θ meets the condition

$$2d\sin\theta = n\lambda, \tag{2.1}$$

where n is a positive integer. d is determined by the lattice constant and crystalline orientation. Thus, the texture information of the thin film can be obtained from the spectral intensity as a function θ. 2θ is typically plotted in the horizontal axis in the spectra. We use Riguku® Smartlab to acquire the XRD spectra of our thin film samples. Cu K_α characteristic x-ray, with a wavelength of 1.54 Å, is used in all measurements.

2.3 Vibrating sample magnetometer measurement

The magnetic properties of samples with ferromagnetic metal (FM) layers are measured using a vibrating sample magnetometer (VSM) at room temperature. Schematic of a VSM instrument is presented in Fig. 2.4. The sample is mounted on a quartz rod, which is placed between two electromagnets. The quartz rod can be rotated, allowing the magnetic field to point along or normal to the film plane. The sample is magnetized after applying a uniform magnetic field and vibrated sinusoidally using the quartz rod. According to Faraday's law of induction, an electromotive force is generated in the pick-up coils by

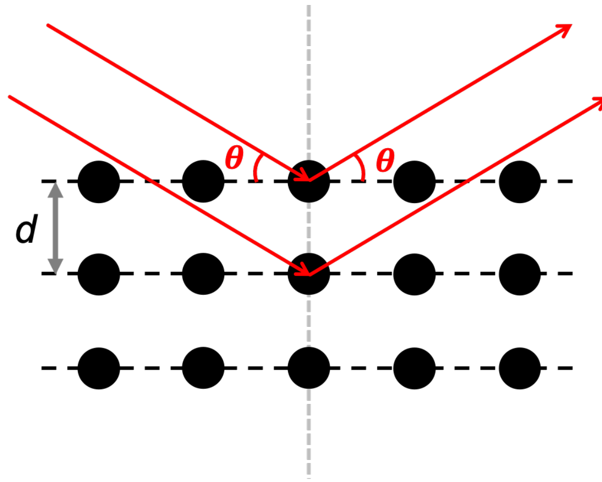

Figure 2.3: Schematic of the Bragg conditions for obtaining constructive interference of x rays scattered from lattice planes separated by an interplanar distance d at the injection angle θ.

moving the magnetized sample. The electromotive force in the pick-up coils is proportional to the magnetic moment of the sample. The strength of the electromotive force is recorded using a lock-in amplifier. We use a VSM made from TAMAKAWA Co., LTD to carry out our measurement. The magnetic field can be applied up to 2 T in the measurement and the vibration frequency is set to 82.5 Hz. The magnetic field is strong enough to saturate the magnetization of the soft FM thin films used in our measurements along the easy- and hard-axis.

2.4 Device fabrication

Micron-scale devices for transport measurement is fabricated from the thin film samples using optical lithography and ion milling. The geometric pattern can be transferred from a photomask to the sample coated with a photoresist layer by optical lithography. We use MICROPOSIT™ S1813G photoresist in this process. It is a positive resist and the part exposed to ultraviolet light is dissolved in a developer. The typical thickness of the resist layer is $\sim 1.2\,\mu$m after spin-coating at 5000 rpm for 30 s. MF-319 is used as the developer in the developing process. We use Ar ion beam for ion milling, which is carried out in the loadlock chamber of the RF magnetron sputtering instrument with a base pressure below 5×10^{-4} Pa. The sample area without the resist coating can be removed via bombardment of the Ar ion beam. The duration of the ion

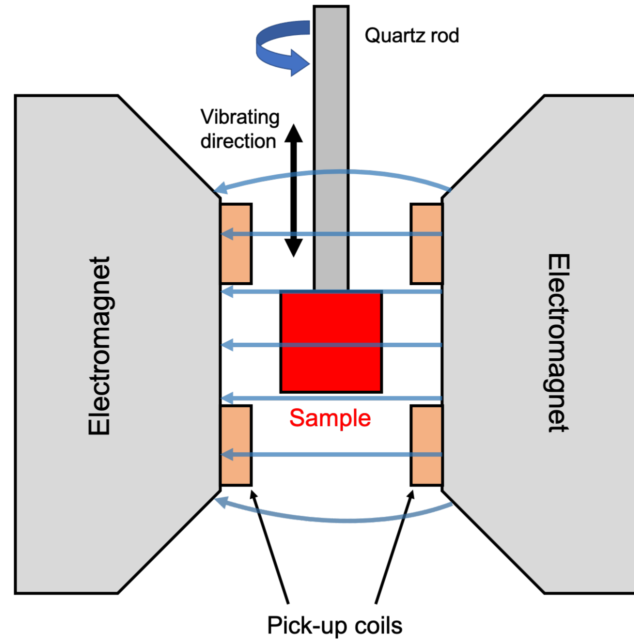

Figure 2.4: Schematic illustration of the part close to sample in a vibrating sample magnetometer (VSM).

milling depends on the property and thickness of the thin films. The contact pads, i.e., electrodes, are formed on the fabricated devices using a standard lift-off process. The electrodes are deposited by RF magnetron sputtering and the structure is the same for all the devices, which is 5 Ta/60 Cu/5 Pt (unit in nanometer).

The optical lithography and ion milling processes are illustrated in Fig. 2.5. The procedure is:

1. Coat S1813G resist at 5000 rpm for 30 s by a spin-coater.

2. Pre-bake at 115 °C for 60 s to dry the resist.

3. Mount the photomask. Illuminate using ultraviolet light generated by a mercury lamp for 30 s.

4. Develop in MF-319 developer for 150 s followed by water rinse for several seconds.

5. Etch the film by Ar ion beam with a gas pressure of 6×10^{-2} Pa. Wait 5 min after etching for cooling.

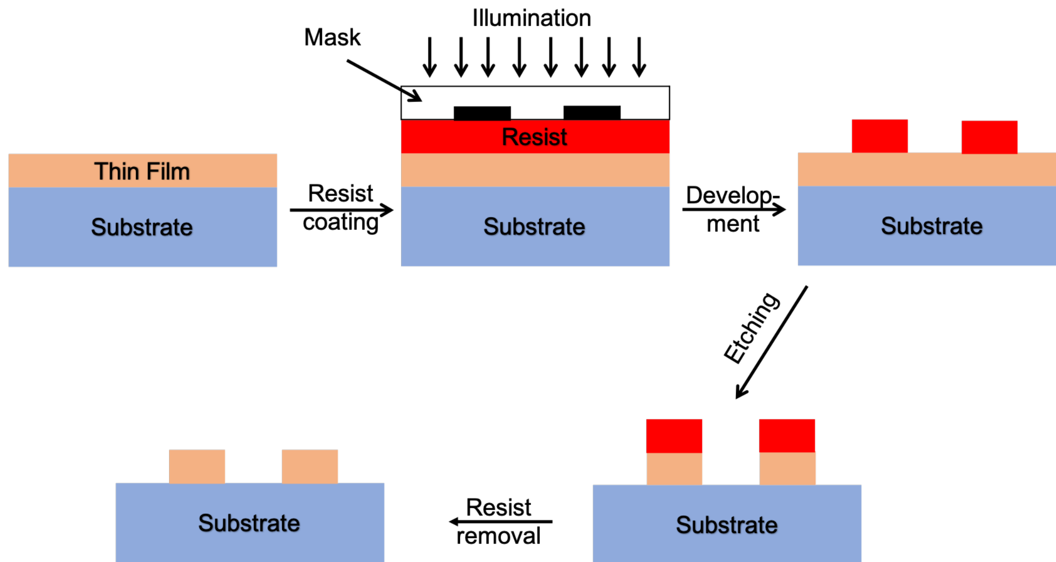

Figure 2.5: Schematic of optical lithography and ion milling process for device fabrication.

6. Remove the resist using ultrasonic cleaner by immersing in a solvent in the sequence of N-Methyl-2-pyrrolidone, acetone, and isopropyl alcohol.

The lift-off process for forming electrodes is schematically shown in Fig. 2.6. The procedure is listed as follows:

1. Coat S1813G resist at 5000 rpm for 30 s by a spin-coater.

2. Pre-bake at 115 °C for 60 s to dry the resist.

3. Mount the photomask. Illuminate using ultraviolet light generated by a mercury lamp for 30 s.

4. Develop in MF-319 developer for 150 s followed by water rinse for several seconds.

5. Etch the film by Ar ion beam with a gas pressure of 6×10^{-2} Pa for 20 s to remove the oxidation layer on the surface of samples. Wait 5 min after etching for cooling.

6. Deposit 5 Ta/60 Cu/5 Pt electrodes by RF magnetron sputtering.

7. Remove the resist using ultrasonic cleaner by immersing in a solvent in the sequence of N-Methyl-2-pyrrolidone, acetone, and isopropyl alcohol.

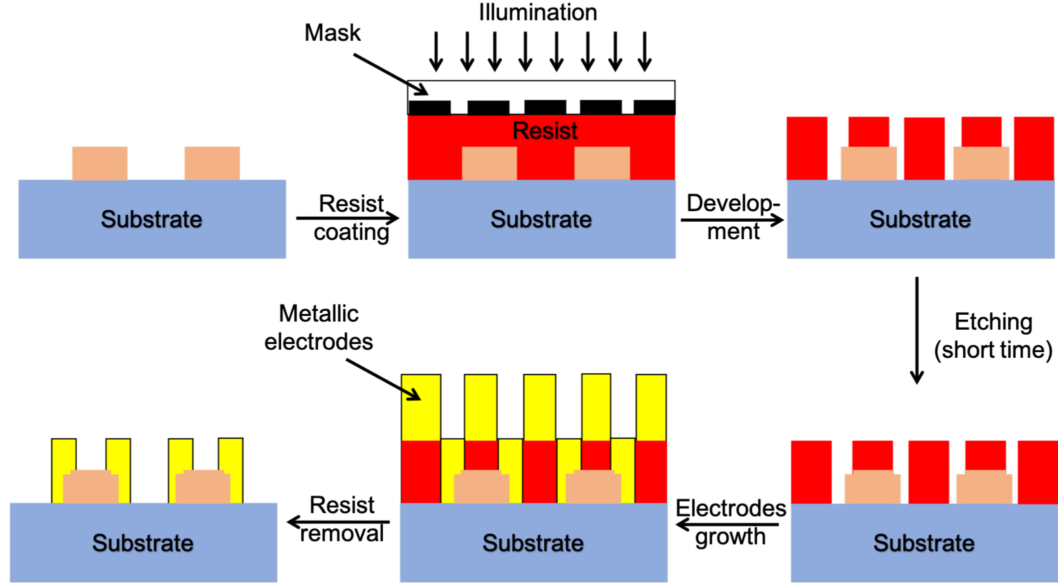

Figure 2.6: Schematic of lift-off process for adding electrode pads.

2.5 Direct current transport measurement

The direct current (DC) magneto-transport property of the thin films is measured using the fabricated Hall bar devices under an external magnetic field ($\boldsymbol{H}_{\text{ext}}$). The Hall bar device, the measurement circuit, and the coordinate system are schematically presented in Fig. 2.7. The transport channel is set to a length l and width w, which is the distance between two crossing Hall bars and the width of the transport wire, respectively.

According to the Ohm's law $\boldsymbol{j} = \hat{\sigma}\boldsymbol{E}$ ($\hat{\rho}\boldsymbol{j} = \boldsymbol{E}$), the conductivity σ and the resistivity ρ read as:

$$\boldsymbol{j} = \begin{pmatrix} \sigma_{xx} & \sigma_{xy} \\ \sigma_{yx} & \sigma_{yy} \end{pmatrix} \boldsymbol{E}; \quad \begin{pmatrix} \rho_{xx} & \rho_{xy} \\ \rho_{yx} & \rho_{yy} \end{pmatrix} \boldsymbol{j} = \boldsymbol{E}, \tag{2.2}$$

where $\boldsymbol{j}$ is the current density in the thin film and $\boldsymbol{E}$ is the driving electric field. The unknowns in the conductivity and resistivity tensors are two in isotropic system because of $\sigma_{xx} = \sigma_{yy}$ ($\rho_{xx} = \rho_{yy}$) and $\sigma_{xy} = -\sigma_{yx}$ ($\rho_{xy} = -\rho_{yx}$). By inverting the matrix, the diagonal and the off-diagonal components of the conductivity tensor can be expressed as a function of the elements in resistivity

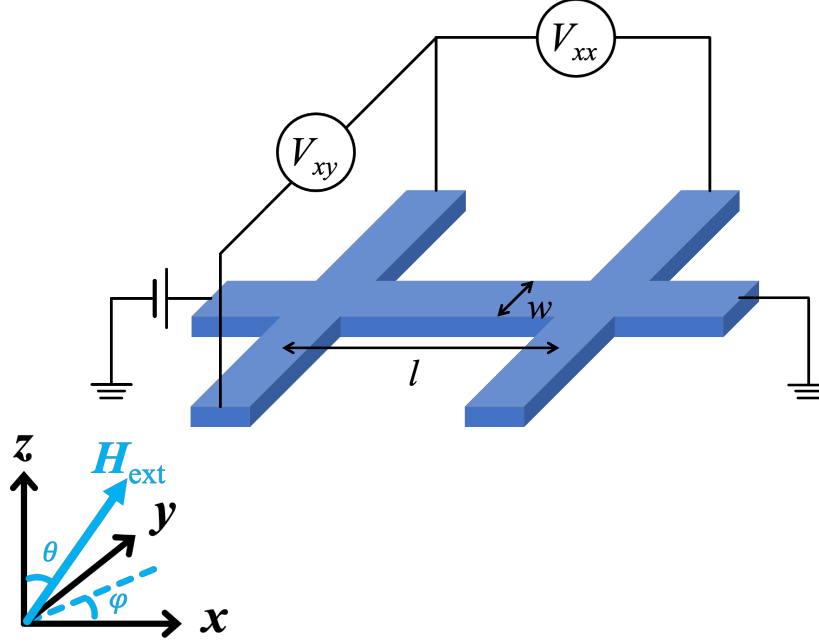

Figure 2.7: Schematic of the Har bar device, DC current transport measurement circuit and coordinate system.

tensor, which read

$$\sigma_{xx} = \left(\frac{\rho_{xx}}{\rho_{xx}^2 + \rho_{yx}^2}\right); \quad \sigma_{xy} = \left(\frac{\rho_{yx}}{\rho_{xx}^2 + \rho_{yx}^2}\right). \tag{2.3}$$

ρ_{yx} is much smaller than ρ_{xx} in most cases. Thus we can simplify Eq. 2.3 as

$$\sigma_{xx} = \frac{1}{\rho_{xx}}; \quad \sigma_{xy} = \frac{\rho_{yx}}{\rho_{xx}^2}. \tag{2.4}$$

ρ_{xx} and ρ_{xy} of the thin films are determined by the longitudinal (R_{xx}) and transverse (R_{xy}) resistance of devices based on the relationship of $\rho_{xx} = R_{xx}l/wt$ and $\rho_{xy} = R_{xy}t$, where t is the thickness of thin films. For heterostructures, ρ_{xx} of different layers can be estimated using the parallel resistor model by measuring R_{xx} of devices with different thicknesses.

R_{xx} under $\boldsymbol{H}_{\text{ext}}$ reads as

$$R_{xx} = \frac{V_{xx}}{I} = R_0\left(1 + \text{MR}(\boldsymbol{H}_{\text{ext}})\right), \tag{2.5}$$

where V_{xx} is the recorded longitudinal voltage, R_0 is the intrinsic resistance of devices, and MR is the magnetoresistance that depends on the direction and strength of $\boldsymbol{H}_{\text{ext}}$. R_{xy} consists of the contributions from ordinary Hall effect, anomalous Hall effect (AHE) and planar Hall effect (PHE). PHE is an effect induced by the anisotropic magnetoresistance in the FM layer. R_{xy} can be expressed using the recorded transverse voltage V_{xy} under $\boldsymbol{H}_{\text{ext}}$ as

$$R_{xy} = \frac{V_{xy}}{I} = \frac{R_{\text{H}}}{t}\mu_0 H_{\text{ext}} \cos\theta + R_{\text{AHE}} \cos\theta + R_{\text{PHE}} \sin^2\theta \sin 2\varphi, \tag{2.6}$$

where R_{H} is the Hall coefficient, μ_0 is the vacuum permeability, R_{AHE} is the anomalous Hall resistance, R_{PHE} is the planar Hall resistance and H_{ext}, θ and φ are the strength, polar angle and azimuthal angle of $\boldsymbol{H}_{\text{ext}}$, respectively.

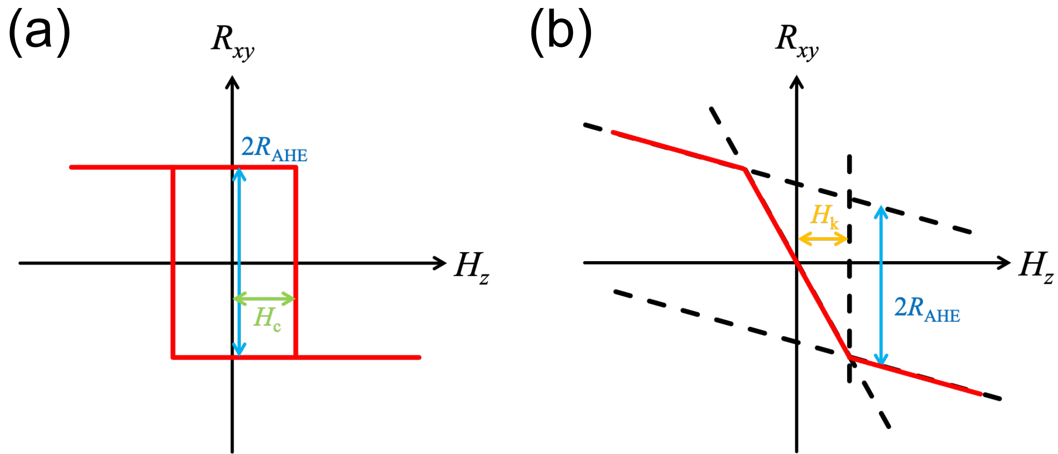

Figure 2.8: Schematics of R_{xy} hysteresis loops for thin films containing FM layer exhibiting perpendicular magnetic anisotropy (a) and in-plane magnetic anisotropy (b).

For non-magnetic material thin films, the carrier concentration n is determined by measuring R_{xy} as a function of $\boldsymbol{H}_{\text{ext}}$ along the z-axis, defined as H_z. R_{H} is obtained from the slope of R_{xy} against H_z. The concentration of carriers n of materials is estimated using $n = |\frac{1}{eR_{\text{H}}}|$ for single-carrier systems. For FM thin films or heterostructures containing FM layer, R_{AHE} is determined by measuring the R_{xy} hysteresis loop using H_z. Schematics of R_{xy} hysteresis loops for samples exhibiting perpendicular magnetic anisotropy (PMA) and in-plane magnetic anisotropy (IMA) are illustrated in Figs. 2.8(a) and (b), respectively. For a thin film exhibiting PMA, R_{AHE} is given by the difference between the

values of R_{xy} at $H_z = 0$ in the two half loops, which is twice the magnitude of R_{AHE}. For the films exhibiting IMA, R_{AHE} is obtained from the extrapolation of the two high-field ordinary Hall effect slopes. The out-of-plane anisotropy field H_{k} is defined as the intersection between the high-field linear curve and the linear fitting of data within a low field regime.

The transport measurements, with high field and variable temperature, are conducted using a Quantum Design Physical Property Measurement System (PPMS®) and a Quantum Design PPMS® DynaCool™. The maximum field in the two systems reaches 9 T and 14 T, respectively. The environment temperature can be tuned from 2 to 400 K. The measurements with low field are carried out using KEITHLEY 2400 and 2450 SourceMeter® and KEITHLEY 2182A nanovoltmeter. Two electromagnets are used in these measurements to generate a magnetic field with a maximum of 2 T.

2.6 Harmonic Hall resistance technique

We use the harmonic Hall resistance technique to characterize the current-induced SOT and quantify current-spin conversion in Bi-based material/FM thin film heterostructures [38, 39, 41, 99, 103, 104]. Schematic of the measurement set-up is illustrated in Fig. 2.9. The principle and analysis of the harmonic Hall resistance technique are described below.

Harmonic Hall resistance R_{har} is measured under $\boldsymbol{H}_{\mathrm{ext}}$ by applying an alternative current (AC) I_{AC}, which reads as

$$I_{\mathrm{AC}} = I_0 \sin \omega t, \tag{2.7}$$

where I_0 and $\omega/2\pi$ are the amplitude and frequency, respectively. The harmonic Hall voltage V_{har} is recorded using lock-in amplifiers. V_{har} consists of contributions from ordinary Hall effect, AHE, PHE, and the magnetothermal effects. The magnetothermal effects originate from an unintentional temperature gradient normal to film plane due to the difference in the thermal conductivities of the substrate and air. The thermal effects include the ONE [99], the anomalous Nernst effect (ANE), and/or the combined action of spin Seebeck effect (SSE) and inverse spin Hall effect (ISHE) [103]. The contribution from the ONE in V_{var} is proportional to H_{ext}.

The contribution from the ANE and/or the combined action of SSE and ISHE is independent of H_{ext}. The magnetization of FM layer $\boldsymbol{M}$ is modulated by $\boldsymbol{H}_{\mathrm{ext}}$ with an equilibrium polar angle θ_M and an azimuthal angle φ_M. Note that we neglect the in-plane easy axis anisotropy energy K_{I} in our model because it is usually small in many soft ferromagnetic materials. The shape isotropy in our device with micrometer size is also negligible. Thus, we assume

φ_M is equal to φ. Eq. 2.6 can be expanded to include the contributions from magnetothermal effect and V_{har} and R_{har} in the bilayer read as:

$$\begin{aligned}V_{\text{har}} =& R_{\text{OHE}}\mu_0 H_{\text{ext}} \cos\theta I_0 \sin\omega t + R_{\text{AHE}} \cos\theta_M I_0 \sin\omega t \\ &+ R_{\text{PHE}} \sin^2\theta_M \sin 2\varphi I_0 \sin\omega t \\ &+ Nw\Delta T H_{\text{ext}} \sin\theta \cos\varphi + \alpha w \Delta T \sin\theta_M \cos\varphi;\end{aligned} \tag{2.8}$$

$$\begin{aligned}R_{\text{har}} = \frac{V_{\text{har}}}{I_0} =& R_{\text{OHE}}\mu_0 H_{\text{ext}} \cos\theta \sin\omega t + R_{\text{AHE}} \cos\theta_M \sin\omega t \\ &+ R_{\text{PHE}} \sin^2\theta_M \sin 2\varphi \sin\omega t \\ &+ \frac{Nw\Delta T}{I_0} H_{\text{ext}} \sin\theta \cos\varphi + \frac{\alpha w \Delta T}{I_0} \sin\theta_M \cos\varphi,\end{aligned} \tag{2.9}$$

where R_{OHE} is a coefficient representing the ordinary Hall resistance of the heterostructure, N is the ONE coefficient, w is the width of the conducting channel in the Hall bar devices, α is the coefficient for ANE and/or SSE/ISHE combination, ΔT is the temperature difference between the top and bottom surfaces of the thin film. During the AC current injection, two oscillating effective fields are generated on $\boldsymbol{M}$ attributed to spin-orbit torque (SOT), i.e., $\boldsymbol{H}_{\text{DL}}$ induced by damping-like spin-orbit torque (DL-SOT) and $\boldsymbol{H}_{\text{FL}}$ induced by field-like spin-orbit torque (FL-SOT), resulting in an oscillation of $\boldsymbol{M}$ from the equilibrium position.

A Joule heating induced in-plane temperature gradient also exists along the direction of Hall bar, i.e., along the y-axis. The voltage induced by ONE and ANE due to an in-plane temperature gradient points along the z-axis. Such voltage does not contribute to the Hall voltage and thus can be neglected in the analysis of $R_{2\omega}$. The SSE of FM layer generates a spin current along the y-axis, which does not contribute to $R_{2\omega}$ through the ISHE. Thus, the effect of in-plane temperature gradient does not influence the analysis of harmonic Hall resistance.

In order to estimate the strength of $\boldsymbol{H}_{\text{DL}}$ and $\boldsymbol{H}_{\text{FL}}$, we first derive the equilibrium θ_{M} of $\boldsymbol{M}$ induced by $\boldsymbol{H}_{\text{ext}}$. Vectors $\boldsymbol{M}$ and $\boldsymbol{H}_{\text{ext}}$ can be written as

$$\boldsymbol{M} = M_{\text{s}} \left(\sin\theta_M \cos\varphi \boldsymbol{i} + \sin\theta_M \sin\varphi \boldsymbol{j} + \cos\theta_M \boldsymbol{k}\right) \tag{2.10}$$

and

$$\boldsymbol{H}_{\text{ext}} = H_{\text{ext}} \left(\sin\theta \cos\varphi \boldsymbol{i} + \sin\theta \sin\varphi \boldsymbol{j} + \cos\theta \boldsymbol{k}\right), \tag{2.11}$$

where M_{s} is the saturation magnetization of $\boldsymbol{M}$. The magnetostatic energy E of the system is given by

$$E = -K_{\text{eff}} \cos^2\theta_M - \boldsymbol{M} \cdot \boldsymbol{H}_{\text{ext}}, \tag{2.12}$$

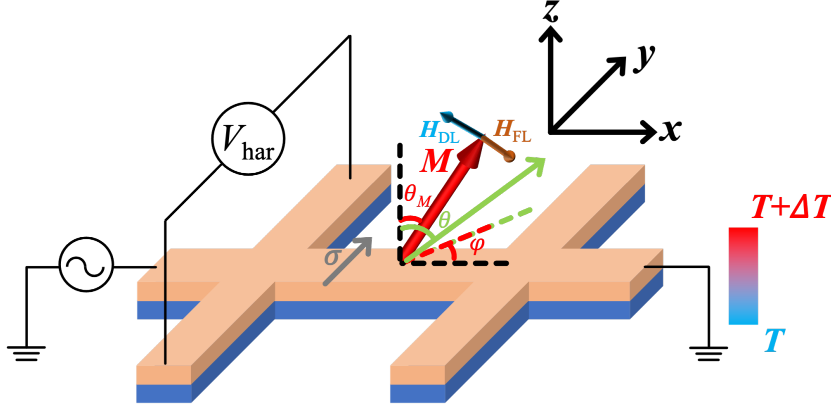

Figure 2.9: Schematic of harmonic Hall resistance measurement circuit, coordinate system and the spin-orbit torque in spin current source material/FM bilayer.

where K_{eff} is the effective out-of-plane magnetic anisotropy energy. The two terms on the right side are attributed to the out-of-plane magnetic anisotropy and Zeeman effect, respectively. θ_M of $\boldsymbol{M}$ is determined by the following equation

$$\frac{\partial E}{\partial \theta_M} = 0 = \frac{H_k}{2} \sin 2\theta_M - H_{\text{ext}} \sin(\theta - \theta_M). \tag{2.13}$$

We define $H_k \equiv 2K_{\text{eff}}/M_{\text{s}}$.

The total current-induced field $\Delta\boldsymbol{H}$ that modulates $\boldsymbol{M}$ can be written in a form of

$$\Delta\boldsymbol{H} = \Delta H_x + \Delta H_y + \Delta H_z. \tag{2.14}$$

The change in equilibrium θ_M and φ of $\boldsymbol{M}$ is defined as $\Delta\theta_M$ and $\Delta\varphi$. $\Delta\varphi$ represents Assuming $\varphi \ll 1$ and $|\Delta\boldsymbol{H}| \ll H_{\text{ext}}$, $\Delta\varphi$ reads as

$$\Delta\varphi = \frac{-\Delta H_x \sin\varphi + \Delta H_y \cos\varphi}{H_{\text{ext}} \sin\theta}. \tag{2.15}$$

$\Delta\theta_M$ can be written as

$$\Delta\theta_M = \sum_{i=x,y,z} \frac{\partial \theta_M}{\partial H_i} \Delta H_i. \tag{2.16}$$

$\partial\theta_M/\partial H_i$ can be calculated using a relation derived from Eq. 2.13:

$$\frac{\partial}{\partial H_i}\left(\frac{\partial E}{\partial \theta_M}\right) = 0 = [H_k \cos 2\theta_M + H_{\text{ext}} \cos(\theta - \theta_M)] \frac{\partial \theta_M}{\partial H_i} - f_i, \tag{2.17}$$

where

$$f_x = \cos\theta_M \cos\varphi; \quad f_y = \cos\theta_M \sin\varphi; \quad f_z = -\sin\theta_M. \tag{2.18}$$

We obtain $\Delta\theta_M$ by substituting the calculated $\partial\theta_M/\partial H_i$ into Eq. 2.16, which reads as

$$\Delta\theta_M = \frac{\cos\theta_M(\Delta H_x \cos\varphi + \Delta H_y \sin\varphi) - \sin\theta_M \Delta H_z}{H_\mathrm{k}\cos 2\theta_M + H_\mathrm{ext}\cos(\theta - \theta_M)}. \tag{2.19}$$

The directions of $\boldsymbol{H}_\mathrm{DL}$ and $\boldsymbol{H}_\mathrm{FL}$ are along $\boldsymbol{\sigma} \times \boldsymbol{m}$ and $\boldsymbol{\sigma}$, respectively. $\boldsymbol{m}$ is the unit vector of $\boldsymbol{M}$. In the geometry of Hall bar device in Fig. 2.9, $\boldsymbol{\sigma}$ is parallel to $\boldsymbol{y}$. An Oersted field $\boldsymbol{H}_\mathrm{Oe}$ induced by the AC current flowing in Bi-based material thin film layer can exert torque on $\boldsymbol{M}$ as well, which has the same geometry of $\boldsymbol{H}_\mathrm{FL}$. $\boldsymbol{H}_\mathrm{DL}$, $\boldsymbol{H}_\mathrm{DL}$, and $\boldsymbol{H}_\mathrm{Oe}$ oscillate in $\sin\omega t$ and their magnitudes, i.e., H_DL, H_DL and H_Oe, are proportional to I_0. Assuming $\boldsymbol{\sigma} = -\boldsymbol{y}$, we obtain the form of $\boldsymbol{H}_\mathrm{DL}$ and $\boldsymbol{H}_\mathrm{FL} + \boldsymbol{H}_\mathrm{Oe}$ as

$$\boldsymbol{H}_\mathrm{DL} = H_\mathrm{DL}(\boldsymbol{y} \times \boldsymbol{m})\sin\omega t = H_\mathrm{DL}(-\cos\theta_M \boldsymbol{i} + \sin\theta_M \cos\varphi \boldsymbol{k})\sin\omega t, \tag{2.20}$$

$$\boldsymbol{H}_\mathrm{FL} + \boldsymbol{H}_\mathrm{Oe} = (H_\mathrm{FL} + H_\mathrm{Oe})\boldsymbol{j}\sin\omega t, \tag{2.21}$$

$\Delta\boldsymbol{H}$ consists of $\boldsymbol{H}_\mathrm{DL}$, $\boldsymbol{H}_\mathrm{DL}$, and $\boldsymbol{H}_\mathrm{Oe}$. Thus, we can use these relations to renormalize $\Delta\boldsymbol{H}$ defined in Eq. 2.14, read as

$$\begin{aligned} \Delta H_x &= -\, H_\mathrm{DL}\cos\theta_M \sin\omega t; \\ \Delta H_y &= -\, (H_\mathrm{FL} + H_\mathrm{Oe})\sin\omega t; \\ \Delta H_z &= H_\mathrm{DL}\sin\theta_M \cos\varphi \sin\omega t. \end{aligned} \tag{2.22}$$

To simplify our measurement, $\boldsymbol{H}_\mathrm{ext}$ is applied with an optimized geometry according to the easy axis of the FM layer in the samples.

2.6.1 In-plane magnetization system

For FM layer exhibiting IMA, $\boldsymbol{H}_\mathrm{ext}$ is rotated in the xy plane with an angel φ between $\boldsymbol{H}_\mathrm{ext}$ and the x-axis. In such geometry, θ and θ_M are 90°. Substituting these values and Eq. 2.22 into Eqs. 2.19 and 2.15, $\Delta\theta_M$ and $\Delta\varphi$ are simplified as

$$\Delta\theta_M = \frac{-H_\mathrm{DL}}{H_k + H_\mathrm{ext}}\cos\varphi\sin\omega t,\ \Delta\varphi = -\frac{H_\mathrm{FL} + H_\mathrm{Oe}}{H_\mathrm{ext}}\cos\varphi\sin\omega t. \tag{2.23}$$

Note that the out-of-plane anisotropy field is negative for samples exhibiting IMA. Here we use H_k to represent its magnitude. The equilibrium angle with

AC current is $\theta'_M = 90° + \Delta\theta_M$ and $\varphi' = \varphi + \Delta\varphi$. We can replace θ_M and φ with θ'_M and φ' in Eq. 2.9 and simplify it as

$$\begin{aligned} R_{\text{har}} =& R_{\text{PHE}} \sin 2\varphi \sin \omega t \\ &+ \left(\frac{Nw\Delta T}{I_0} H_{\text{ext}} + \frac{\alpha w \Delta T}{I_0} + R_{\text{AHE}} \frac{H_{\text{DL}}}{H_{\text{ext}} + H_{\text{k}}} \right) \cos\varphi \sin^2 \omega t \\ &- 2R_{\text{PHE}} \frac{H_{\text{FL}} + H_{\text{Oe}}}{H_{\text{ext}}} \cos 2\varphi \cos\varphi \sin^2 \omega t. \end{aligned} \tag{2.24}$$

$\sin^2 \omega t$ equals to $(1 - \cos 2\omega t)/2$, suggesting that the contributions due to current-induced SOT in Eq. 2.24 appear in the second harmonic Hall resistance term $R_{2\omega}$. ΔT originates from Joule's heating. Using Eq. 2.7, ΔT is given as

$$\Delta T \propto R_0 \cdot I_{\text{AC}}^2 = R_0 \cdot I_0^2 \sin^2 \omega t = R_0 \cdot I_0^2 (1 - \cos 2\omega t)/2. \tag{2.25}$$

Therefore, the contributions induced by the magnetothermal effects in Eq. 2.24 also appear in $R_{2\omega}$. We separate Eq. 2.24 into the first and second harmonic Hall resistance, R_ω and $R_{2\omega}$, as

$$R_\omega = R_{\text{PHE}} \sin 2\varphi, \tag{2.26}$$

and

$$\begin{aligned} R_{2\omega} =& \left(R_{\text{AHE}} \frac{H_{\text{DL}}}{H_{\text{ext}} + H_{\text{k}}} + \frac{Nw\Delta T}{I_0} H_{\text{ext}} + \frac{\alpha w \Delta T}{I_0} \right) \cos\varphi \\ &- 2R_{\text{PHE}} \frac{H_{\text{FL}} + H_{\text{Oe}}}{H_{\text{ext}}} \cos 2\varphi \cos\varphi. \end{aligned} \tag{2.27}$$

In practical measurement, an unintentional misalignment between $\boldsymbol{H}_{\text{ext}}$ and the film plane partly mixes R_{AHE} into the R_ω signal. A modified representation of R_ω is given by adding the R_{AHE} contribution into Eq. 2.26:

$$R_\omega = R_{\text{PHE}} \sin 2\varphi + \zeta R_{\text{AHE}} \cos\varphi, \tag{2.28}$$

where ζ is a constant that is introduced to take into account the unintentional misalignment.

In Eq. 2.27, we have decomposed $R_{2\omega}$ into two parts with different φ dependences, i.e., $\cos\varphi$ and $\cos 2\varphi \cos\varphi$. The prefactors of these two parts are defined as A and B, respectively, read as

$$A \equiv R_{\text{AHE}} \frac{H_{\text{DL}}}{H_{\text{ext}} + H_k} + \frac{Nw\Delta T}{I_0} H_{\text{ext}} + \frac{\alpha w \Delta T}{I_0}, \tag{2.29}$$

and

$$B \equiv -2R_{\text{PHE}} \frac{H_{\text{FL}} + H_{\text{Oe}}}{H_{\text{ext}}}. \tag{2.30}$$

We obtain H_{DL} and $H_{\text{FL}} + H_{\text{Oe}}$ using Eqs. 2.29 and 2.30 after measuring $R_{2\omega}$ under different H_{ext}.

2.6.2 Out-of-plane magnetization system

For samples with FM layer exhibiting PMA, we apply $\boldsymbol{H}_{\text{ext}}$ along the x- and y-axis. In these cases, θ is 90° and φ is 0° for $\boldsymbol{H}_{\text{ext}} \parallel x$ ands 90° for $\boldsymbol{H}_{\text{ext}} \parallel y$. By substituting these values and Eq. 2.22 into Eqs. 2.19 and 2.15, $\Delta\theta_M$ and $\Delta\varphi$ can be rewritten as

$$\Delta\theta_M = \frac{-H_{\text{DL}}}{H_k \cos 2\theta_M + H_{\text{ext}} \sin\theta_M} \sin\omega t,\ \Delta\varphi = -\frac{H_{\text{FL}} + H_{\text{Oe}}}{H_{\text{ext}}} \sin\omega t\ (\boldsymbol{H}_{\text{ext}} \parallel x); \tag{2.31}$$

and

$$\Delta\theta_M = -\frac{H_{\text{FL}} + H_{\text{Oe}}}{H_k \cos 2\theta_M + H_{\text{ext}} \sin\theta_M} \sin\omega t,\ \Delta\varphi = -\frac{H_{\text{DL}}}{H_{\text{ext}}} \cos\theta_M \sin\omega t\ (\boldsymbol{H}_{\text{ext}} \parallel y). \tag{2.32}$$

R_{har} is reexpressed by replacing θ_M and φ with $\theta'_M = 90° + \Delta\theta_M$ and $\varphi' = 0°(90°) + \Delta\varphi$ in Eq. 2.9, which reads as

$$\begin{aligned} R_{\text{har},\boldsymbol{H}_{\text{ext}}||x} =& R_{\text{AHE}}\cos\theta_M \sin\omega t + R_{\text{AHE}} \frac{H_{\text{DL}} \sin\theta_M}{H_k \cos 2\theta_M + H_{\text{ext}} \sin\theta_M} \sin^2\omega t \\ &- 2R_{\text{PHE}} \frac{(H_{\text{FL}} + H_{\text{Oe}}) \sin^2\theta_M}{H_{\text{ext}}} \sin^2\omega t \\ &+ \frac{Nw\Delta T}{I_0} H_{\text{ext}} + \frac{\alpha w \Delta T}{I_0} \sin\theta_M; \end{aligned} \tag{2.33}$$

and

$$\begin{aligned} R_{\text{har},\boldsymbol{H}_{\text{ext}}||y} =& R_{\text{AHE}}\cos\theta_M \sin\omega t + R_{\text{AHE}} \frac{(H_{\text{FL}} + H_{\text{Oe}}) \sin\theta_M \cos\theta_M}{H_k \cos 2\theta_M + H_{\text{ext}} \sin\theta_M} \sin^2\omega t \\ &- 2R_{\text{PHE}} \frac{H_{\text{DL}} \sin^2\theta_M \cos\theta_M}{H_{\text{ext}}} \sin^2\omega t. \end{aligned} \tag{2.34}$$

Similar to Eqs. 2.26 and 2.27, we separate the first and second harmonic terms, giving

$$R_{\omega,\boldsymbol{H}_{\text{ext}}||x \text{ or } y} = R_{\text{AHE}}\cos\theta_M, \tag{2.35}$$

$$\begin{aligned} R_{2\omega,\boldsymbol{H}_{\text{ext}}||x} =& R_{\text{AHE}} \frac{H_{\text{DL}} \sin\theta_M}{H_k \cos 2\theta_M + H_{\text{ext}} \sin\theta_M} - 2R_{\text{PHE}} \frac{(H_{\text{FL}} + H_{\text{Oe}}) \sin^2\theta_M}{H_{\text{ext}}} \\ &+ \frac{Nw\Delta T}{I_0} H_{\text{ext}} + \frac{\alpha w \Delta T}{I_0} \sin\theta_M \end{aligned} \tag{2.36}$$

and

$$R_{2\omega,\boldsymbol{H}_{\mathrm{ext}}||y} = R_{\mathrm{AHE}}\frac{(H_{\mathrm{FL}}+H_{\mathrm{Oe}})\sin\theta_M\cos\theta_M}{H_k\cos 2\theta_M + H_{\mathrm{ext}}\sin\theta_M} - 2R_{\mathrm{PHE}}\frac{H_{\mathrm{DL}}\sin^2\theta_M\cos\theta_M}{H_{\mathrm{ext}}}. \tag{2.37}$$

For a given I_0, H_{DL} and $H_{\mathrm{FL}} + H_{\mathrm{Oe}}$ can be extracted from Eqs. 2.36 and 2.37 by scanning H_{ext} along the x- and y-axis.

Contribution from H_{Oe} can be expressed as $H_{\mathrm{Oe}}/j = -2\pi d_{\mathrm{N}}$ (10^{-1} Oe/(A$\cdot$cm^{-2})) according to Ampère's law [104], where j and d_{N} are the magnitude of the current density and thickness of Bi-based material thin film layer. Thus, we separate H_{FL} from $H_{\mathrm{FL}} + H_{\mathrm{Oe}}$ by subtracting the calculated H_{Oe}. Using the extracted H_{DL} and H_{FL}, we estimate the efficiency of DL-SOT ξ_{DL}, i.e., current-spin conversion efficiency, and the efficiency of FL-SOT ξ_{FL} using Eq. 1.5 by replacing the current density in heavy metal j_{HM} with j:

$$\xi_{\mathrm{DL(FL)}} = \frac{2e}{\hbar}\frac{\mu_0 H_{\mathrm{DL(FL)}}}{j}M_{\mathrm{s}}t_{\mathrm{eff}}, \tag{2.38}$$

where t_{eff} is the thickness of the effective FM layer. In our estimation, we assume that spin is transparent at the interface. We thus assume $\xi_{\mathrm{DL}} \sim \theta_{\mathrm{SH}}$. The corresponding spin Hall conductivity (SHC) σ_{SH} and field-like spin Hall conductivity (FL-SHC) σ_{FL} in Bi-based material thin film are defined using the resistivity ρ_{xx} as

$$\sigma_{\mathrm{SH(FL)}} = \xi_{\mathrm{DL(FL)}}\sigma_{xx} = \xi_{\mathrm{DL(FL)}}/\rho_{xx}. \tag{2.39}$$

Chapter 3

Current-spin conversion in BiSb alloy thin films

Part of this chapter has been published in "The spin Hall effect in Bi-Sb alloys driven by thermal excited Dirac-like electrons", Z. Chi, Y.-C. Lau, X.-D. Xu, T. Ohkubo, K. Hono, and M. Hayashi, Science Advances 6, eaay2324 (2020).

3.1 Introduction

BiSb alloy has attracted great interest in spintronic applications due to its topological property [63,94–97]. It has been reported that BiSb alloy thin film grown by molecular beam epitaxy (MBE) possesses a huge current-spin conversion efficiency due to topological surface state (TSS) at room temperature, allowing current-induced magnetization switching in a BiSb alloy/MnGa thin film heterostructure exhibiting perpendicular magnetic anisotropy (PMA) [98]. However, current-induced spin-orbit torque (SOT) in BiSb alloy/Co bilayer have been reported by a different group, suggesting negligible current-spin conversion in BiSb alloy [99]. Further studies are required to resolve this conflict. In theory, considerable spin Hall conductivity (SHC) has been predicted in Bi-rich BiSb alloy [88], suggesting that current-induced SOT in BiSb alloy may be also generated by bulk spin Hall effect (SHE). Thus, understanding the mechanism behind the SOT in BiSb alloy/ferromagnetic metal (FM) bilayers is of great importance for the better design of spintronic devices based on BiSb.

In this chapter, we present our study on identifying current-spin conversion in polycrystalline $Bi_{1-x}Sb_x$ alloy thin films by characterizing the current-induced SOT in $Bi_{1-x}Sb_x$/CoFeB thin film heterostructures. The $Bi_{1-x}Sb_x$ thickness, composition, film facet, and measurement temperature dependences

of current-spin conversion efficiency and corresponding SHC of $Bi_{1-x}Sb_x$ are discussed in detail.

3.2 Sample description

BiSb alloy/CoFeB thin film heterostructure samples were deposited onto thermally oxidized Si substrates at ambient temperature. The thickness of the oxide layer of the substrate is 100 nm. We utilize the alternating ultrathin layer deposition (AULD) method to grow BiSb alloy layer; the base structure of the heterostructure is Sub./seed/[t_{Bi} Bi|t_{Sb} Sb]$_N$/t_{Bi} Bi/t_{CoFeB} CoFeB/2 MgO/1 Ta (nominal thickness in units of nanometers, nm), which is shown in Fig. 3.1(a) schematically. N is the repeat number of Bi|Sb bilayers. t_{Bi}, t_{Sb}, and t_{CoFeB} represent the thickness of Bi, Sb, and CoFeB unit layer, respectively. The total thickness of the repeated Bi|Sb bilayer is set to satisfy $t_{\mathrm{Bi}} + t_{\mathrm{Sb}} \sim 0.7$ nm. The terminal Bi single layer is fixed to 0.3 nm in all samples. The atomic composition of CoFeB is Co:Fe:B=20:60:20 in the unit of atomic %. The seed layer in the heterostructure is 0.5 nm Ta unless noted otherwise. 2 MgO/1 Ta is used as the capping layer to prevent the heterostructures from oxidization. We assume that the top Ta layer is fully oxidized into TaOx and does not influence the electrical and spin transport properties of the heterostructures.

3.3 Structural and magnetization characterization

The structural and magnetic characterization of the Bi|Sb multilayer/CoFeB heterostructure are presented first. Fig. 3.1(b) illustrates the x-ray diffraction (XRD) spectra of thin films with the structure of 0.5 Ta/[0.35 Bi|0.35 Sb]$_N$/0.3 Bi/2 CoFeB. The red and blue curves show the spectra of samples with $N =$ 8 and 16, respectively. Typical Bragg diffraction peaks, which correspond to (003), (012), and (104) crystallographic directions, are observed, suggesting the films are polycrystalline. The peaks marked by the star is originated from the substrate. The intensity of the peaks increase by increasing the repeat number N of Bi|Sb bilayers, indicating the improved crystal quality of the films.

The roughness of the samples was characterized using atomic force microscopy. The atomic force microscopy image of a 0.5 Ta/[0.35 Bi|0.35 Sb]$_8$/0.3 Bi/2 CoFeB heterostructure is shown in Fig. 3.2. The top figure is the height profile corresponding to the blue solid line in the bottom main image. We find the average peak-to-peak height of crystal grains is less than 3 nm and the root

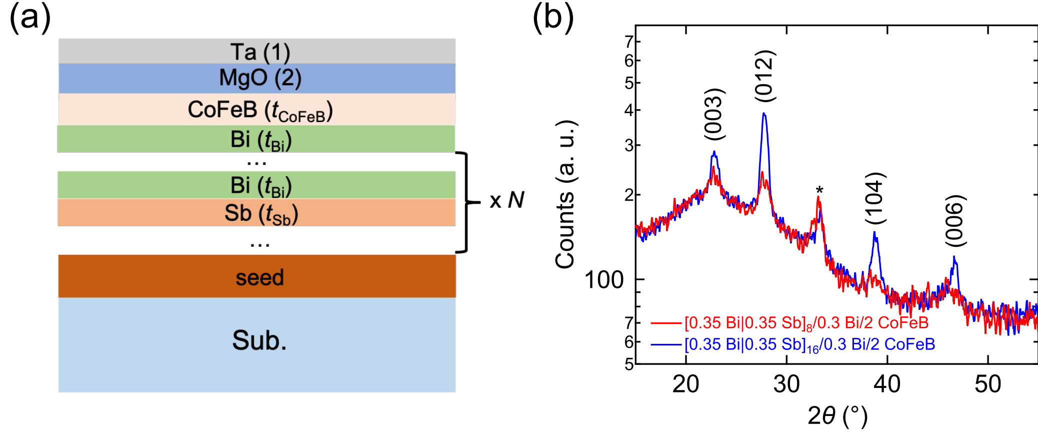

Figure 3.1: XRD spectra of 0.5 Ta/[0.35 Bi|0.35 Sb]$_N$/0.3 Bi/2 CoFeB/2 MgO/1 Ta with N as 8 and 16 shown as blue and red lines, respectively. a.u. means arbitrary units.

mean square roughness is of the order of 1 nm.

High-angle annular dark-field scanning transmission electron microscopy (HAADF-STEM) analysis of samples was performed after cross sectioning the samples into thin lamellae using focused ion beam lift-out technique. Cross-sectional HAADF-STEM images of a thin film with $N = 16$ are shown in Fig. 3.3(a). The top STEM image with lower-magnification confirms that the [Bi|Sb]$_{16}$ layer is continuous. The 2 nm-thick CoFeB and capping layers can be distinguished well from Bi|Sb bilayers and confirmed to follow the morphology and continuity of the multilayer. The average size of the BiSb multilayer crystal grain is ~35 nm. The bottom panel shows the STEM image of the film with high resolution. The lattice fringes can be observed clearly, revealing good crystalinity of the Bi|Sb layers. The inset of Fig. 3.3(a) is a typical nanobeam diffraction pattern of the Bi|Sb bilayers. The diffraction patterns indicate that the crystal grains consist of $Bi_{1-x}Sb_x$ nanocrystallites with random orientations within the film plane.

Figure 3.3(b) shows the element-selected analysis of the HAADF-STEM images of [Bi|Sb]$_{16}$/CoFeB heterostructure obtained via energy-dispersive x-ray spectroscopy (EDS) [105]. EDS line profiles of the atomic ratio for different elements averaged over the entire image are shown in Fig. 3.3(c). We find that Sb tends to diffuse into the CoFeB layer, while Bi is practically immiscible with any other elements. The diffusion of Sb can be attributed to the finite

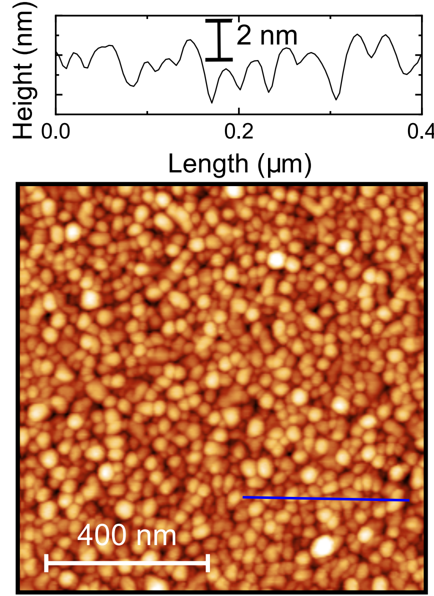

Figure 3.2: Atomic force microscopy image of 0.5 Ta/[0.35 Bi|0.35 Sb]$_8$/0.3 Bi/2 CoFeB/2 MgO/1 Ta sample. The top figure is the line profile along the blue solid line represented in the main image.

solubility of Sb with Co and Fe. The EDS mapping shows that Bi and Sb layers intermix with each other to form an alloy rather other a superlattice, confirming that the AULD method is efficient for growing binary compound alloy. Hereafter, we denote the Bi|Sb bilayers as t_{BiSb} $\mathrm{Bi}_{1-x}\mathrm{Sb}_x$. t_{BiSb} is the total thickness of Bi|Sb bilayers and x is the corresponding Sb concentration defined by $x \equiv \frac{t_{\mathrm{Sb}}}{t_{\mathrm{Bi}}+t_{\mathrm{Sb}}}$. We note the concentration defined by thickness is an apparent value and real value can be different.

The magnetic moments of $\mathrm{Bi}_{1-x}\mathrm{Sb}_x$/CoFeB heterostructures were measured using a vibrating sample magnetometer (VSM) at room temperature. The magnetization hysteresis loops of a 5.6 $\mathrm{Bi}_{0.53}\mathrm{Sb}_{0.47}$/2 CoFeB heterostructure are shown in Fig. 3.4(a). The loops measured under an external magnetic field H_{ext} along (in-plane) and perpendicular to (out-of-plane) the film plane are illustrated by the red and blue lines, respectively. As evident, the magnetic easy axis of CoFeB layer points along the film plane. CoFeB thickness dependence of the saturated magnetic moment of $\mathrm{Bi}_{0.53}\mathrm{Sb}_{0.47}$/ CoFeB heterostructures (t_{BiSb} = 5.6 and 10.9 nm) is presented in Fig. 3.4(b). Little difference is found between the two series of samples. Therefore, we assume that the

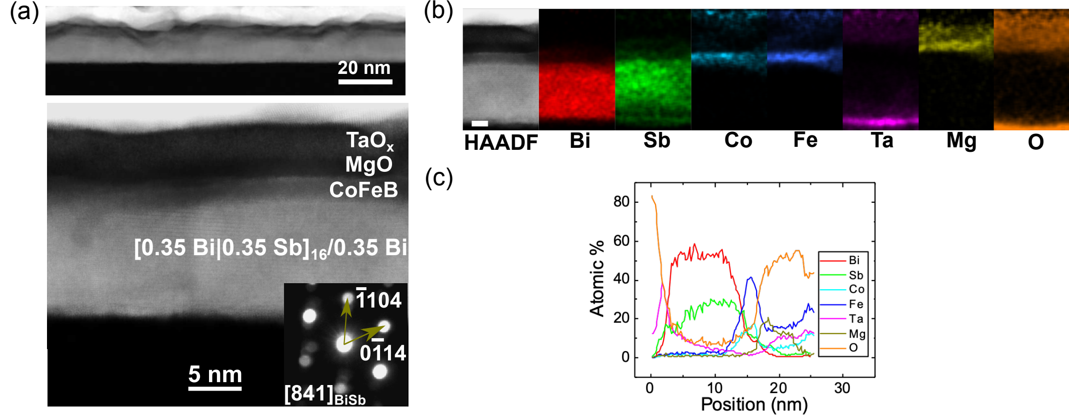

Figure 3.3: (a) Cross-sectional high-angle annular dark-field scanning transmission electron microscopy (HAADF-STEM) image of 0.5 Ta/[0.35 Bi|0.35 Sb]$_{16}$/0.3 Bi/2 CoFeB/2 MgO/1 Ta sample in different ranges. The inset in the bottom image is the selected nanobeam diffraction pattern of the Bi|Sb multilayer. (b) Elemental energy-dispersive x-ray spectroscopy (EDS) maps. The length of the horizontal bar represents ~2 nm. (c) Line profile of the atomic ratio for different elements in the sample. Zero position represents the interface between substrate and heterostructure.

saturation magnetization M_s and the thickness of a magnetic dead layer t_{DL}, if any, are independent of the thickness of the BiSb layer. The solid line in Fig. 3.4(b) is the linear fit of the magnetic moment against t_{CoFeB}. According to the slope and x-intercept of the linear fitting, M_s and t_{DL} are determined as 1190 ± 20 emu/cm^3 and 0.46 ± 0.04 nm, respectively. In addition, we measured the saturated magnetic moment of a 10 Bi/2 CoFeB and a 10 Sb/2 CoFeB heterostructure, which are shown in Fig. 3.4(b) as blue circle and black triangle, respectively. No obvious difference is found in the saturated magnetic moment when x is changed. Thus, we assume that M_s and t_{DL} are constant for all heterostructures with different x.

We used a superconducting quantum interference device to investigate the relationship between the temperature and the magnetic moment of BiSb alloy/CoFeB thin film heterostructures. Fig. 3.5 shows the magnetization hysteresis loops of a 5.6 $Bi_{0.53}Sb_{0.47}$/2 CoFeB heterostructure measured under H_{ext} along the film plane at 300 K and 10 K, which are illustrated by blue and red lines, respectively. The two loops overlap with each other, suggesting that M_s

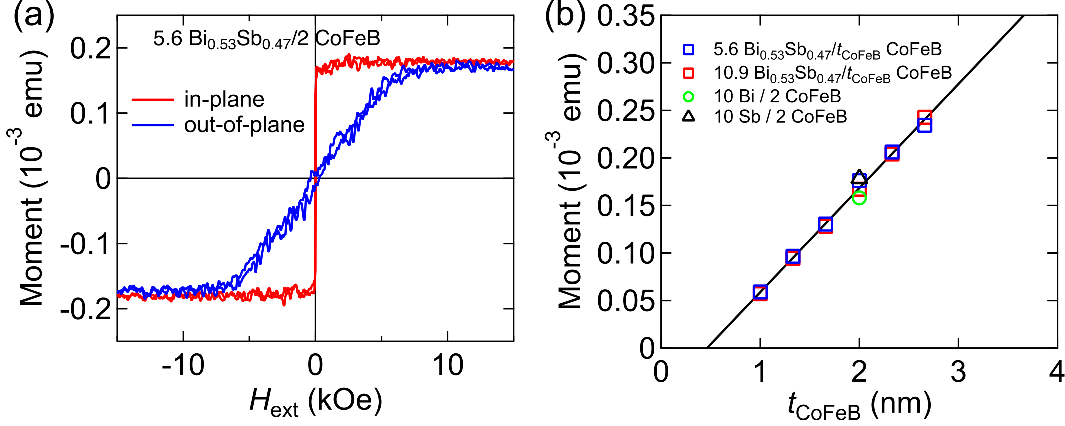

Figure 3.4: (a) Magnetization hysteresis loops of 5.6 $Bi_{0.53}Sb_{0.47}$/2 CoFeB heterostructure. Red and blue curves correspond the hysteresis measured under a field applied along and normal to the film plane, respectively. (b) CoFeB thickness (t_{CoFeB}) dependence of the saturated magnetic moment in 5.6 $Bi_{0.53}Sb_{0.47}/t_{\mathrm{CoFeB}}$ CoFeB (blue squares) and 10.9 $Bi_{0.53}Sb_{0.47}/t_{\mathrm{CoFeB}}$ CoFeB (red squares) heterostructures. The green circle and black triangle represent the saturated magnetic moment of a 10 Bi/2 CoFeB and a 10 Sb/2 CoFeB heterostructure, respectively.

and t_{DL} of CoFeB on $Bi_{1-x}Sb_x$ layer hardly depend on the temperature.

3.4 Current-spin conversion characterization

In order to investigate current-spin conversion in $Bi_{1-x}Sb_x$ alloy, $Bi_{1-x}Sb_x$/CoFeB heterostructures were patterned into Hall bar devices. The width w and length L of the conducting channel of the Hall bar are 10 and 25 μm, respectively. An optical image of a patterned Hall bar device, the measurement circuit, and the coordinate system are illustrated in the inset to Fig. 3.6(a). The longitudinal and transverse resistance, R_{xx} and R_{xy}, are determined using DC current transport measurements. The current-induced SOT in $Bi_{1-x}Sb_x$/CoFeB heterostructures is evaluated using the harmonic Hall technique under different H_{ext}. The field is rotated in the film plane; φ is defined as the angle between H_{ext} and the x-axis. The amplitude and frequency ($\omega/2\pi$) of the applied AC current are 1.5 $\mathrm{mA_{rms}}$ and 17.5 Hz, respectively. The conductivities of BiSb and CoFeB layer, σ_{BiSb} and σ_{CoFeB}, are estimated using a parallel resistor model by

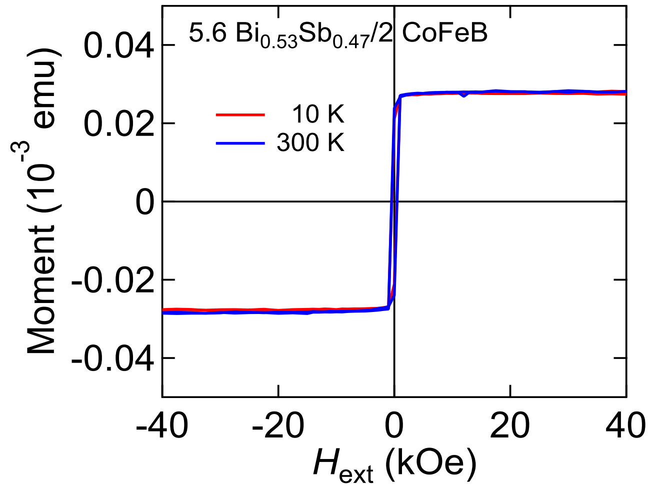

Figure 3.5: Magnetization hysteresis loops of 5.6 $Bi_{0.53}Sb_{0.47}$/2 CoFeB heterostructure measured under a magnetic field applied along the film plane at different temperatures. The red and blue lines correspond to the results obtained at 10 K and 300 K, respectively.

measuring the resistance of samples with different t_{BiSb} and t_{CoFeB}. The current distribution within the heterostructures is calculated using the thickness and conductivities of the conducting layers. Note that we neglect the current conduction in the 0.5 nm Ta seed and capping layers because of their larger resistivity compared to BiSb and CoFeB layers.

3.4.1 BiSb thickness dependence

We first study the layer thickness dependence of current-spin conversion in $Bi_{0.53}Sb_{0.47}$ at room temperature. The conductivity of $Bi_{0.53}Sb_{0.47}$ is plotted as a function of t_{BiSb} in Fig. 3.6(a). The slight increase of σ_{BiSb} with increasing t_{BiSb} is likely due to the larger grain size for thicker films that reduces the scattering at the grain boundaries. The average value of σ_{CoFeB} in $Bi_{0.53}Sb_{0.47}$/CoFeB heterostructures is $\sim 5.5 \times 10^3\ \Omega^{-1} \cdot \mathrm{cm}^{-1}$. Figs. 3.6(b) and (c) show t_{BiSb} dependence of the anomalous Hall resistance R_{AHE} and the out-of-plane anisotropy field H_k, respectively. For a given t_{BiSb}, we studied devices with three different CoFeB thicknesses, i.e., $t_{\mathrm{CoFeB}} \sim 2$, 3.4, and 4.2 nm. $|R_{\mathrm{AHE}}|$ decreases with increasing t_{BiSb} regardless of the thickness of the CoFeB layer. This is caused by current shunting into the BiSb layer due to its reduced resistance with increasing t_{BiSb}. H_k is nearly independent of t_{BiSb} but it increases with increasing t_{CoFeB}. Planar Hall resistance R_{PHE} of $Bi_{0.53}Sb_{0.47}$/CoFeB het-

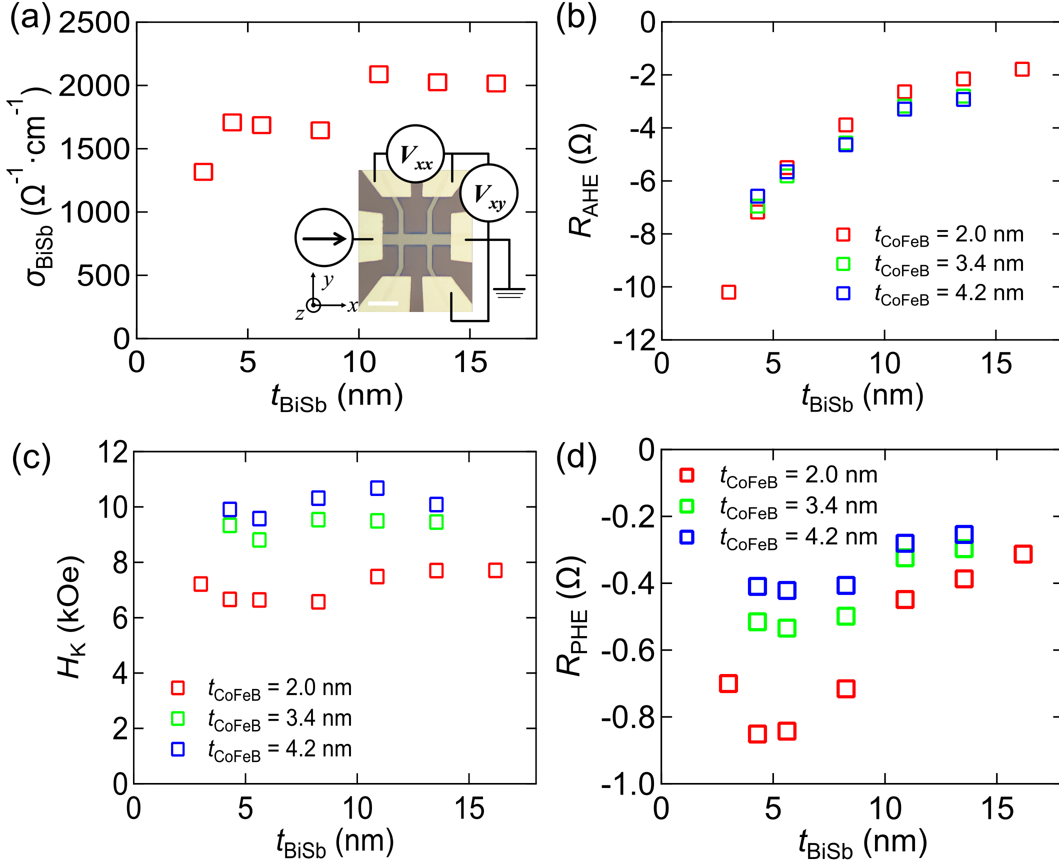

Figure 3.6: BiSb thickness (t_{BiSb}) dependence of the conductivity of BiSb (σ_{BiSb}) (a), anomalous Hall resistance R_{AHE} (b), out-of-plane anisotropy field H_k (c) and planar Hall resistance R_{PHE} (d) in t_{BiSb} BiSb/t_{CoFeB} CoFeB thin film heterostructures. The inset in (a) is the optical image of patterned Hall bar devices, measurement circuit and the corresponding coordinate system. The scale bar represents 30 μm. The All the data were obtained at 300 K.

erostructure is plotted against t_{BiSb} in Fig. 3.6(d). The values are determined using the first harmonic Hall resistance R_ω fitted using Eq. 2.28. Representative φ-dependent R_ω measured under different H_{ext} in a 5.6 $Bi_{0.53}Sb_{0.47}$/2 CoFeB heterostructure are presented in Fig. 3.7. The magnitude and shape of R_ω show little dependence on the change of H_{ext}, indicating good alignment of the sample and magnetic field independent R_{PHE}. The average R_{PHE} obtained under different H_{ext} is used for the analysis hereafter. Note that R_{PHE} contains contribution from the spin Hall magnetoresistance [51, 106]. We find

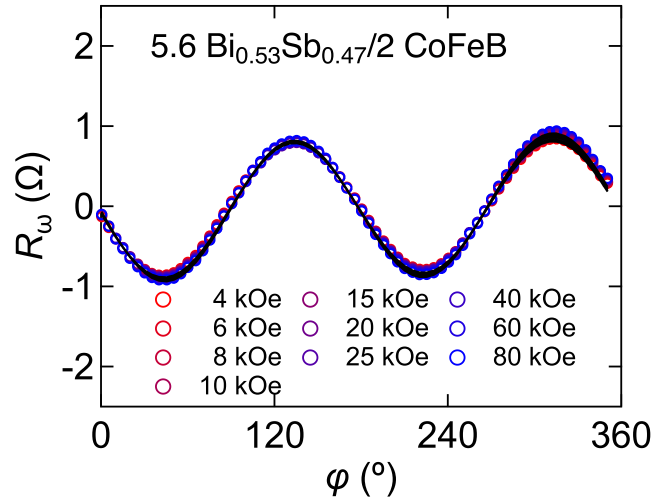

Figure 3.7: Representative azimuthal angle φ dependence of the first harmonic Hall resistance R_ω for 5.6 $Bi_{0.53}Sb_{0.47}$/2 CoFeB thin film heterostructure measured under different external magnetic field H_{ext} at 300 K. The black lines are the fit based on Eq. 2.28.

a peak in $|R_{\text{PHE}}|$ at $t_{\text{BiSb}} \sim 5\,\text{nm}$. Such thickness is approximately twice the spin diffusion length λ of $Bi_{0.53}Sb_{0.47}$ ($\sim 2.3\,\text{nm}$). The position of $|R_{\text{PHE}}|$ peak is in agreement with spin Hall magnetoresistance theory [49].

Representative second harmonic Hall resistance $R_{2\omega}$ measured under different H_{ext} are plotted as a function of φ for 5.6 $Bi_{0.53}Sb_{0.47}$/2 CoFeB and 10.9 $Bi_{0.53}Sb_{0.47}$/2 CoFeB heterostructures in Figs. 3.8(a) and (b), respectively. The black solid lines are the best fittings using Eq. 2.27. We find that the strength of H_{ext} considerably influences the shape and magnitude of $R_{2\omega}$. Fig. 3.8(c) plots the fitting parameter A, i.e., the prefactor of $\cos\varphi$ component in $R_{2\omega}$, as a function of H_{ext} for 10.9 $Bi_{0.53}Sb_{0.47}$/2 CoFeB heterostructure. The black line is the best fitting to A against H_{ext} and colored lines represent the calculated decompositions of different contributions according to Eq. 2.29. The contribution induced by the damping-like spin-orbit torque (DL-SOT) (red line) dominates in A when H_{ext} is small, whereas $R_{2\omega}$ changes its signal and the contribution induced by the ordinary Nernst effect (ONE) (green line) is dominant under high H_{ext}. The large ONE contribution to $R_{2\omega}$ is consistent with the results given by Roschewsky *et al.* [99]. Fig. 3.8(d) displays B, the prefactor of $\cos 2\varphi \cos\varphi$ component in $R_{2\omega}$, against $1/H_{\text{ext}}$. The black line shows the best fitting using Eq. 2.30. The effective fields associated the DL-SOT and field-like spin-orbit torque (FL-SOT), H_{DL} and H_{FL}, can be ex-

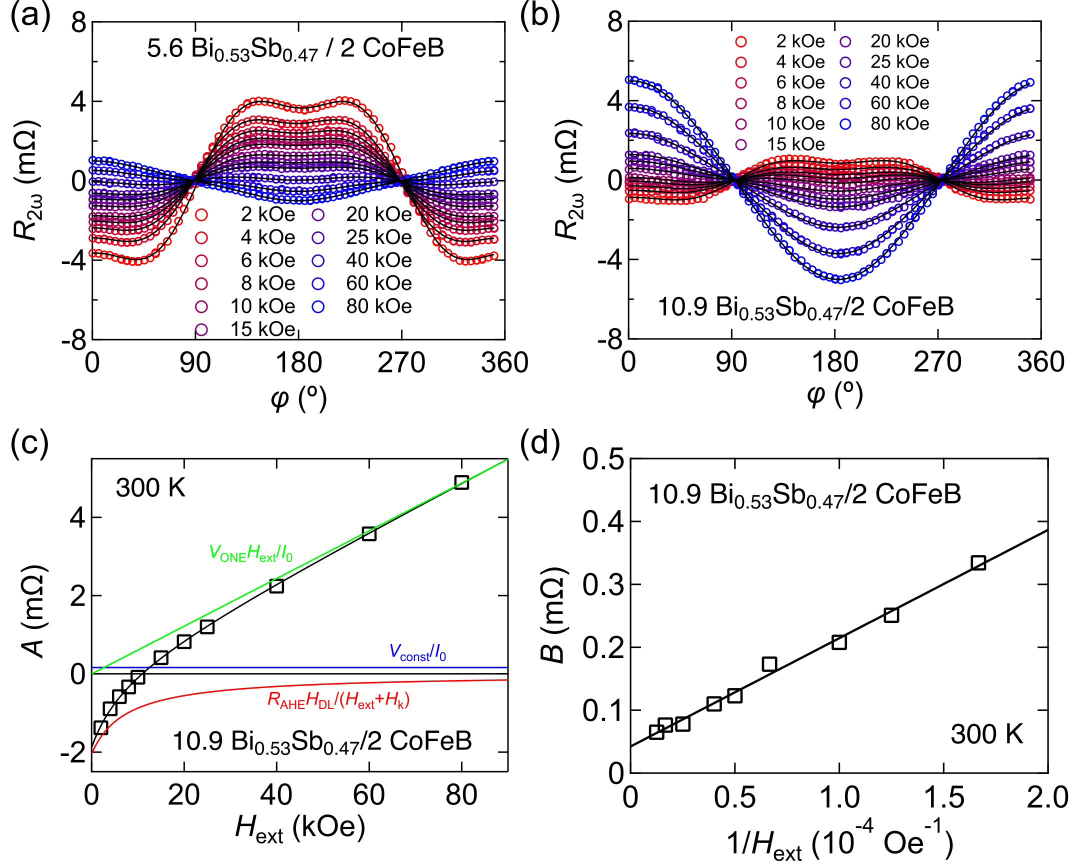

Figure 3.8: (a,b) Representative azimuthal angle φ dependence of the second harmonic Hall resistance $R_{2\omega}$ for 5.6 $Bi_{0.53}Sb_{0.47}$/2 CoFeB (a) and 10.9 $Bi_{0.53}Sb_{0.47}$/2 CoFeB (b) thin film heterostructures measured under different external magnetic field H_{ext} at 300 K. The solid black lines are the fittings following Eq. 2.27. (c) H_{ext} dependence of A in $R_{2\omega}$ for 10.9 $Bi_{0.53}Sb_{0.47}$/2 CoFeB heterostructure. The black curve represents the fitting result according to Eq. 2.29. The colored lines mean the contribution from different origins. (d) $1/H_{\text{ext}}$ dependence of B in $R_{2\omega}$ for 10.9 $Bi_{0.53}Sb_{0.47}$/2 CoFeB. The black line is the fitting result based on Eq. 2.30.

tracted from the fitting in Figs. 3.8(c) and (d). The current-induced Oersted field H_{Oe} is estimated based on the Ampère's law (see Chap. 2). By substituting H_{DL}, H_{FL}, H_{Oe}, R_{AHE}, current density in the BiSb layer j_{BiSb}, M_s and the effective magnetic layer thickness t_{eff} ($t_{\text{eff}} \equiv t_{\text{CoFeB}} - t_{\text{DL}}$) into Eq. 2.38, we obtain the efficiency of DL-SOT ξ_{DL}, which is equivalent to current spin

conversion efficiency, and the efficiency of FL-SOT ξ_{FL} in BiSb/CoFeB thin film heterostructures.

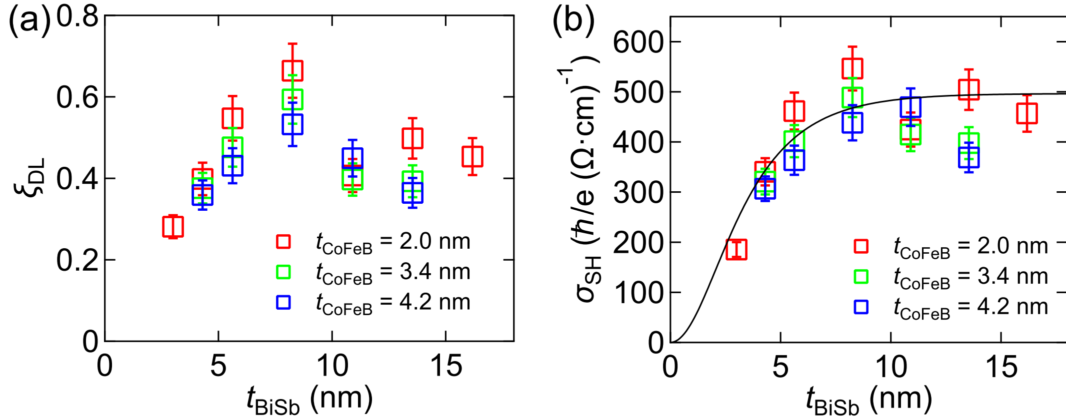

Figure 3.9: t_{BiSb} dependence of the efficiency of DL-SOT ξ_{DL} (a) and spin Hall conductivity σ_{SH} (b) in $Bi_{0.53}Sb_{0.47}$/CoFeB heterostructures with different CoFeB thickness t_{CoFeB}. All the data were measured at 300 K.

The BiSb thickness dependence of ξ_{DL} for $Bi_{0.53}Sb_{0.47}$/CoFeB heterostructures is shown in Fig. 3.9(a). The sign of ξ_{DL} is the same as that of Pt [107], which is in agreement with previous studies on Bi_2Se_3 [72,74] and MBE-grown $Bi_{0.9}Sb_{0.1}$ thin films [98]. ξ_{DL} reaches a maximum of 0.65 at $t_{BiSb} \sim 8\,\text{nm}$. This value is much larger than that of heavy metals (HMs) while a little smaller than found in other Bi-based topological insulators (TIs) [74, 77, 79, 98]. ξ_{DL} is hardly influenced by t_{CoFeB}, indicating current-spin conversion originated from BiSb. ξ_{DL} increases with t_{BiSb} until $\sim 8\,\text{nm}$, whereas it drops slightly at thicker t_{BiSb}. Note that the conductivity of the BiSb layer also varies with its thickness. In order to account for this change, we estimate the SHC (σ_{SH}) of $Bi_{0.53}Sb_{0.47}$ using Eq. 2.39 and plot it as a function of BiSb thickness in Fig. 3.9(b). σ_{SH} increases with increasing t_{BiSb} and tends to saturate when t_{BiSb} is beyond $\sim 8\,\text{nm}$. This trend suggests that current-spin conversion in $Bi_{0.53}Sb_{0.47}$ is likely due to the SHE rather than the scenario dominated by surface states [74,108] or a quantum confinement picture [79]. We fit the data presented in Fig. 3.9(b) using a model based on the spin diffusion equation. Similar to Eq. 1.10, σ_{SH} reads

$$\sigma_{SH} = \bar{\sigma}_{SH}[1 - \text{sech}(\frac{t_{BiSb}}{\lambda})]. \tag{3.1}$$

$\bar{\sigma}_{SH}$ is the bulk SHC and λ is the spin diffusion length. We find that, in $Bi_{0.53}Sb_{0.47}$, $\bar{\sigma}_{SH} = 496 \pm 26$ $(\hbar/e)$ $\Omega^{-1}\cdot cm^{-1}$ and $\lambda = 2.3 \pm 0.4$ nm. The estimated λ is comparable to that of W (~ 1.09 nm) and Ta (~ 0.77 nm) [51].

ξ_{FL} is plotted as a function of t_{BiSb} for $Bi_{0.53}Sb_{0.47}$/CoFeB heterostructures with different t_{CoFeB} in Fig. 3.10. Contribution from H_{Oe} is illustrated by the dotted lines in Fig. 3.10 with colors corresponding to different t_{CoFeB}. We find that H_{Oe} has the opposite sign against H_{FL}. ξ_{FL} shows little dependence on t_{CoFeB} and t_{BiSb}, with an average value of ~ 0.2. The value of ξ_{FL} is nearly half of that of ξ_{DL}. The sign of ξ_{FL} is consistent with that of Pt/Co/AlO_x heterostructures [39] but different from that observed in Bi_2Te_3/Permalloy heterostructures [74]. The different t_{BiSb} dependence of ξ_{DL} and ξ_{FL} suggests that the two orthogonal components of SOT (DL-SOT and FL-SOT) originate from phenomena that are characterized by different characteristic length scales [38, 109].

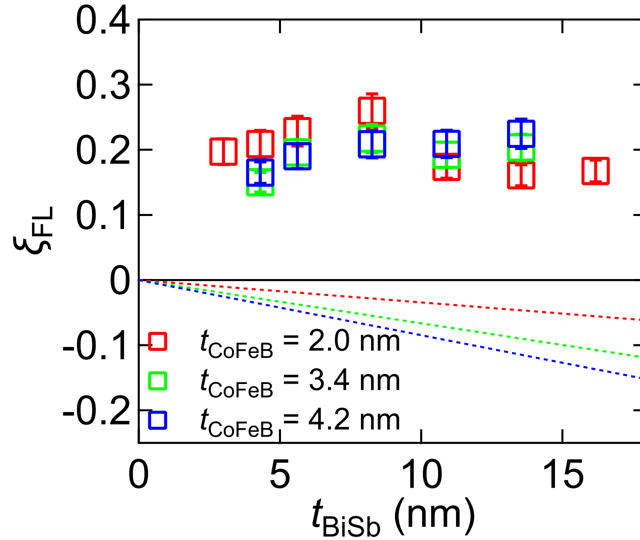

Figure 3.10: BiSb thickness dependence of the efficiency of FL-SOT ξ_{FL} for t_{BiSb} BiSb/t_{CoFeB} CoFeB heterostructures with different t_{CoFeB}. The dotted lines correspond to the contributions from the current-induced Oersted field. All the data were obtained at 300 K.

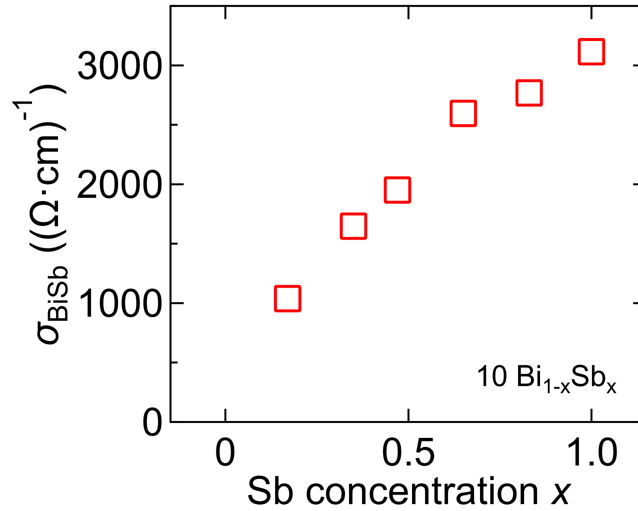

Figure 3.11: Sb concentration x dependence of the conductivity σ_{BiSb} of 10 $\mathrm{Bi}_{1-x}\mathrm{Sb}_x$ thin films. All the data were acquired at 300 K.

3.4.2 BiSb composition dependence

In order to shed light on the origin of the SHE in $\mathrm{Bi}_{1-x}\mathrm{Sb}_x$, we investigate Sb concentration x dependence of current-spin conversion in $\mathrm{Bi}_{1-x}\mathrm{Sb}_x$. Fig. 3.11 shows the Sb concentration dependence of the conductivity σ_{BiSb} of 10 $\mathrm{Bi}_{1-x}\mathrm{Sb}_x$ thin films (without the CoFeB layer, i.e., $t_{\mathrm{CoFeB}} = 0$). σ_{BiSb} increases monotonically with increasing x. This trend is consistent with previous reports on the transport properties of bulk $\mathrm{Bi}_{1-x}\mathrm{Sb}_x$ alloy [110]; $\mathrm{Bi}_{1-x}\mathrm{Sb}_x$ changes from a semiconductor to a semimetal with increasing Sb concentration.

The Hall coefficient R_{H} of $\mathrm{Bi}_{1-x}\mathrm{Sb}_x$ thin films determined by ordinary Hall effect measurement is plotted as a function of x in Fig. 3.12. In our measurement set-up, positive (negative) R_{H} corresponds to majority carrier being electrons (holes). R_{H} decreases monotonically with increasing x and changes its sign smoothly at $x \sim 0.55$, indicating that Bi-rich thin films are electron dominant and the majority carrier is hole for Sb-rich samples. These results reflect the multi-carrier nature of polycrystalline $\mathrm{Bi}_{1-x}\mathrm{Sb}_x$ alloy, i.e., the Fermi level cut at least one electron pocket and one hole pocket. We note that this trend is different from that in $(\mathrm{Bi}_{1-x}\mathrm{Sb}_x)_2\mathrm{Te}_3$ TI where R_{H} abruptly changes its sign when tuning the Fermi level through the Dirac point [76].

Figures 3.12(b) and (c) illustrate R_{AHE} and H_k, respectively, plotted against x in 10 $\mathrm{Bi}_{1-x}\mathrm{Sb}_x$/2 CoFeB heterostructures. $|R_{\mathrm{AHE}}|$ decreases monotonically with increasing x due to increased current shunting to the $\mathrm{Bi}_{1-x}\mathrm{Sb}_x$ layer as

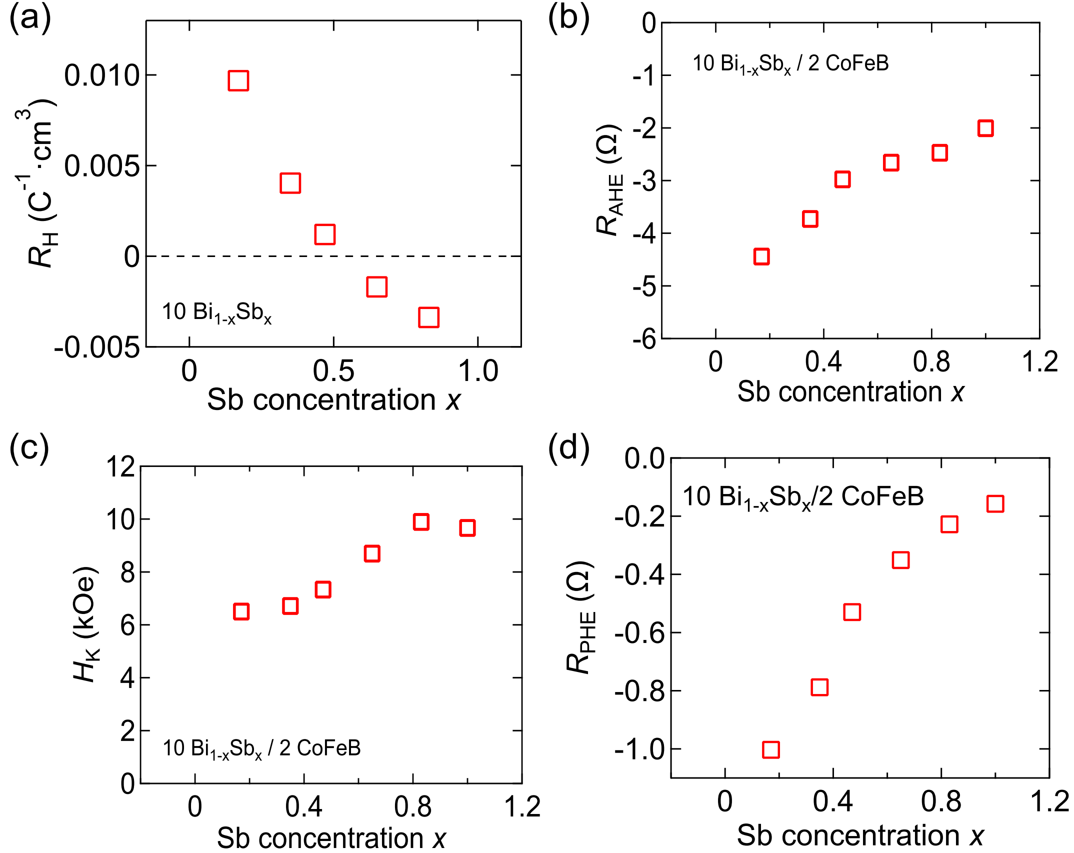

Figure 3.12: (a) Sb concentration x dependence of the Hall coefficient R_{H} for 10 $\mathrm{Bi}_{1-x}\mathrm{Sb}_x$ thin films. (b-d) x dependence of the anomalous Hall resistance R_{AHE} (b), out-of-plane anisotropy field H_k (c), and planar Hall resistance R_{PHE} (d) for 10 $\mathrm{Bi}_{1-x}\mathrm{Sb}_x$/2 CoFeB heterostructures. All the data were acquired at 300 K.

σ_{BiSb} increases with increasing x. H_k slightly increases with increasing x. Although the mechanism of this change is unclear, variation in H_k indicates that the PMA, which is predominantly defined at the CoFeB/MgO interface, is affected by the choice of underlayer [111]. R_{PHE} of the $\mathrm{Bi}_{1-x}\mathrm{Sb}_x$/CoFeB heterostructures is plotted as a function of x in Fig. 3.12(d). $|R_{\mathrm{PHE}}|$ decreases with increasing x, which is also attributed to the current redistribution between the $\mathrm{Bi}_{1-x}\mathrm{Sb}_x$ and CoFeB layers for different x.

ξ_{DL} and σ_{SH} for 10 $\mathrm{Bi}_{1-x}\mathrm{Sb}_x$/2 CoFeB heterostructures are plotted as a function of x in Fig. 3.13(a) by red and blue hollow squares, respectively. ξ_{DL} increases with increasing Bi concentration, reaching a maximum of ~ 1.2

for $x \sim 0.17$. Although $Bi_{1-x}Sb_x$ with x between 0.07 and 0.22 is known to form a TI, we emphasize that both BiSb thickness dependence of σ_{SH} and the facet orientation dependent analysis, which will be presented in the next section, suggest that current-spin conversion in $Bi_{0.83}Sb_{0.17}$ alloy is due to the SHE dominated by its bulk property. σ_{SH} also increases with increasing Bi concentration. However, a plateau of $\sigma_{SH} \sim 600$ $(\hbar/e)$ $\Omega^{-1}\cdot\text{cm}^{-1}$ is observed for $x < 0.35$. The strength of SHC in $Bi_{0.83}Sb_{0.17}$ thin film is comparable to that in HM W [34] and TI Bi_2Se_3 [74]. The value and the trend of σ_{SH} against x are surprisingly consistent with the calculation based on a tight-binding model (shown by the blue line in Fig. 3.13(a)) [88]. This agreement suggests that the intrinsic value of σ_{SH} is observed in $Bi_{1-x}Sb_x$ and the SHE here is likely to have a dominant intrinsic contribution from the band structure instead of the extrinsic side-jump or skew scattering. ξ_{FL} against Sb concentration x is presented in Fig. 3.13(b). Similar to ξ_{DL}, ξ_{FL} increases monotonically with increasing Bi concentration, although its value is around half of that of ξ_{DL}.

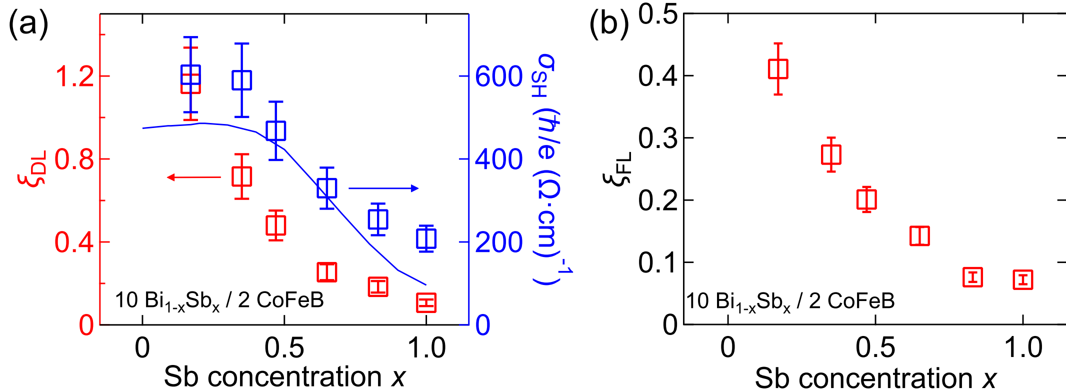

Figure 3.13: (a) Sb concentration x dependence of the efficiency of DL-SOT ξ_{DL} (red squares, left axis) and spin Hall conductivity σ_{SH} (blue squares, right axis) in 10 $Bi_{1-x}Sb_x$/2 CoFeB heterostructures. The blue line is the calculated Sb concentration dependence of σ_{SH} based on a tight-binding model reproduced from Ref. [88]. (b) The efficiency of FL-SOT ξ_{FL} plotted against x. All the data were gotten at 300 K.

3.4.3 Facet dependence

We have also studied the facet orientation dependence of the current-spin conversion by growing thin films on different seed layers. Figure 3.14(a) shows the XRD spectra of 8.9 $Bi_{0.53}Sb_{0.47}$ thin films grown on different seed layers. Here we replace the 0.5 Ta seed layer with 0.5 Ta/2 Te (red) or 2 MgO (blue). The unit of the thicknesses is nm. The orientation of $Bi_{0.53}Sb_{0.47}$ thin film is changed from practically random (0.5 Ta, see in Fig. 3.1) to contain a dominant (003) (0.5 Ta/2 Te) or (012) (2 MgO) preferential growth. The Sb concentration dependence of σ_{BiSb} in 10 $Bi_{1-x}Sb_x$ thin films grown on different seed layers is shown in Fig. 3.14(b). σ_{BiSb} shows little dependence on x for $Bi_{1-x}Sb_x$ thin films grown on 0.5 Ta/2 Te seed layer. The trend of σ_{BiSb} in $Bi_{1-x}Sb_x$ thin films grown on 2 MgO seed layer is similar to that of $Bi_{1-x}Sb_x$ thin films grown on 0.5 Ta seed layer, which increases monotonically with increasing x. However, the values of σ_{BiSb} are different between these two sets, especially in the thin regime. We consider the texture of $Bi_{1-x}Sb_x$ thin films influences its longitudinal conductivity.

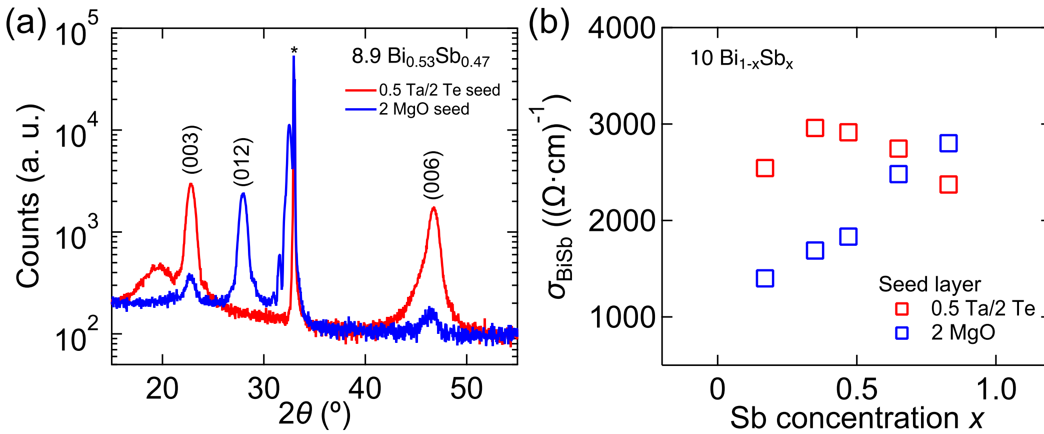

Figure 3.14: (a) XRD spectra of 8.9 $Bi_{0.53}Sb_{0.47}$ thin films grown on 0.5 Ta/2 Te (red) 2 MgO (blue) seed layers. (b) Sb concentration dependence of the conductivity of 10 $Bi_{1-x}Sb_x$ thin films with 0.5 Ta/2 Te (red squares) and 2 MgO (blue squares) seed layers. All the data were acquired at 300 K.

Figure 3.15(a) illustrates the Sb concentration dependence of ξ_{DL} in 10 $Bi_{1-x}Sb_x$/2 CoFeB heterostructures grown on 0.5 Ta/2 Te and 2 MgO seed layers. ξ_{DL} increases with increasing Bi concentration, whereas the rate of the

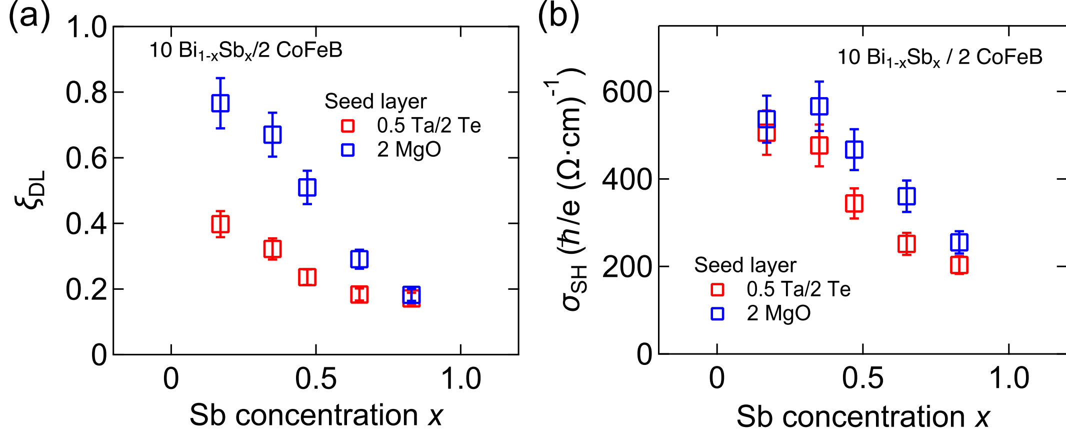

Figure 3.15: Sb concentration x dependence of the efficiency of DL-SOT ξ_{DL} (a) and spin Hall conductivity σ_{SH} (b) obtained from 10 $\text{Bi}_{1-x}\text{Sb}_x$/2 CoFeB heterostructures grown on 0.5 Ta/2 Te (red) and 2 MgO (blue) seed layers. All the data were measured at 300 K.

increase against x is slower for heterostructures grown on 0.5 Ta/2 Te. The corresponding SHC is shown in Fig. 3.15(b). The x dependence of the SHC in $\text{Bi}_{1-x}\text{Sb}_x$ is robust against the change of $\text{Bi}_{1-x}\text{Sb}_x$ texture and longitudinal conductivity. The TSS of $\text{Bi}_{1-x}\text{Sb}_x$ is intimately related to the facet orientation [96, 112]. If TSS exists in our polycrystalline samples and contribute to current-spin conversion, the SHC of BiSb should have depended on the facet orientation. Although contribution from the TSS on the overall current conduction may be negligibly small, the thickness dependence of σ_{SH} suggest that current-spin conversion in BiSb is predominantly caused by the SHE. Therefore, we assume that the TSS of $\text{Bi}_{1-x}\text{Sb}_x$, if present, plays little role in current-spin conversion. The robustness of SHC against σ_{BiSb} also consolidates our suggestion that the observed SHE in $\text{Bi}_{1-x}\text{Sb}_x$ is due to an intrinsic mechanism.

3.4.4 Temperature dependence

To provide further information on the origin of the SHE in $\text{Bi}_{1-x}\text{Sb}_x$, we investigate the temperature dependence of transport and current-spin conversion properties of 10 $\text{Bi}_{1-x}\text{Sb}_x$/2 CoFeB heterostructures with selected x (x =0.17, 0.47, and 0.65). Here, the seed layer is fixed to 0.5 Ta.

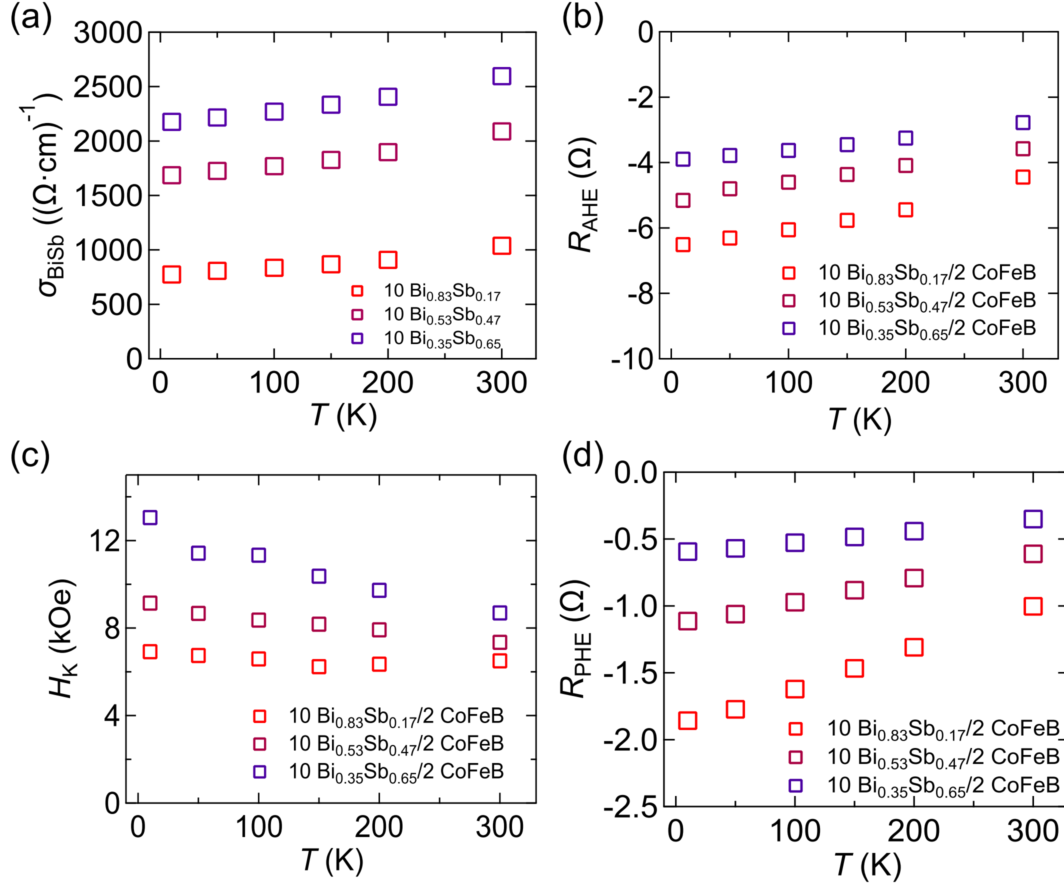

Figure 3.16: (a) Temperature dependence of σ_{BiSb} for 10 $\mathrm{Bi}_{1-x}\mathrm{Sb}_x$ thin films. (b-d) Temperature dependence of the anomalous Hall resistance R_{AHE} (b), anisotropy field H_{k} and planar Hall resistance R_{PHE} for 10 $\mathrm{Bi}_{1-x}\mathrm{Sb}_x$/2 CoFeB heterostructures.

The conductivity of 10 $\mathrm{Bi}_{1-x}\mathrm{Sb}_x$ thin films with different x is plotted as a function of temperature in Fig. 3.16(a). σ_{BiSb} slightly increases with increasing temperature regardless of x. This is a typical characteristic of semiconductors or semimetals. The temperature dependence of R_{AHE}, H_k, and R_{PHE} for 10 $\mathrm{Bi}_{1-x}\mathrm{Sb}_x$/2 CoFeB heterostructures are shown in Figs. 3.16(b), (c), and (d), respectively. For all x studied, $|R_{\mathrm{AHE}}|$, H_k, and $|R_{\mathrm{PHE}}|$ decrease with increasing temperature. The changes of R_{AHE} and R_{PHE} are mainly due to the different temperature dependences of the conductivity between the $\mathrm{Bi}_{1-x}\mathrm{Sb}_x$ and CoFeB layers. As shown in Fig. 3.16(a), σ_{BiSb} increases slightly with temperature,

whereas the conductivity of CoFeB is almost independent of temperature [113]. This difference results in redistribution of current flowing in the two layers upon changing temperature.

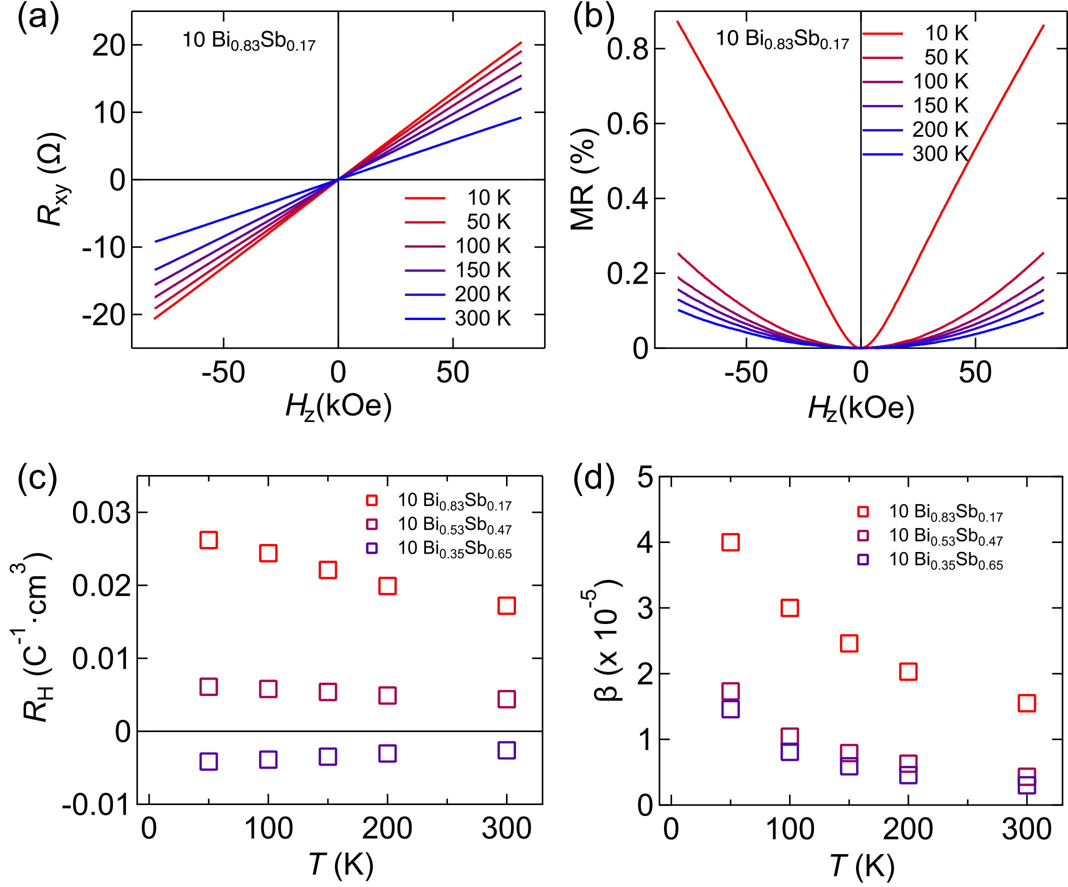

Figure 3.17: (a,b) Field dependence of the ordinary Hall resistance R_{xy} (a) and magnetoresistance (b) for 10 $Bi_{0.83}Sb_{0.17}$ thin film measured under different temperature. (c-d) Hall coefficient R_H (c) and magnetoresistance coefficient β (d) for 10 $Bi_{1-x}Sb_x$ with different Sb concentration x plotted as a function of temperature.

As described in Section 3.4.2, both electrons and holes contribute to carrier transport in BiSb. Therefore, we utilize a classical two-carrier model [114] to estimate the concentration and mobility of carriers in the thin films without the CoFeB layer. The experimental inputs of the model include R_H, σ_{BiSb} at $H_{ext} = 0$, and the quadratic component of the longitudinal magnetoresistance

measured under an out-of-plane external magnetic field H_z. The relations obtained from the model reads [115]:

$$R_{\mathrm{H}} = \frac{1}{e}\frac{(n_{\mathrm{e}}\mu_{\mathrm{e}}^2 - n_{\mathrm{h}}\mu_{\mathrm{h}}^2) - (n_{\mathrm{h}} - n_{\mathrm{e}})\,\mu_{\mathrm{h}}^2\mu_{\mathrm{e}}^2(\mu_0 H_z)^2}{(n_{\mathrm{h}}\mu_{\mathrm{h}} + n_{\mathrm{e}}\mu_{\mathrm{e}})^2 + (n_{\mathrm{h}} - n_{\mathrm{e}})^2\,\mu_{\mathrm{h}}^2\mu_{\mathrm{e}}^2(\mu_0 H_z)^2}, \tag{3.2}$$

$$\sigma_{\mathrm{BiSb}} = e\,(n_{\mathrm{h}}\mu_{\mathrm{h}} + n_{\mathrm{e}}\mu_{\mathrm{e}})\,, \tag{3.3}$$

and

$$\begin{aligned}\mathrm{MR} =& \frac{\rho_{\mathrm{BiSb}}\,(\mu_0 H_z) - \rho_{\mathrm{BiSb}}\,(\mu_0 H_z = 0)}{\rho_{\mathrm{BiSb}}\,(\mu_0 H_z = 0)} \\ =& \frac{n_{\mathrm{e}}\mu_{\mathrm{e}}n_{\mathrm{h}}\mu_{\mathrm{h}}\,(\mu_{\mathrm{h}} + \mu_{\mathrm{e}})^2\,(\mu_0 H_z)^2}{(n_{\mathrm{h}}\mu_{\mathrm{h}} + n_{\mathrm{e}}\mu_{\mathrm{e}})^2 + (n_{\mathrm{h}} - n_{\mathrm{e}})^2\,(\mu_{\mathrm{h}}\mu_{\mathrm{e}})^2\,(\mu_0 H_z)^2}.\end{aligned} \tag{3.4}$$

n_{e} (n_{h}) and μ_{e} (μ_{h}) are the carrier concentration and mobility of electrons (holes), respectively. We assume that $n_{\mathrm{e}}{\approx}n_{\mathrm{h}}{\equiv}n$ for all $\mathrm{Bi}_{1-x}\mathrm{Sb}_x$ thin films since Bi and Sb have the same number of valence electrons. Eqs. 3.2, 3.3 and 3.4 are then simplified as

$$R_{\mathrm{H}} = \frac{ne\,(\mu_{\mathrm{e}}^2 - \mu_{\mathrm{h}}^2)}{\sigma_{\mathrm{BiSb}}^2}, \tag{3.5}$$

$$\sigma_{\mathrm{BiSb}} = ne\,(\mu_{\mathrm{h}} + \mu_{\mathrm{e}})\,, \tag{3.6}$$

and

$$\mathrm{MR} = \mu_{\mathrm{e}}\mu_{\mathrm{h}}(\mu_0 H_z)^2 = \beta(\mu_0 H_z)^2. \tag{3.7}$$

n, μ_{e}, and μ_{h} are estimated by substituting the parameters obtain by the experiments into these equations. Representative temperature dependences of R_{xy} and magnetoresistance for 10 $\mathrm{Bi}_{0.83}\mathrm{Sb}_{0.17}$ thin films are shown in Figs. 3.17(a) and (b), respectively. Both R_{xy} and magnetoresistance are plotted as a function of H_z. Figs. 3.17(c) and (d) present the temperature dependence of the extracted R_{H} and β, respectively. We note that a quasi-linear magnetoresistance is observed at 10 K, which is attributed to the weak anti-localization originating from the strong spin-orbit coupling of Bi [116]. Therefore, we limit our estimation of carrier concentration and mobility to temperature ranging from 50 K to 300 K.

The estimated carrier concentration n of 10 $\mathrm{Bi}_{1-x}\mathrm{Sb}_x$ thin films with different x is plotted as a function of temperature in Fig. 3.18. n increases with increasing temperature for all x studied here. We infer this enhancement is due

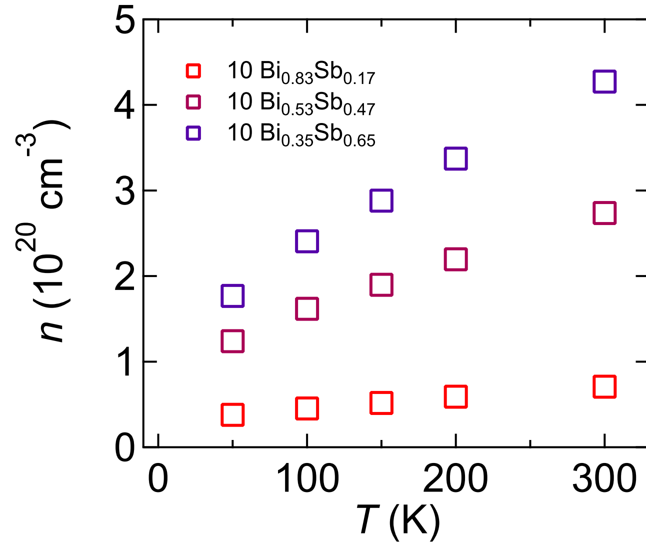

Figure 3.18: Temperature dependence of the carrier concentration n of 10 $\mathrm{Bi}_{1-x}\mathrm{Sb}_x$ thin films with different Sb concentration x.

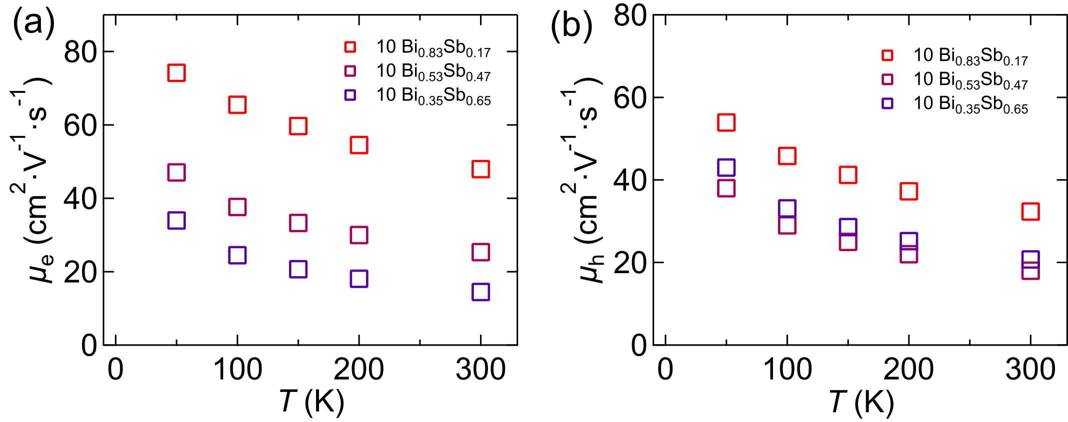

Figure 3.19: Temperature dependence of the mobility of electron μ_e (a) and hole μ_h (b) of 10 $\mathrm{Bi}_{1-x}\mathrm{Sb}_x$ thin films with different Sb concentration x.

to thermal broadening of the Fermi-Dirac distribution. Figs. 3.19(a) and (b) show the temperature dependences of μ_e and μ_h, respectively. In contrast to n, both μ_e and μ_e decrease with increasing temperature. The carrier concentration at 77 K for bulk single-crystal Bi and Sb are $\sim 4.6 \times 10^{17}\,\mathrm{cm}^{-3}$ and $\sim$

$3.9 \times 10^{19}\,\mathrm{cm}^{-3}$, respectively [82, 117]. At the same temperature, the mobility of electron in Bi is $\mu_\mathrm{e} \sim 6 \times 10^5\,\mathrm{cm}^2{\cdot}\mathrm{V}^{-1}{\cdot}\mathrm{s}^{-1}$ [82] and the mobility of hole in Sb is $\mu_\mathrm{h} \sim 2 \times 10^4\,\mathrm{cm}^2{\cdot}\mathrm{V}^{-1}{\cdot}\mathrm{s}^{-1}$ [117]. From Fig. 3.18 and Fig. 3.19, we observe the carrier concentration of $\mathrm{Bi}_{1-x}\mathrm{Sb}_x$ thin films increases with increasing x, whereas the mobilities decrease with increasing x. These trends are consistent with those of bulk Bi and Sb single crystals. However, the values of n in the thin films studied here are one to two orders of magnitude larger than that of bulk and the mobility are several orders of magnitude lower. These differences are expected as the defect density contained in sputtered polycrystalline thin films is likely significantly higher than that of bulk single crystals [90].

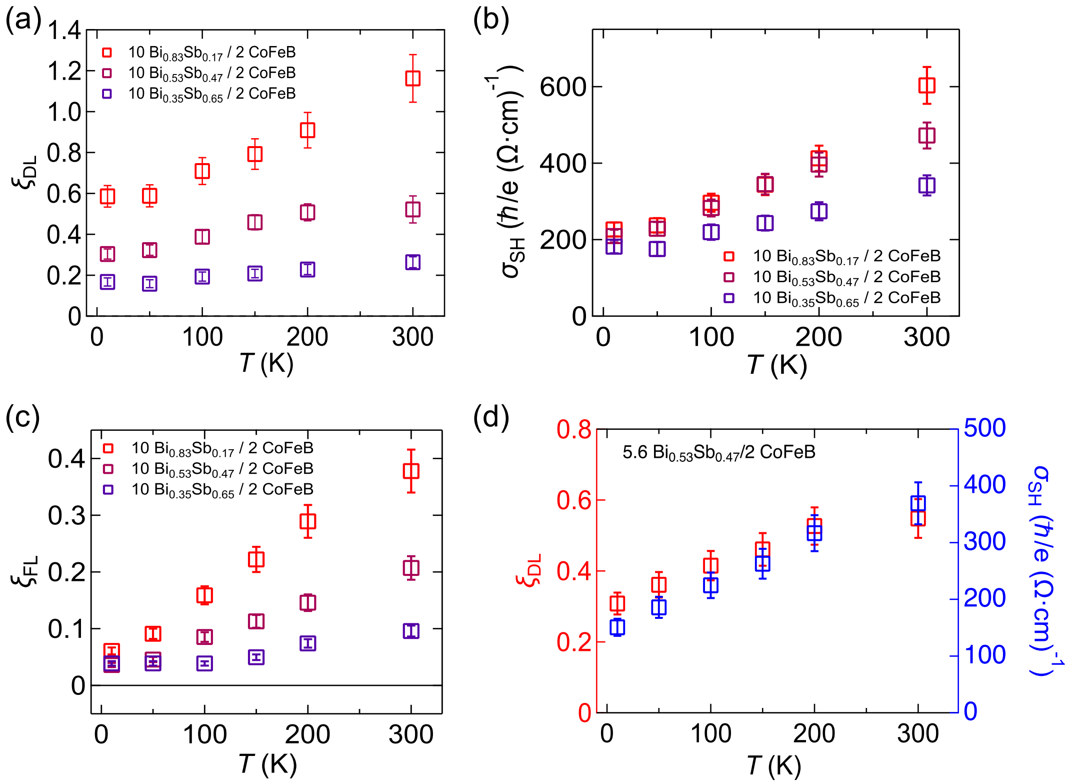

Figure 3.20: (a-c) Temperature dependence of ξ_DL (a), σ_SH (b) and ξ_FL (c) in 10 $\mathrm{Bi}_{1-x}\mathrm{Sb}x$/2 CoFeB thin film heterostructures with different Sb concentration x. (d) Temperature dependence of ξ_DL and corresponding σ_SH in 5.6 $\mathrm{Bi}_{0.53}\mathrm{Sb}_{0.47}$/2 CoFeB thin film heterostructure.

The temperature dependences of ξ_DL and the corresponding σ_SH in 10 $\mathrm{Bi}_{1-x}\mathrm{Sb}_x$/2 CoFeB heterostructures with different x are shown in Figs. 3.20(a)

and (b), respectively. Surprisingly, both ξ_{DL} and σ_{SH} increase with increasing temperature from 10 K to room temperature. These results are in contrast to what has been observed in HM/FM thin film heterostructures, where the ξ_{DL} decreases with increasing temperature [35] or is independent of temperature [109]. The most significant change is observed in $\mathrm{Bi_{0.83}Sb_{0.17}}$/CoFeB, where ξ_{DL} (σ_{SH}) increases by a factor of two (three) from 10 K to 300 K. The temperature dependence of ξ_{DL} (σ_{SH}) may originate from the temperature dependence of λ or M_{s} (see Eqs. 2.38 and 3.1). Fig. 3.20(d) illustrates the temperature dependence of ξ_{DL} and σ_{SH} in another $\mathrm{Bi_{0.53}Sb_{0.47}}$/CoFeB heterostructure, with a different BiSb thickness ($t_{\mathrm{BiSb}} \sim 5.6$ nm). ξ_{DL} and σ_{SH} increase with increasing temperature in the same manner as that of the thicker BISb/CoFeB film, suggesting that λ is not changing with temperature. We have verified that the saturation magnetization of CoFeB hardly changes with temperature (see Fig. 3.5). Thus, we exclude possibilities that temperature dependence of ξ_{DL} in $\mathrm{Bi_{1-x}Sb_x}$/CoFeB heterostructure is caused by variation in the spin diffusion length or CoFeB magnetization with the temperature. The change in ξ_{DL} (σ_{SH}) with temperature should be attributed to the temperature-dependent σ_{SH} of $\mathrm{Bi_{1-x}Sb_x}$.

Figure 3.20(c) presents the temperature dependence of ξ_{FL} in $\mathrm{Bi_{1-x}Sb_x}$/CoFeB thin film heterostructures. ξ_{FL} increases with increasing temperature. However, ξ_{FL} approaches zero by decreasing temperature while ξ_{DL} is finite at 10 K for all x studied here. The value of ξ_{FL} is nearly half of that of ξ_{DL} The differences on the trend and strength between ξ_{DL} and ξ_{FL} reconfirm our suggestion proposed above: the origin of the DL-SOT and FL-SOT should be attributed to different phenomena.

3.5 Discussion

As introduced in Chap. 1, the mechanism of the SHE can be distinguished according to the relaxation time τ dependence of σ_{SH}: $\sigma_{\mathrm{SH}} \propto \tau^1$ in the case of extrinsic skew scattering and $\sigma_{\mathrm{SH}} \propto \tau^0$ when the intrinsic or extrinsic side-jump mechanism dominates. Within the Drude model, τ is characterized by the mobility via the relation: $\mu = e\tau/m^*$, where m^* is the effective mass of carrier. With regard to the relation with n, the intrinsic contribution of SHE should scale with n if the analogy to the anomalous Hall effect (AHE) applies (see Fig. 3.21) [118]. Calculations have also pointed out a similar scaling see between σ_{SH} and n for the extrinsic SHE [119]. Thus, one must take the ratio σ_{SH}/n to eliminate the effect of n on σ_{SH} to study its scaling with τ. Here, we regard σ_{SH}/n as the equivalent carrier mobility of transverse spin current and define it as spin current mobility.

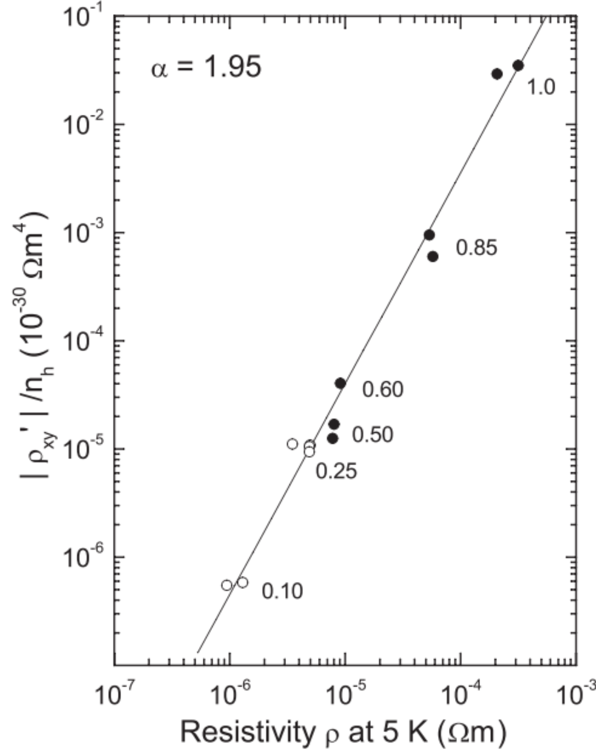

Figure 3.21: Scaling plots of normalized anomalous Hall resistivity $|\rho_{xy}/n_{\mathrm{h}}|$ against resistivity ρ in the ferromagnetic spinel semiconductor $\mathrm{CuCr_2Se_{4-x}Br_x}$ measured at 5 K. A scaling relation of $|\rho_{xy}/n_{\mathrm{h}}| = A\rho^{\alpha}$, where $\alpha = 1.95 \pm 0.08$ and $A = 2.24{\times}10^{-25}$, is observed. The figure is originally from Ref. [118].

σ_{SH}/n as a function of μ (here the mobility of majority carrier is used, i.e., μ_{e} for x=0.17, 0.47 and μ_{h} for x=0.65) is illustrated in Fig. 3.22. The spin current mobility increases with increasing μ for all x studied here. The slope of σ_{SH}/n versus μ tends to increase positively with increasing the Sb concentration. For the Bi-rich BiSb alloys, σ_{SH}/n is nearly independent of μ, suggesting that the extrinsic skew scattering contribution is negligible. In contrast, σ_{SH}/n slightly increases with μ for Sb-rich BiSb alloys, indicating that it may contain contribution from skew scattering. As shown in the schematic of the band structure of Bi-rich $\mathrm{Bi_{1-x}Sb_x}$ alloy in Fig. 3.23, the transport property is dominated by the massive Dirac electrons in the L valley [86,96,110,120,121]. By substituting Sb for Bi, holes from the T and H valleys with quadratic-like dispersion become more important on the conduction, which has been confirmed by the x dependence of R_{H} presented in Fig. 3.12(a). The Dirac-like property of electrons in the L valley also gradually reduces with increasing the

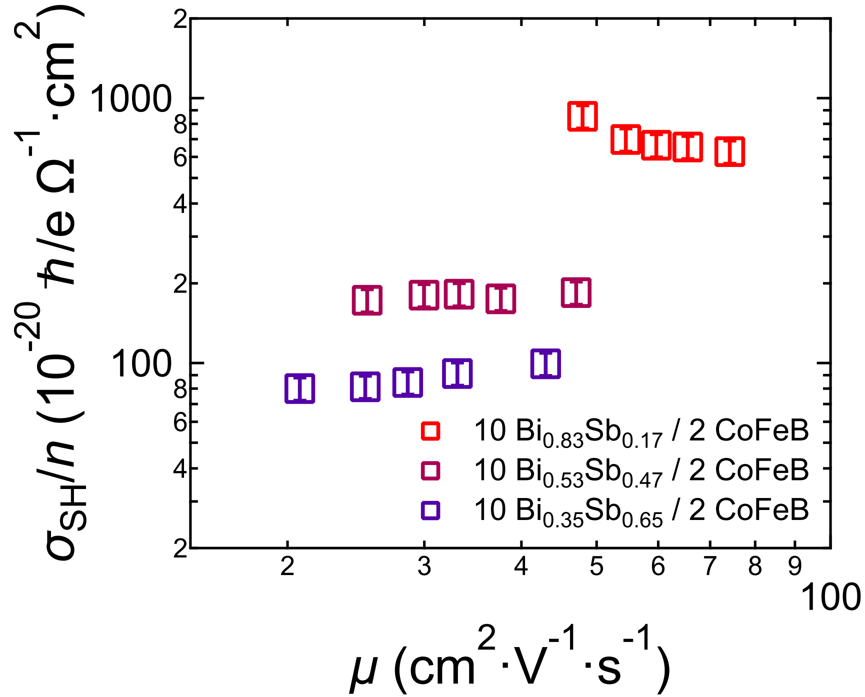

Figure 3.22: σ_{SH}/n as a function of the mobility of majority (μ_e for $x = 0.17$ and 0.47; μ_h for $x = 0.65$) for 10 $\mathrm{Bi}_{1-x}\mathrm{Sb}_x$/2 CoFeB thin film heterostructures.

substitution. Therefore, our spin current mobility analysis suggests that the massive Dirac-like electrons in the L valley, rather than the holes in the T or H valley with quadratic dispersion, play a key role in obtaining the large intrinsic SHE in $\mathrm{Bi}_{1-x}\mathrm{Sb}_x$. This picture can explain the large enhancement of σ_{SH} and ξ_{DL} with increasing temperature: thermal broadening of the Fermi-Dirac distribution introduces more massive Dirac electrons at higher temperature. A direct comparison of the density of massive Dirac electrons between high and low temperature is schematically shown in Fig. 3.23.

To provide quantitative comparison of the spin current mobility with other materials, we estimate the σ_{SH}/n of a typical HM, Pt, which has the highest theoretical intrinsic SHC ($\sigma_{\mathrm{SH}} \approx 2000$ $(\hbar/e)\Omega^{-1}\cdot\mathrm{cm}^{-1}$ at 0 K [122]). σ_{SH}/n of Pt is $\sim 20 \times 10^{-20}$ $(\hbar/e)\Omega^{-1}\cdot\mathrm{cm}^2$ with the assumption that n of Pt is $\sim 10^{22}$ cm^{-3}. This value is more than one order of magnitude smaller than that of $\mathrm{Bi}_{0.83}\mathrm{Sb}_{0.17}$ evaluated at room temperature ($\sigma_{\mathrm{SH}}/n \sim 800{\times}10^{-20}$ $(\hbar/e)\Omega^{-1}\cdot\mathrm{cm}^2$). In addition, Fig. 3.22 shows that σ_{SH}/n in Bi-rich alloy ($\mathrm{Bi}_{0.83}\mathrm{Sb}_{0.17}$) is nearly one order of magnitude larger than that of Sb-rich one ($\mathrm{Bi}_{0.35}\mathrm{Sb}_{0.65}$). These results reveal the higher spin current generation efficiency and mobility of the

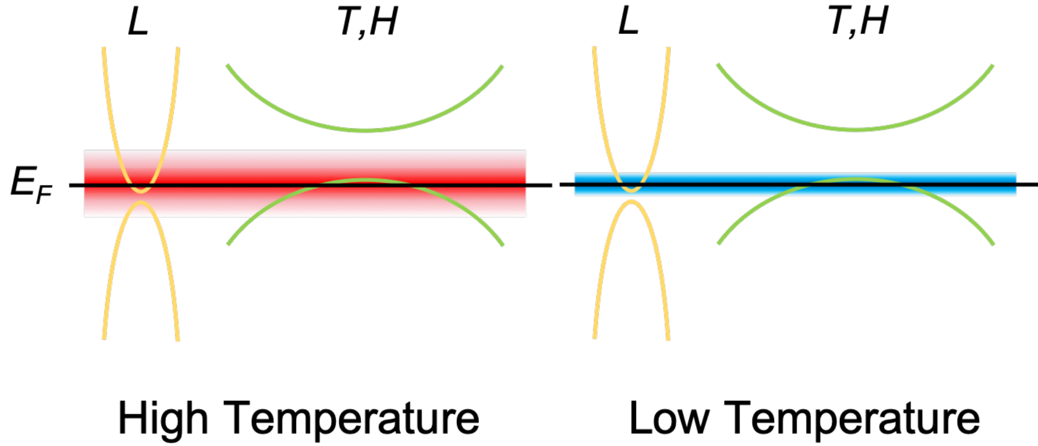

Figure 3.23: Schematic illustration of the band structures, focusing around L and T (or H) valleys, of the Bi-rich Bi-Sb alloy with different thermal broadening at high (left) and low (right) temperature.

L-valley massive Dirac electrons in Bi-rich BiSb alloys compared to the holes in Sb-rich BiSb and the s-like conduction electrons in Pt.

3.6 Conclusion

We have characterized current-induced SOT in polycrystalline $Bi_{1-x}Sb_x$ alloy/CoFeB heterostructures to study current-spin conversion efficiency (ξ_{DL}) of $Bi_{1-x}Sb_x$ alloy. The BiSb thickness dependence of SHC in $Bi_{0.53}Sb_{0.47}$ thin films is in accordance with the spin diffusion model, indicating that current-spin conversion take place in the bulk of BiSb alloy. $\xi_{DL} \sim 1.2$ is found in $Bi_{0.83}Sb_{0.17}$ at room temperature. The SHC of $Bi_{1-x}Sb_x$ exhibits a plateau with a value of ~ 600 $(\hbar/e)$ $\Omega^{-1}\cdot\text{cm}^{-1}$ for $x < 0.35$ and decreases gradually with increasing x. This trend is in good agreement with the calculation based on a tight-binding model, suggesting the intrinsic contribution from the band structure is likely to dominate the SHE in $Bi_{1-x}Sb_x$. The SHC is robust against the facet orientation of $Bi_{1-x}Sb_x$ thin film, indicating that the TSS, if present, plays little role in current-spin conversion. An unexpected enhancement of SHC with increasing temperature is observed in $Bi_{1-x}Sb_x$. By spin current mobility analysis, we infer that such enhancement is due to the thermally-

excited massive Dirac electrons in the L valley.

Chapter 4

Current-spin conversion in carrier-doped Bi thin films

4.1 Introduction

In the previous chapter, we have demonstrated large current-spin conversion efficiency in BiSb alloy generated by the intrinsic spin Hall effect (SHE). Based on our observation of the increase in spin Hall conductivity (SHC) with increasing temperature in BiSb alloy, we assume that the strong SHE of BiSb alloy is related to the thermally-excited massive Dirac electrons presided at the L valley. However, solid experimental or theoretical evidence is still necessary to confirm this assumption. Because the Dirac-like character of the carriers in BiSb alloy originates from Bi, a good strategy to address this issue is to investigate the Fermi-level dependence of the current-spin conversion efficiency in Bi. Considering the simplified band structure of Bi with L and T valleys, as illustrated in Fig. 4.1, the Fermi level (E_F) in pristine Bi can be tuned by carrier doping. If the massive Dirac carriers contribute to the SHE, the SHC of Bi should depend on the position of Fermi level.

In this chapter, we present studies on current-spin conversion in carrier-doped Bi thin films. Te (valance electron configuration as $5p^4$) and Sn (valance electron configuration as $5p^2$) are doped to pristine Bi as electron and hole dopants, respectively, to tune the Fermi level. Previous studies have shown the effectiveness of carrier doping by substituting Te and Sn for $Bi_{0.9}Sb_{0.1}$ [123]. Here, we use current-induced SOT in doped Bi/CoFeB heterostructures to study the current-spin conversion efficiency.

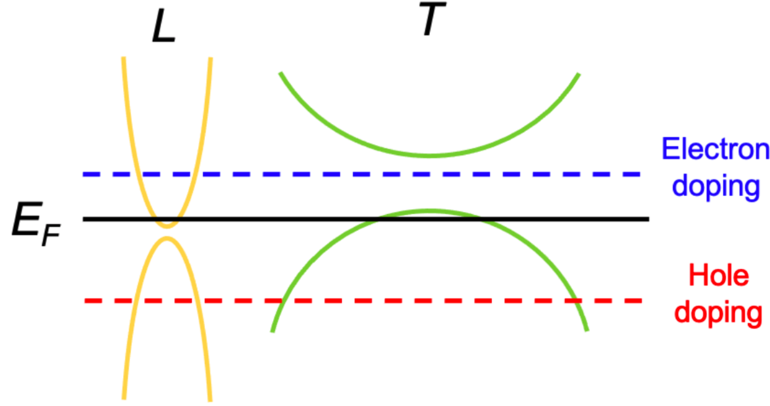

Figure 4.1: Schematic illustration of Bi band structure and Fermi level shift via carrier doping.

4.2 Sample description

Te-doped Bi ($Bi_{1-x}Te_x$) and Sn-doped Bi ($Bi_{1-y}Sn_y$) alloy thin films were grown by magnetron sputtering using the alternating ultrathin layer deposition (AULD) method on 10×10 mm^2 Si substrate at ambient temperature. x and y represent the nominal doping concentration of Te and Sn in Bi, respectively. The base structures are Sub./0.5 Ta/[$t_{\rm Bi}$ Bi|$t_{\rm Sn}$ Sn]$_{N=16}$/0.3 Bi/$t_{\rm CoFeB}$ CoFeB/2 MgO/1 Ta and Sub./0.5 Ta/[$t_{\rm Bi}$ Bi|$t_{\rm Te}$ Te]$_{N=16}$/0.3 Bi/$t_{\rm CoFeB}$ CoFeB/2 MgO/1 Ta (thickness in units of nanometer, nm). $t_{\rm Bi(Te,\ Sn)}$ is the thickness of each Bi (Te, Sn) layer. $N = 16$ represents the repeat number of Bi|Sn and Bi|Te bilayers. The thickness of the bilayer is set to satisfy $t_{\rm Bi}+t_{\rm Te(Sn)} \sim 0.63$ nm and the total thickness of the multilayer (including the Bi termination layer) is $\sim$ 10.4 nm. The Te (Sn) concentration is defined as $x(y) \equiv t_{\rm Te(Sn)}/(t_{\rm Bi} + t_{\rm Te(Sn)})$. $t_{\rm CoFeB}$ is the thickness of the CoFeB layer. We refer to films with $t_{\rm CoFeB} = 0$ as $Bi_{1-x}Te_x$ and $Bi_{1-y}Sn_y$ thin films and $t_{\rm CoFeB}$ =2 nm as $Bi_{1-x}Te_x$/CoFeB and $Bi_{1-y}Sn_y$/CoFeB heterostructures. The nominal composition of CoFeB is Co:Fe:B = 20:60:20 in atomic %. The bottom 0.5 Ta acts as a seed layer and the 2 MgO/1 Ta capping layer is used to protect the films from oxidation. A 15 nm-thick pristine Bi thin film and 15 Bi/2 CoFeB heterostructure, i.e., Sub./0.5 Ta/15 Bi/$t_{\rm CoFeB}$ CoFeB/2 MgO/1 Ta ($t_{\rm CoFeB} = 0$ or 2), were grown as reference samples (non-doped Bi).

4.3 Structure and magnetization characterization

The bulk binary phase diagram of Bi-Te shows limited solubility of Te in rhombohedral Bi, whereas Bi and Sn are practically immiscible [124]. In thin films, however, non-equilibrium phases with extended solubility may be stabilized. $\theta - 2\theta$ x-ray diffraction (XRD) spectra of pristine and doped Bi thin films with different x and y are shown in Fig. 4.2(a). There is no CoFeB layer in these films. All the films are polycrystalline with predominant Bi (012) and (104) diffraction peaks. These results indicate that there are two primary orientations normal to the film plane for x and y up to 0.4. Focusing on the (012) diffraction, the corresponding interatomic plane distance $d_{(012)}$ deduced from the Bragg's law (Eq. 2.1) is plotted as a function of x and y in Fig. 4.2(b). $d_{(012)}$ changes linearly with x and y, which is in accordance with the Vegard's law. The opposite slope of $d_{(012)}$ against x and y for $Bi_{1-x}Te_x$ and $Bi_{1-y}Sn_y$ is attributed to the different atomic radii r of Bi, Te and Sn, with a relation: $r_{Te} \leq r_{Bi} < r_{Sn}$ [125]. The appearance of β-Sn (200) peak for $y \geq 0.3$ may indicate agglomeration of β-Sn clusters in Bi.

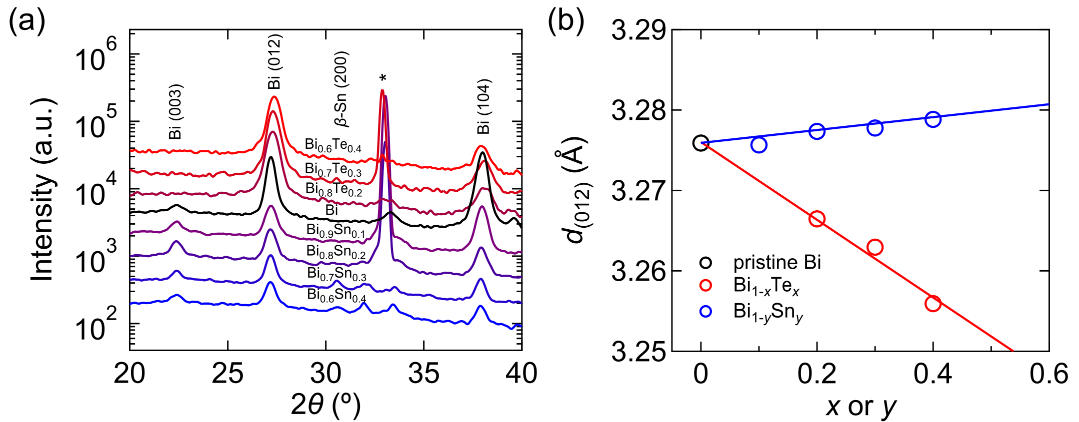

Figure 4.2: (a) XRD spectra of pristine, Te- and Sn-doped Bi thin films grown on substrates with 0.5 nm Ta seed layers. (b) Doping concentration (x for Te and y for Sn) dependence of Bi (012) interatomic plane distance, $d_{(012)}$ deduced from Bragg's law. The nominal thickness of all the thin films are 10.4 nm.

The magnetic properties of carrier-doped Bi/CoFeB heterostructures were investigated using a vibrating sample magnetometer (VSM) at room temper-

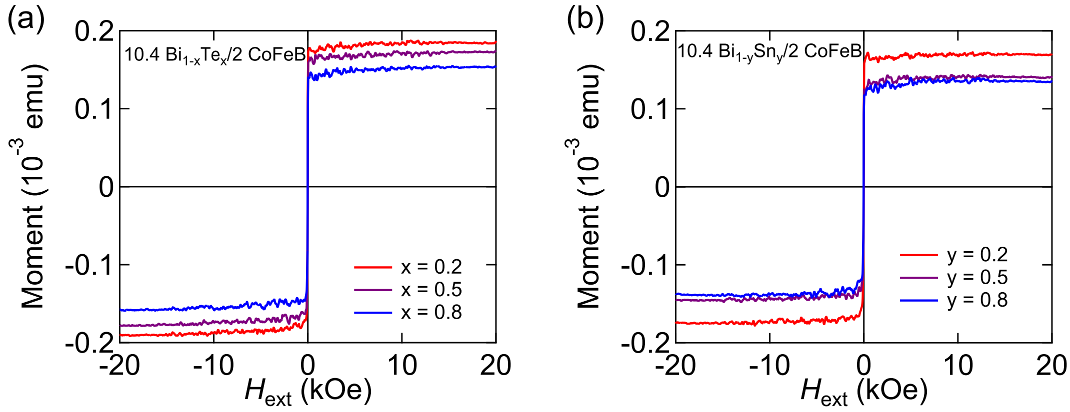

Figure 4.3: The magnetization hysteresis loops for 10.4 $Bi_{1-x}Te_x$/2 CoFeB (a) and 10.4 $Bi_{1-y}Sn_y$/2 CoFeB (b) heterostructures with different doping level x and y. The data is obtained under an external field applied along the film plane at room temperature.

ature. The magnetization hysteresis loops of 10.4 $Bi_{1-x}Te_x$/2 CoFeB and 10.4 $Bi_{1-y}Sn_y$/2 CoFeB heterostructures with different x and y ($x, y = 0.2$, 0.5 and 0.8) are shown in Figs. 4.3(a) and (b), respectively. The magnetization hysteresis loops are measured with an external magnetic field $H_{\rm ext}$ applied along the film plane. The saturated magnetic moment $M_{\rm sat}$ is defined as

$$M_{\rm sat} = M_{\rm s} \cdot t_{\rm eff} = M_{\rm s} \left(t_{\rm CoFeB} - t_{\rm DL} \right), \tag{4.1}$$

where $M_{\rm s}$ is the saturation magnetization and $t_{\rm eff}$ is the magnetic effective thickness of the CoFeB layer. We find that the saturated magnetic moment decreases with increasing x and y. We assume the $M_{\rm s}$ of CoFeB is equal to $1190\,{\rm emu}\cdot{\rm cm}^{-3}$ (the value deduced in Chap. 3), independent of the choice of the underlayer, and use this value to estimate the magnetic dead layer thickness $t_{\rm DL}$. The x and y dependences of $t_{\rm DL}$ in doped Bi/CoFeB heterostructures are presented in Fig. 4.4. $t_{\rm DL}$ increases with increasing x or y. A linear function is used to fit $t_{\rm DL}$ against x and y with a fixed interpolation for $x = y = 0$. The values of $t_{\rm DL}$ in $Bi_{1-x}Te_x$/CoFeB and $Bi_{1-y}Sn_y$/CoFeB heterostructures with different x and y are estimated according to this fitting.

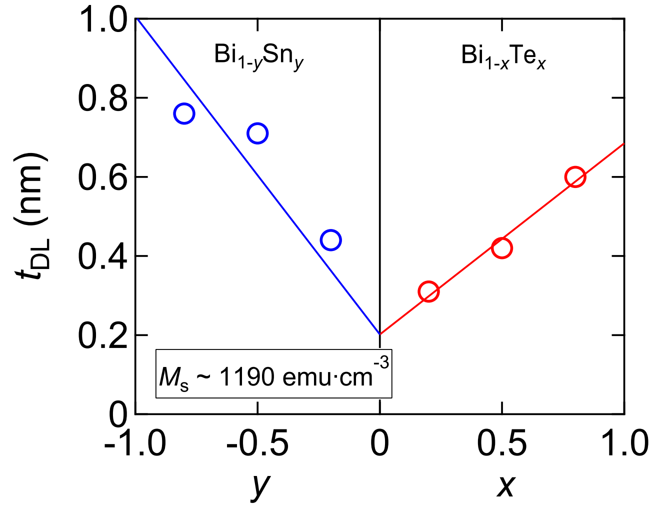

Figure 4.4: x and y dependence of the estimated dead layer thickness (t_{DL}) of 10.4 $Bi_{1-x}Te_x$/2 CoFeB (a) and 10.4 $Bi_{1-y}Sn_y$/2 CoFeB (b) heterostructures. The magnetization M_s is controlled as 1190 emu·cm^{-3}. The red and blue lines are the linear fitting for t_{DL} against x and y, respectively, with a fixed interpolation for $x = y = 0$.

4.4 Direct current transport measurement

First, we study the DC current transport properties of pristine Bi, $Bi_{1-x}Te_x$, and $Bi_{1-y}Sn_y$ thin films at room temperature using micro-sized Hall bar devices. The same device is used both for transport and spin-orbit torque (SOT) measurement (see Fig. 3.6(a)). The longitudinal resistivity ρ_{xx} of pristine and doped Bi thin films is plotted as a function of x or y in Fig. 4.5. ρ_{xx} exhibits a sharp peak and decreases monotonically with increasing x and y. We attribute this trend to the enhanced carrier concentrations via chemical doping, as shown below.

The Hall resistance R_{xy} of $Bi_{1-x}Te_x$ and $Bi_{1-y}Sn_y$ thin films with different x and y are plotted as a function of an out-of-plane external magnetic field (H_z) in Figs. 4.6(a) and (b), respectively. The sign of the slope of R_{xy} in $Bi_{1-x}Te_x$ is opposite of that of $Bi_{1-y}Sn_y$, confirming that the majority carrier changes from electron to hole by varying the dopant from Te to Sn. The concentration, n, and mobility, μ, of carriers in doped Bi is estimated based on the single-carrier model. For pristine Bi, both carriers contribute to the transport due to the electron and hole pockets at the L and T valleys. Thus,

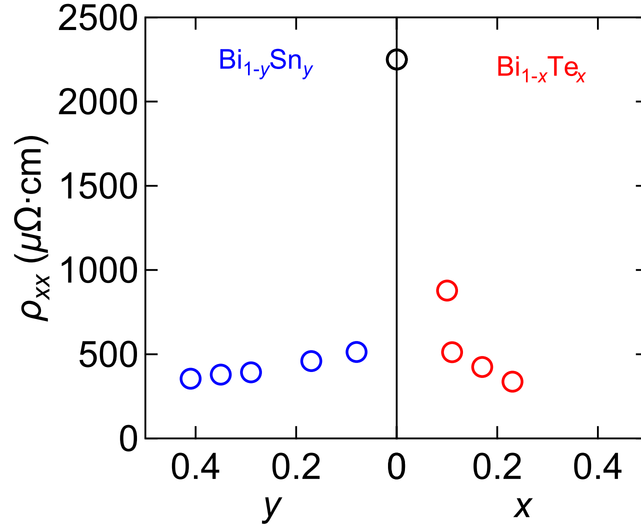

Figure 4.5: x and y dependence of resistivity ρ_{xx} in pristine and carrier-doped Bi thin films. The black hollow circles is the value for 15 nm pristine Bi thin film. The thickness of all the doped Bi thin films is fixed as 10.4 nm. All the data were acquired at 300 K.

we adopt the two-carrier model, which has been introduced in Chap. 3, to estimate the carrier concentration and mobility in pristine Bi using the results of additional magnetoresistance measurements.

Figure 4.6(c) shows n as a function of x and y. Positive (negative) n corresponds to the majority carrier being electron (hole). The concentration of majority carrier (electron) in pristine Bi ($\sim 3.8 \times 10^{19}\,\mathrm{cm}^{-3}$) is one or two orders of magnitude smaller than that of doped Bi. These results are in accordance with the simple rigid-band illustration shown in Fig. 4.1: starting from pristine Bi, electron and hole doping shift E_{F} away from the Dirac point, leading to a dramatic enhancement of $|n|$. Assuming that Te or Sn substitutes Bi and provides one carrier, the black line in Fig. 4.6(c) the calculated n versus x or y, which is in reasonable agreement with experimental data. The difference in n with Te and Sn doping may be attributed to the different solubility of the two elements in Bi and/or the influence of the heavier hole bands at the T valley. Hereafter, we choose n as an indicator of the Fermi level positioning relative to the Dirac point. The x and y dependence of μ for the majority carrier, i.e., electrons for pristine Bi and $\mathrm{Bi}_{1-x}\mathrm{Te}_x$ and holes for $\mathrm{Bi}_{1-y}\mathrm{Sn}_y$, is presented in Fig. 4.6(d). μ decays rapidly with increasing doping. Within the

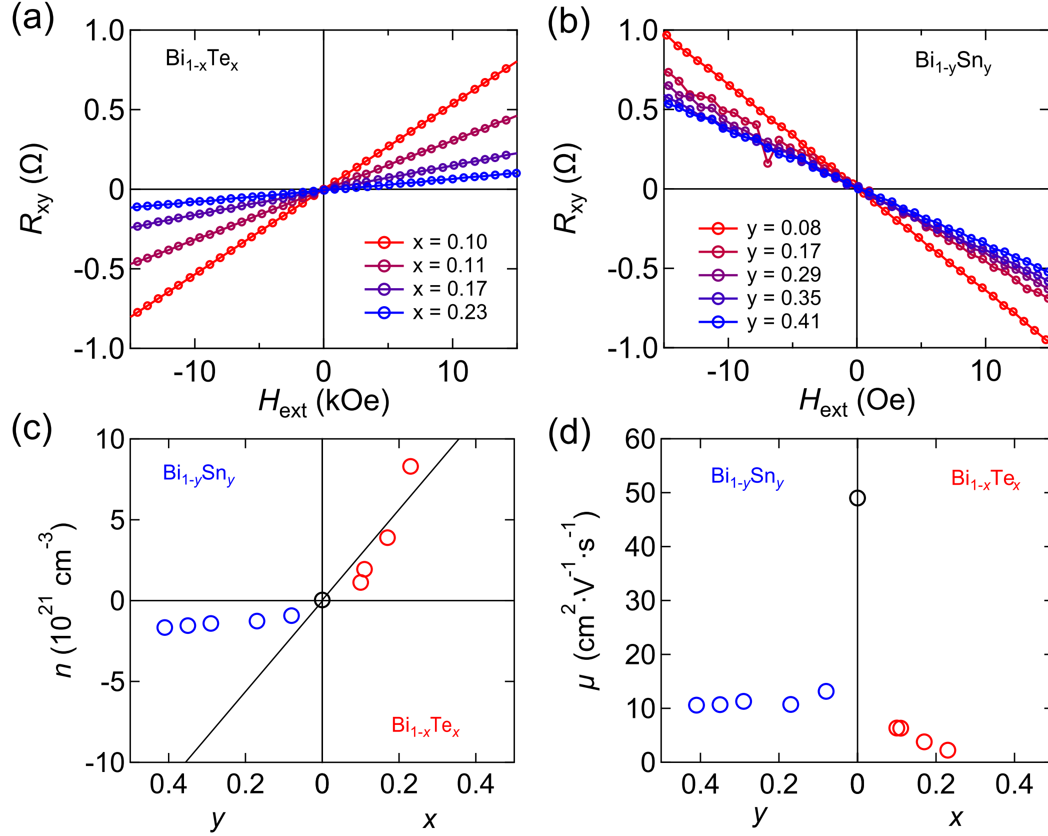

Figure 4.6: (a,b) Hall resistance R_{xy} of $Bi_{1-x}Te_x$ (a) and $Bi_{1-y}Sn_y$ (b) thin films ($t_{CoFeB} = 0$) with different x and y as a function of external field (H_{ext}). (c,d) x and y dependence of carrier concentration n (c) and the mobility μ for majority carrier (d) in pristine and carrier-doped Bi thin films. The signal of n of hole is defined as negative. The thickness of all the doped Bi thin films is fixed as 10.4 nm. The black hollow circles in (c) and (d) are the values for 15 nm pristine Bi thin film. The line in (c) represents the calculated results based on the assumption that each Te or Sn atom provides one carrier. All the data were acquired at 300 K.

Drude model, μ is proportional to τ/m^*, where τ and m^* are the relaxation time and effective mass of carriers, respectively. Thus, the decrease of μ upon doping can be attributed to two reasons. First, the scattering of carriers increases with increasing doping, contributing to the decrease of τ. Second, E_F is shifted away from the Dirac point by increasing x or y, resulting in the loss of Dirac-like character of carriers, i.e., the increase of m^*. Given the significant change of μ, we infer the latter is more likely to be dominant.

4.5 Current-spin conversion characterization

The current-induced SOT in 15 Bi/2 CoFeB, 10.4 $Bi_{1-x}Te_x$/2 CoFeB and 10.4 $Bi_{1-y}Sn_y$/2 CoFeB heterostructures were quantified using the harmonic Hall resistance technique. The amplitude of applied AC current was set in the range of 1~4.5 mA_{rms} and the frequency ($\omega/2\pi$) was set as 17.5 Hz. Typical first harmonic Hall resistance R_ω of a 10.4 $Bi_{0.89}Te_{0.11}$/2 CoFeB heterostructure measured under different H_{ext} is plotted against φ in Fig. 4.7(a). We use Eq. 2.28 to fit the data and obtain the planar Hall resistance R_{PHE}. R_{PHE} changes little upon varying H_{ext}, suggesting negligible sample misalignment and weak external field dependence of R_{PHE}. Therefore, we treat R_{PHE} as the average value obtained under different magnetic fields. Fig. 4.7(b) illustrates R_{PHE} for 15 Bi/2 CoFeB, 10.4 $Bi_{1-x}Te_x$/2 CoFeB and 10.4 $Bi_{1-y}Sn_y$/2 CoFeB plotted as a function of n. The magnitude of R_{PHE} decreases with increasing n. We consider this trend is mainly due to the enhanced current shunting in the doped Bi layer.

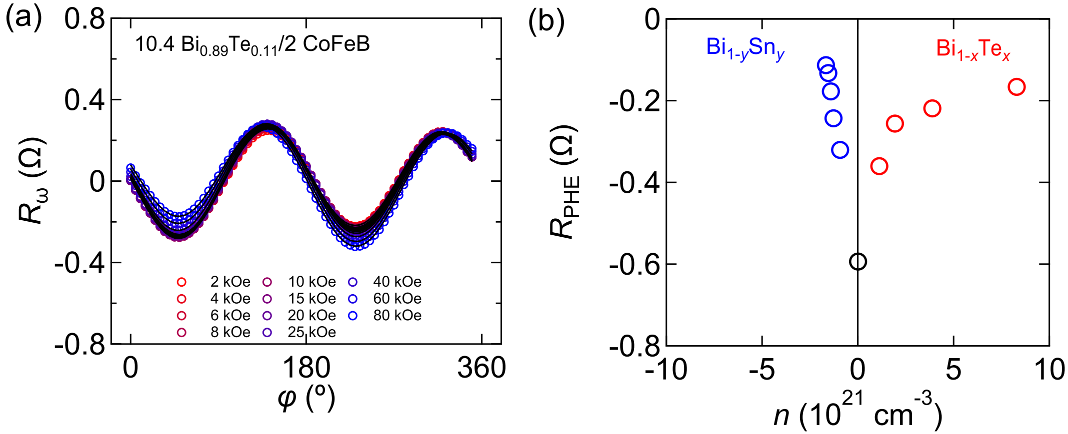

Figure 4.7: (a) Representative azimuthal angle, φ, dependence of first harmonic Hall resistance (R_ω) of 10.4 $Bi_{0.89}Te_{0.11}$/2 CoFeB heterostructure measured at different external fields H_{ext}. The black curves are the fitting results according to Eq. 2.28 (b) Planar Hall resistance (R_{PHE}) of different doped Bi/CoFeB heterostructures plotted as a function of carrier concentration n.

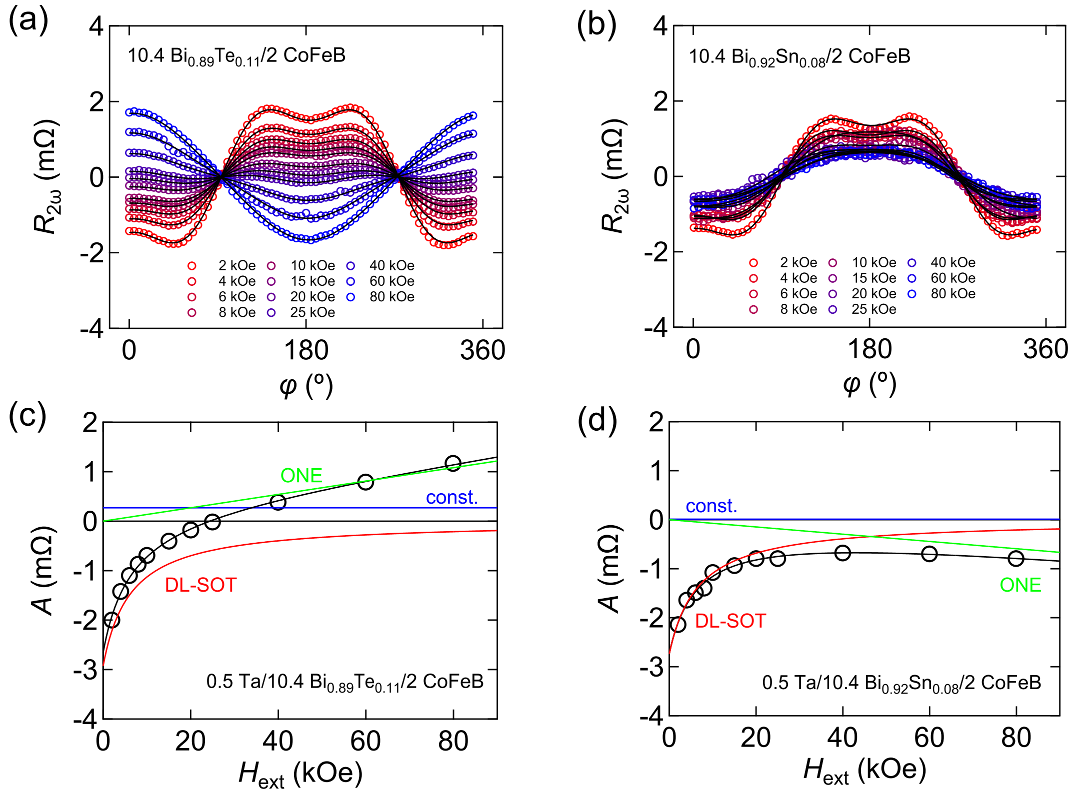

Figure 4.8: (a,b) Representative azimuthal angle, φ, dependence of second harmonic Hall resistance ($R_{2\omega}$) of 10.4 $Bi_{0.89}Te_{0.11}$/2 CoFeB (a) and 10.4 $Bi_{0.92}Sn_{0.08}$/2 CoFeB heterostructures measured at different external fields H_{ext}. The black curves are the fitting results according to Eq. 2.27 (c,d) H_{ext} dependence of the magnetitude of $\cos\varphi$ part, A, in $R_{2\omega}$. The colored lines are the contributions from different origins and the black lines are the summation of all the contributions.

Representative φ-dependent $R_{2\omega}$ for 10.4 $Bi_{0.89}Te_{0.11}$/2 CoFeB and 10.4 $Bi_{0.92}Te_{0.08}$/2 CoFeB heterostructures measured at different H_{ext} are plotted in Figs. 4.8(a) and (b), respectively. Black solid lines are the best fits using Eq. 2.27. First, we focus on A of $R_{2\omega}$, i.e., the prefactor of $\cos\varphi$ component in $R_{2\omega}$, to extract the effective field H_{DL} associated with the damping-like spin-orbit torque (DL-SOT). The H_{ext} dependence of A for 10.4 $Bi_{0.89}Te_{0.11}$/2 CoFeB and 10.4 $Bi_{0.92}Sn_{0.08}$/2 CoFeB heterostructures are plotted using black hollow circles in Figs. 4.8(c) and (d), respectively. The black lines show the best fits using Eq. 2.27. Other colored lines represent decompositions of various

contributions. For both samples, contributions induced by the DL-SOT (red lines) are dominant in small H_{ext}, whereas contributions from the ordinary Nernst effect (ONE) (green lines) become more important at larger fields. The sign of the latter contribution in $Bi_{1-x}Te_x$/CoFeB is opposite of that of $Bi_{1-y}Sn_y$/CoFeB heterostructures, which can be related to the change of the majority carriers in these two series of doped Bi thin films. In contrast, the SOT maintains its sign upon changing the carrier type, which is in agreement with theoretical predictions [86–88].

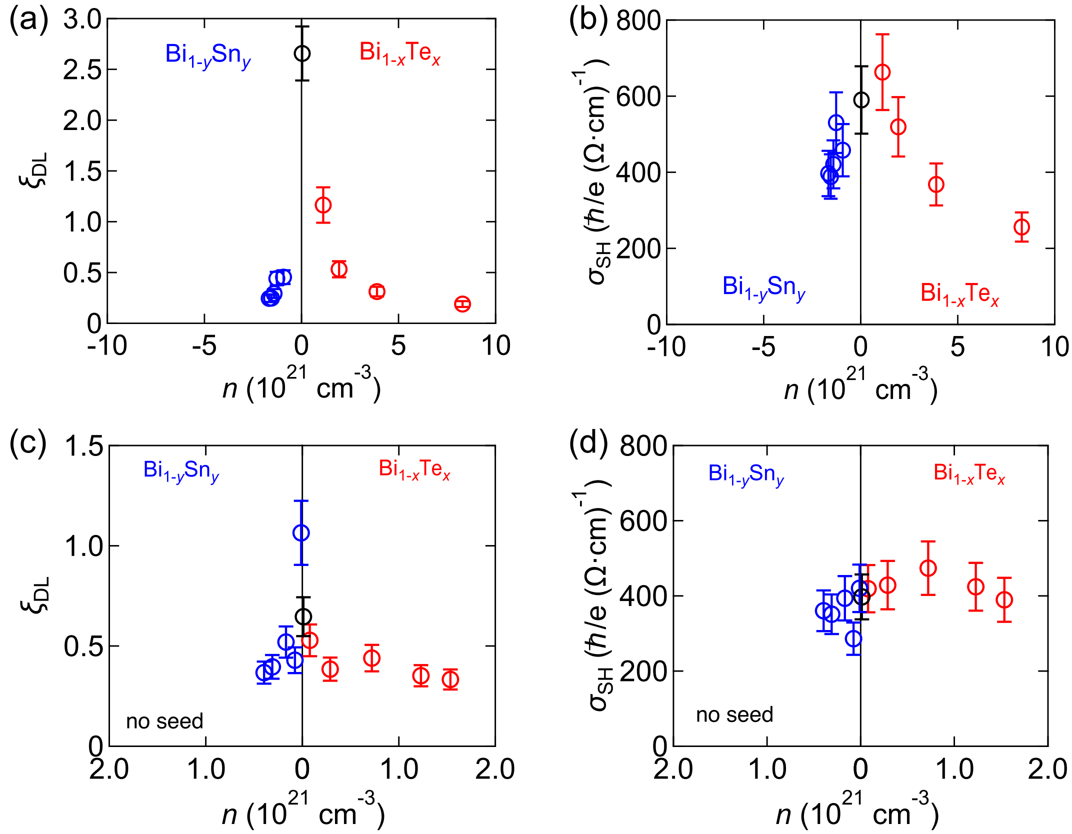

Figure 4.9: (a,b) Carrier concentration n dependence of the efficiency of DL-SOT ξ_{DL} (a) and spin Hall conductivity σ_{SH} (b) in 15 Bi/2 CoFeB, 10.4 $Bi_{1-x}Te_x$/2 CoFeB and 10.4 $Bi_{1-y}Sn_y$/2 CoFeB heterostructures. (c,d) n dependence of ξ_{DL} (c) and σ_{SH} (d) in 11 Bi/2 CoFeB, 11 $Bi_{1-x}Te_x$/2 CoFeB and 11 $Bi_{1-y}Sn_y$/2 CoFeB heterostructures without Ta seed layers. All the data were obtained at 300 K.

The efficiency of DL-SOT ξ_{DL} can be obtained by substituting H_{DL}, the current density in doped Bi layer j_{Bi}, anomalous Hall resistance R_{AHE}, out-of-

plane anisotropy field H_k, M_s and t_eff into Eq. 2.38. j_Bi is calculated using a parallel circuit resistor model with an assumption of $\rho_{xx,\mathrm{CoFeB}} \sim 150\,\mu\Omega\cdot\mathrm{cm}$ [104]. R_AHE and H_k are acquired in separate anomalous Hall effect (AHE) measurements. M_s and t_eff are determined by the VSM measurement. ξ_DL of pristine Bi, $\mathrm{Bi}_{1-x}\mathrm{Te}_x$ and $\mathrm{Bi}_{1-y}\mathrm{Sn}_y$ are plotted as a function of n in Fig. 4.9(a). ξ_DL is positive (same as that of Pt [107] and BiSb alloy shown in the previous chapter) for both types of doping. ξ_DL decreases rapidly and monotonically with increasing n. For highly resistive pristine Bi, we obtain $\xi_\mathrm{DL} \sim 2.7$, which is comparable to the prototype $\mathrm{Bi_2Se_3}$ topological insulator (TI) [74]. This is one of the largest values of ξ_DL reported for Bi [89–92]. We note there is an important difference between our samples and those in previous studies: the stacking order of the heterostructures is different. In our samples, CoFeB is deposited on Bi whereas the stacking is opposite in past studies [89–92]. We have also prepared a 3 CoFeB/11 Bi heterostructure and found ξ_DL ~0.09, which is comparable to the values in previous reports but much smaller than that of Bi/CoFeB heterostructure. We infer that such difference originates from the change in the Bi near the CoFeB interface. Although the exact origin remains to be identified, these results suggest the stacking significantly influence the measurement of current-spin conversion of Bi.

As shown in Fig. 4.9(b), the SHC (σ_SH, given by Eq. 2.39) shows a weak n dependence in the low-doping regime ($n < 2\times10^{21}\,\mathrm{cm}^{-3}$ or $x, y < 0.1$) with $\sigma_\mathrm{SH} \sim 600$ $(\hbar/e)$ $\Omega^{-1}\cdot\mathrm{cm}^{-1}$ before dramatically decreasing for higher doping and larger $|n|$. In order to investigate the SHC in the low-doping regime, lightly doped Bi/CoFeB heterostructures with $|n| \leq 2\times10^{21}\,\mathrm{cm}^{-3}$ are made and studied. The lightly doped Bi thin films are grown using the AULD method, however, with an increased Bi layer thickness ($\sim 2\,\mathrm{nm}$) to form the [Bi|Te (Sn)] bilayers. Pristine Bi thin film is also grown together. Note that there is a break in the deposition for every 2-nm-thick Bi deposition. In addition, there is no Ta seed layer in light-doped Bi thin films.

Figures.4.9(c) and (d) illustrate the carrier concentration dependence of ξ_DL and σ_SH in light-doped Bi. ξ_DL decreases with increasing n whereas σ_SH is nearly independent of n. The value of σ_SH in such plateau is slightly smaller than that shown in Fig.4.9 (b) with $n \sim 0$. We assume the discrepancy is due to the difference in the growth procedure. We assume n represents the position of E_F relative to the Dirac point in Bi. The trend of σ_SH in Bi against the Fermi level positioning is consistent with theoretical results [86, 88]. Interestingly, the value of SHC is in quantitative agreement with the tight-binding model calculation [88]. These results suggest the intrinsic SHE, not the TSS, is the origin of current-spin conversion in pristine Bi. The Fermi level dependence of σ_SH in Bi agrees with the AHE of a ferromagnetic kagome metal with massive

Dirac fermions: the Berry curvature is concentrated in the vicinity of the Dirac gap [126]. In our case, as E_F shifts away from the Dirac point with increasing n- or p-type doping, the carriers progressively lose their Dirac-like character and current-spin conversion decreases. This trend also explains why doping Bi with Sb, which roughly maintains the same valence band filling and E_F positioning to Bi, can sustain a robust σ_{SH} plateau against wider doping level, up to $Bi_{0.65}Sb_{0.35}$. We note that the decay of σ_{SH} against n for both electron and hole doping is nearly symmetric across $n \sim 0$, which suggests the carriers in heavy T-hole valley has negligible contribution to σ_{SH}.

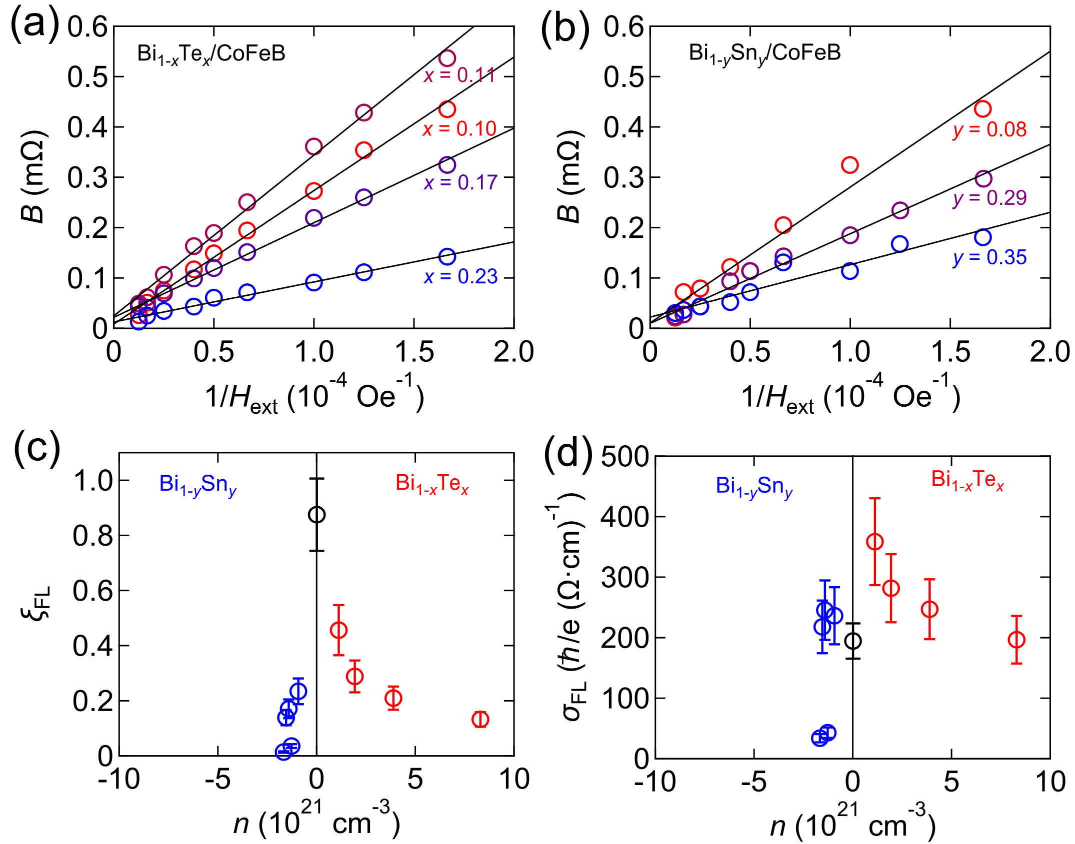

Figure 4.10: (a,b) $1/H_{ext}$ dependence of the magnitude of $\cos 2\varphi \cos \varphi$ part, B, in $R_{2\omega}$ for 10.4 $Bi_{1-x}Te_x$/2 CoFeB (a) and 10.4 $Bi_{1-y}Sn_y$/2 CoFeB (b) heterostructures with different x and y. The black lines are the linear fitting results. (c,d) Carrier concentration n dependence of the efficiency of FL-SOT ξ_{FL} (c) and field-like spin Hall conductivity (FL-SHC) σ_{FL} (d). All the data were measured at 300 K.

The efficiency of field-like spin-orbit torque (FL-SOT) ξ_{FL} of pristine and Te (Sn)-doped Bi/CoFeB heterostructures are estimated by extracting the sum of FL-SOT effective field and Oersted field, $H_{\mathrm{FL}}+H_{\mathrm{Oe}}$, from the H_{ext} dependence of B, i.e., the prefactor of $\cos 2\varphi \cos\varphi$ component in $R_{2\omega}$. $1/H_{\mathrm{ext}}$ dependences of B for $\mathrm{Bi}_{1-x}\mathrm{Te}_x$/CoFeB and $\mathrm{Bi}_{1-y}\mathrm{Sn}_y$/CoFeB heterostructures with different x and y are illustrated in Figs. 4.10(a) and (b), respectively. The solid lines show linear fits. The slope of these fitted lines is proportional to $H_{\mathrm{FL}}+H_{\mathrm{Oe}}$ according to Eq. 2.30. H_{Oe} can be estimated using the Ampère's law (see Chap. 2). The sign of H_{Oe} is opposite of that of H_{FL}. H_{Oe} is subtracted from $H_{\mathrm{FL}}+H_{\mathrm{Oe}}$ to obtain H_{FL}. ξ_{FL} and the corresponding field-like spin Hall conductivity (FL-SHC) σ_{FL} are then obtained using Eqs. 2.38 and 2.39.

ξ_{FL} of pristine and Te (Sn)-doped Bi/CoFeB heterostructures are plotted as a function of n in Fig. 4.10(c). We find the sign of ξ_{FL} is positive in all samples. This sign agrees with Pt/Co/AlO_x [39] and BiSb/CoFeB, whereas it is opposite of that of $\mathrm{Bi_2Se_3}$/Py [74]. ξ_{FL} exhibits a maximum near $n \sim 0$ and decreases with increasing n. For a given n, the magnitude of ξ_{FL} is almost half of that of ξ_{DL}. Fig. 4.10(d) shows the carrier concentration dependence of σ_{FL}. We find σ_{FL} shares similar n dependence with that of σ_{SH} except for an abrupt drop for $|n| > 1.5 \times 10^{21}\,\mathrm{cm}^{-3}$ in the regime of hole doping. The origin of the n dependence of ξ_{FL} and σ_{FL} is unclear.Further studies are required to understand the physics behind.

4.6 Discussion

4.6.1 Robustness of SHC in Bi

To illustrate the robustness of SHE in Bi that originates from the Dirac point, we have also investigated the current-induced SOT in pristine Bi/CoFeB heterostructures with Bi layers grown under different conditions. Four 15 nm-thick pristine Bi thin films, including the one which has been studied above, were grown with different combinations of sputtering conditions (including Ar gas pressure and sputtering power) and seed layers. These samples are referred to as S1 to S4. The growth conditions of the four pristine Bi thin films have been summarized in Table 4.1.

Fig. 4.11(a) shows the XRD spectra of the four pristine Bi thin films. Although both Bi (003) and (012) diffraction peaks are observed in the spectra, the ratio of the two peaks changes in all samples, indicating that the facet orientation of the Bi thin films is tunable by the growth condition. After depositing a 2 nm-thick CoFeB layer onto the Bi thin films, the magnetic properties of the samples were investigated using a VSM. The magnetization

hysteresis loops in Bi/CoFeB heterostructures measured under an H_{ext} applied along the film plane are presented in Fig. 4.11(b). Little difference in the saturated magnetic moment is observed, suggesting negligible influence of the Bi structure on M_{s} and t_{DL} in pristine Bi/CoFeB heterostructures.

Table 4.1: Growth condition and the seed layer of the four Bi thin films

Sample	Condition	Seed layer
S1	20 W, 0.5 Pa	n/a
S2	20 W, 0.5 Pa	0.5 nm Ta
S3	12 W, 1.0 Pa	n/a
S4	12 W, 1.0 Pa	0.5 nm Ta

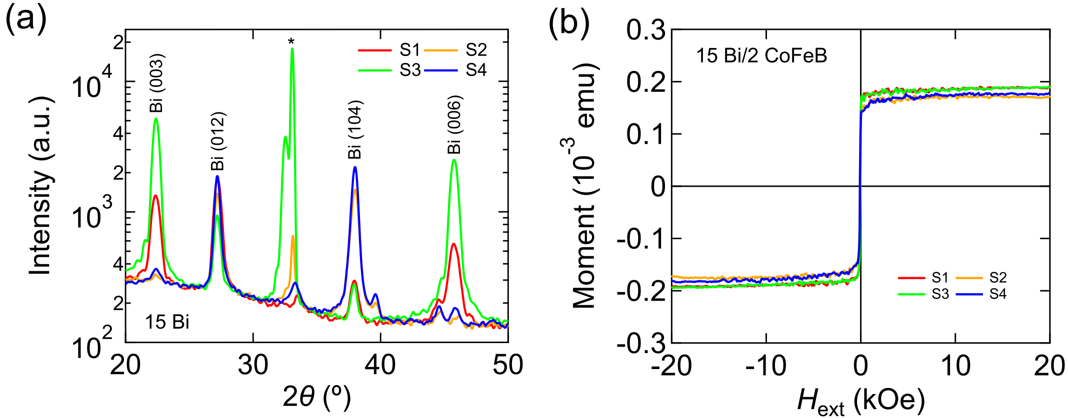

Figure 4.11: (a) XRD spectra of the pristine 15 Bi thin films grown with different combinations of sputtering conditions and seed layers. (b) The magnetization hysteresis loops of different 15 Bi/2 CoFeB heterostructures. The loops were measured at a field along sample plane. All the data were acquired at 300 K.

The mobility of electron (μ_{e}) and hole (μ_{h}), carrier concentration, and resistivity for S1 to S4 are summarized in Table. 4.2. The two-carrier model is used to determine the value of n, μ_{e} and μ_{h} using additional magnetoresistance measurements. ρ_{xx} increases dramatically by inserting a 0.5 nm-thick Ta seed layer; the difference is nearly a factor of five for the samples with and without the seed layer. n has the same order of magnitude in all films. However, the majority carrier of film can be electron or hole depending on the sputtering

Table 4.2: Resistivity ρ_{xx}, carrier concentration n, mobility of electron μ_e and hole μ_h, the efficiency of DL-SOT ξ_{DL}, and spin Hall conductivity σ_{SH} in S1 to S4.

Sample	ρ_{xx}	n	μ_e	μ_h	ξ_{DL}	σ_{SH}
	$\mu\Omega \cdot$ cm	10^{19} cm^{-3}	cm^{2}V^{-1}s^{-1}	cm^{2}V^{-1}s^{-1}		$(\hbar/e)$ $\Omega^{-1}\cdot$cm^{-1}
S1	970	3.2	108	120	1.21	622
S2	3060	1.0	101	94	3.70	604
S3	665	2.6	178	204	0.64	478
S4	2250	3.8	49	39	2.66	590

condition. We assume that the large change in ρ_{xx} is due to the difference in the density of impurities of the films controlled. ξ_{DL} and SHC of the four pristine Bi/CoFeB heterostructures are summarized in Table. 4.2. Unlike the notable changes of the transport properties, σ_{SH} is almost constant for the four Bi thin films; the mean value is $\sim 574 \pm 65(\hbar/e)\Omega^{-1} \cdot \mathrm{cm}^{-1}$.The dominant facet orientation of the Bi thin films hardly changes the SHC. We note that the SHC of BiSb alloy is saturated at a thickness of $\sim 8\,\mathrm{nm}$. Considering the same intrinsic origin of SHE in Bi and BiSb alloy, we assume the value of SHC is also saturated in the samples we have studied here.

4.6.2 Current-spin conversion in Te-rich $Bi_{1-x}Te_x$ thin films

Bi_2Te_3 ($x = 0.6$) is a typical TI where the Dirac cone of TSS forms at the Γ point [65]. To understand whether the TSS of Bi_2Te_3 may contribute to the large ξ_{DL} and σ_{SH} in our samples, we have also investigated the transport and current-spin conversion properties ofs $Bi_{1-x}Te_x$ thin films with $0.5 < x < 0.8$. $\theta - 2\theta$ XRD spectra of 10.4 $Bi_{1-x}Te_x$ thin films for $x = 0.5 - 0.8$ are shown in Fig. 4.12(a). Unlike the XRD spectra of the $Bi_{1-x}Te_x$ thin films with $x \leq 0.4$, Bragg diffraction peaks corresponding to Bi_2Te_3 (006) and (0015) are found. Bi(012) and (104) diffraction peaks gradually disappear with increasing x and a weak Te (100) peak appears for $Bi_{0.2}Te_{0.8}$. These results indicate the formation of polycrystalline Bi_2Te_3 for $x \geq 0.5$. The ρ_{xx} of $Bi_{1-x}Te_x$ thin films for $0 < x < 1$ is shown in Fig. 4.12(b). ρ_{xx} increases dramatically with increasing Te concentration for $x > 0.4$, which we interpret as a manifestation of the phase transition from semimetallic Bi to semiconducting Bi_2Te_3.

The estimated ξ_{DL} and σ_{SH} in $Bi_{1-x}Te_x$ are plotted as a function of x in Fig. 4.12(c). For $x > 0.4$, ξ_{DL} is considerably smaller than that of Bi-rich

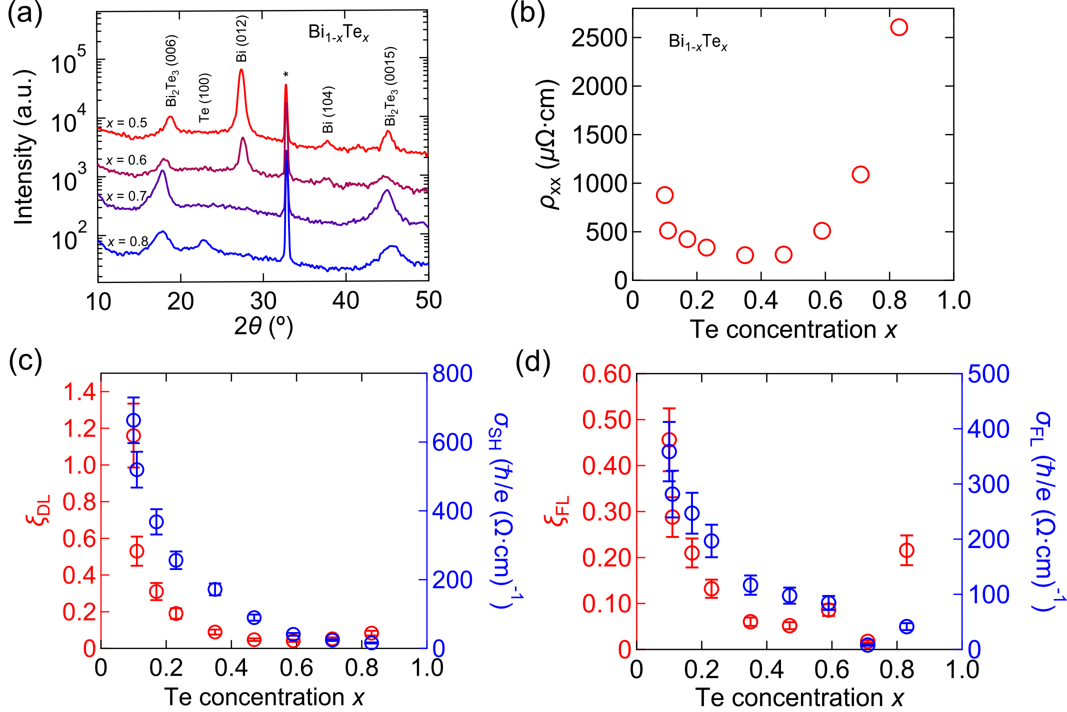

Figure 4.12: (a) XRD spectra of 10.4 $Bi_{1-x}Te_x$ thin films with $x \geq 0.5$. (b) x dependence of resistivity ρ_{xx} of $Bi_{1-x}Te_x$ thin films for $0 < x < 1$. (c,d) x dependence of ξ_{DL} with corresponding σ_{SH} (c) and ξ_{FL} with corresponding σ_{FL} (d) in 10.4 $Bi_{1-x}Te_x$/2 CoFeB heterostructures with $0 < x < 1$. All the measurements were conducted at 300 K.

$Bi_{1-x}Te_x$ ($x < 0.25$) and increases slightly with increasing x for $x > 0.6$. The enhancement of ξ_{DL} for $x > 0.6$ is attributed to the significant increase of the resistivity. σ_{SH} of $Bi_{1-x}Te_x$ with $x > 0.6$ decreases monotonically with increasing x and is one order of magnitude ($\sim$40 $(\hbar/e)$ Ω^{-1}·cm^{-1}) smaller than that of Bi-rich thin films. This value is consistent with that of bulk Bi_2Te_3 reported in previous studies [127]. We thus find no evidence that $Bi_{1-x}Te_x$ thin films with Bi_2Te_3 phase can enhance σ_{SH}. ξ_{FL} and σ_{FL} of $Bi_{1-x}Te_x$ are presented in Fig. 4.12(d) as a function of x. ξ_{FL} (σ_{FL}) increases (decreases) with increasing x for $x > 0.6$. However, there is a sudden drop in the magnitude of σ_{FL} at $x \sim 0.7$, where the crystallization of Bi_2Te_3 takes place. Further studies are required to confirm whether such a drop of FL-SOT is related to the phase

transition from Bi to Bi_2Te_3.

4.7 Conclusion

In this work, we have investigated current-spin conversion in carrier-doped Bi thin films. Te and Sn are doped to Bi as electron and hole dopants, respectively, to tune the Fermi level. We show that the SHC of Bi is significantly dependent on the position of Fermi level relative to the Dirac point, suggesting that massive Dirac carriers play a critical role in controlling current-spin conversion in Bi. The SHC of Bi shows little dependence on the facet orientation and resistivity. We exclude the TSS contribution on the large current-spin conversion. These results thus demonstrate the robust current-spin conversion process of massive Dirac carriers.

Chapter 5

Structure, magnetic anisotropy and current-spin conversion in $Pt_{1-x}Bi_x$/Co/MgO trilayers

5.1 Introduction

Obtaining large perpendicular magnetic anisotropy (PMA) in magnetic devices is critical to developing modern storage devices. Although we have demonstrated spin Hall effect (SHE)-induced current-spin conversion in BiSb and Bi, with an efficiency significantly larger than that of heavy metal (HM), the ferromagnetic metal (FM) layers used in our studies show in-plane magnetic anisotropy (IMA). Technologically, it is important to find a system exhibiting large current-spin conversion efficiency and PMA. Peng *et al*. have predicted that MgO/CoFe/Bi structure gives rise to large PMA using first-principle calculations [128]. It has also been proposed that topological insulator (TI)/HM/FM/oxide heterostructures can be used to set PMA in such structure by making use of the PMA at the HM/FM interface [79, 127]. This approach can also be applied to Bi-based materials. However, introducing an adjacent HM layer with strong SHE will prevent the spin current from Bi to the FM layers. Alternating ultrathin layer deposition (AULD) method has been confirmed as an efficient means to form a Bi-based alloy with controllable concentration. The question is whether one can exploit the AULD method to develop systems that possess large current-spin conversion efficiency and PMA.

In this chapter, we show studies on the magnetic transport characteristics of $Pt_{1-x}Bi_x$/Co/MgO trilayers deposited by the AULD method. Pt/Co/MgO trilayer is chosen as the prototype due to its strong interface PMA [100–102, 129, 130]. We investigate the influence of Bi doping on the structure, magnetic property, and current-spin conversion efficiency in $Pt_{1-x}Bi_x$ at room tempera-

ture.

5.2 Sample description

$Pt_{1-x}Bi_x$/Co/MgO trilayers were grown by radio frequency (RF) magnetron sputtering at room temperature. The base structure is Sub./3 Ta/2 Pt/[t_{Bi} Bi|t_{Pt} Pt]$_{N=8}$/t_{Co} Co/2 MgO/1 Ta (unit in nanometer, nm), where $Pt_{1-x}Bi_x$/Co/MgO layers were grown using the AULD method. $t_{Pt\ (Bi)}$ is the thickness of Pt (Bi) ultrathin film in the Bi|Pt bilayer. $t_{Bi} + t_{Pt}$ is set to satisfy ~ 0.9 nm. $N = 8$ represents the repeat number of the Bi|Pt bilayer. t_{Co} is the thickness of Co layer, which is set to 0.6 or 1.5 nm. 3 Ta/2 Pt and 2 MgO/1 Ta are the seed and capping layers, respectively. We assume the 2 nm-thick Pt layer in the seed layer also contributes to the alloying of $Pt_{1-x}Bi_x$. Therefore, Bi doping level x is defined as $x \equiv \frac{t_{Bi}\times 8}{(t_{Pt}+t_{Bi})\times 8+2}$ and the total thickness of the $Pt_{1-x}Bi_x$ layer t_{PtBi} is 9.2 nm.

5.3 Structural characterization

The binary phase diagram of Pt-Bi shows that the alloy experience three phase transitions by increasing x: Pt to PtBi, PtBi to $PtBi_2$, and $PtBi_2$ to Bi [124]. $\theta - 2\theta$ x-ray diffraction (XRD) spectra of 9.2 $Pt_{1-x}Bi_x$ thin films and a reference 3 Ta/2 Pt seed layer sample are shown in Fig. 5.1(a). The Pt (111) diffraction peak is observed in $Pt_{1-x}Bi_x$ thin films for $x \leq 0.51$ and the reference sample. The intensity of Pt (111) peak is much sharper in $Pt_{1-x}Bi_x$ thin films which is thicker than reference sample. The corresponding interatomic distance of Pt (111) planes, $d_{(111)}$ deduced from the Bragg's law (Eq. 2.1) is plotted as a function of x in Fig. 5.1(b). $d_{(111)}$ can be fitted linearly against x, as expected from the Vegard's law. The increasing $d_{(111)}$ with x can be understood by the larger covalent radii of Bi than that of Pt [125]. These results indicate $Pt_{1-x}Bi_x$ thin film forms a Pt-Bi solid solution.

For a 9.2 $Pt_{0.38}Bi_{0.62}$ thin film, $PtBi_2$ $(00n)$ diffraction peaks are observed (the space group of $PtBi_2$ is $P\bar{3}$). In this sample, the Pt (111) peak shifts toward the $PtBi_2$ (003) peak, suggesting that $Pt_{1-x}Bi_x$ thin film forms a Pt-$PtBi_2$ mixture. $PtBi_2$ has been predicted as a three-dimensional Dirac semimetal [131]. The Dirac band in the bulk and the surface state have been confirmed using angle-resolved photoemission spectroscopy (ARPES) [132].

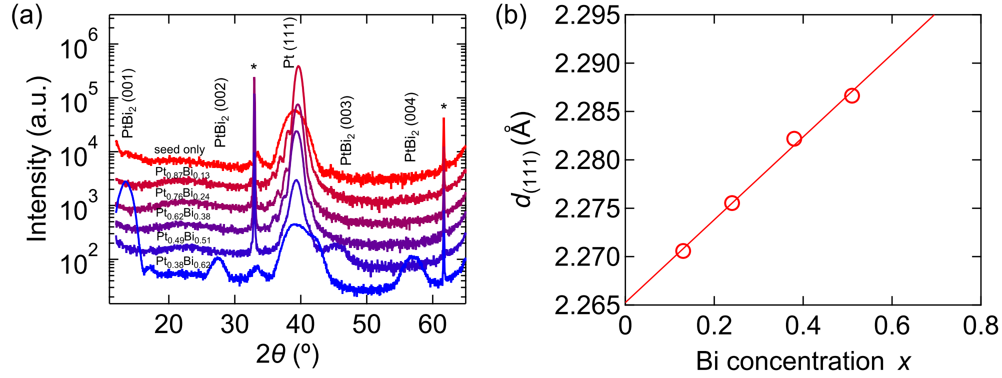

Figure 5.1: (a) XRD spectra of $Pt_{1-x}Bi_x$ alloy thin films with different Bi doping level x and a seed layer reference sample. The nominal thickness of all the $Pt_{1-x}Bi_x$ alloy thin film samples is 9.2 nm. (b) x dependence of Pt (111) interatomic plane distance $d_{(111)}$ for $Pt_{1-x}Bi_x$ thin films with $x \leq 0.51$.

5.4 Magnetic properties

The magnetic properties of 9.2 $Pt_{1-x}Bi_x/t_{Co}$ Co/MgO trilayers with $t_{Co} = 0.6$ nm are investigated using a vibrating sample magnetometer (VSM) at room temperature. It has been known that Pt/Co/oxide trilayers with an ultrathin Co layer exhibit PMA [133, 134].

The magnetization hysteresis loops of 9.2 $Pt_{1-x}Bi_x$/0.6 Co/MgO trilayers are presented in Fig. 5.2. The loops measured under H_{ext} applied along and perpendicular to the film plane are represented in blue and red lines, respectively. For Pt-rich films ($x \leq 0.51$), the magnetic easy axis of the Co layer points along the film normal. The easy axis of ultrathin Co film in the 9.2 $Pt_{0.38}Bi_{0.62}$/0.6 Co/MgO trilayer, where $Pt_{1-x}Bi_x$ thin film is a Pt-$PtBi_2$ mixture, lies in the film plane. We cannot exclude the possibility that the easy axis of the Co layer points along the film normal by further decreasing t_{Co} because the effective magnetic anisotropy energy, i.e., the integrated areal difference between the easy-axis and hard-axis magnetization hysteresis loops, is relatively small. Nevertheless, these results imply the PMA is weakened by the structural change in Bi-rich $Pt_{1-x}Bi_x$ thin films [129, 130].

The PMA of 9.2 $Pt_{1-x}Bi_x$/0.6 Co/MgO trilayers with more x values is studied using the anomalous Hall effect (AHE) measurement after micro-fabricating

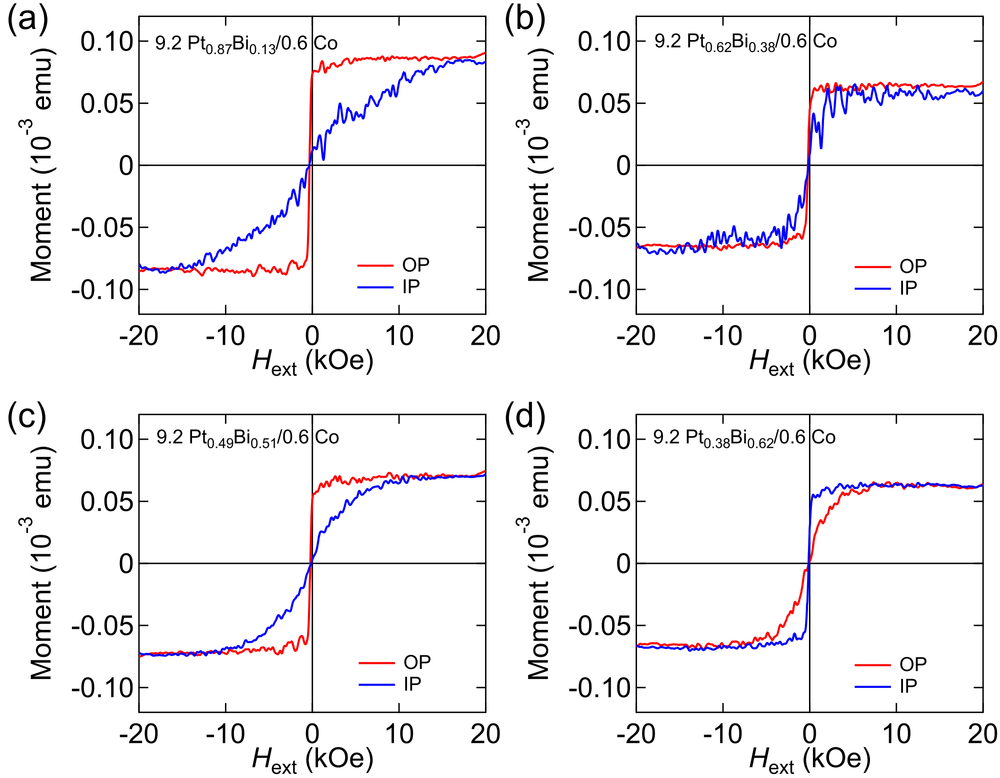

Figure 5.2: Magnetization hysteresis loops for 9.2 $Pt_{1-x}Bi_x$/0.6 Co/MgO trilayers with different x under H_{ext} applied normal to (OP) or along (IP) the film plane.

the samples into Hall bar devices. Optical image of a representative Hall bar device and the coordinate system are shown in Fig. 5.3(a). Fig. 5.3(b) illustrates the normalized Hall resistance R_{xy} hysteresis loops for 9.2 $Pt_{1-x}Bi_x$/0.6 Co/MgO trilayers with different x. The loops are measured under an external magnetic field along the z-axis (H_z). It is found that the easy axis of the Co layer changes from out-of-plane to in-plane when x is 0.56 $\sim$ 0.60, which is consistent with the results obtained by the VSM measurements.

5.5 Current-spin conversion characterization

Current-spin conversion in $Pt_{1-x}Bi_x$ is first studied using 9.2 $Pt_{1-x}Bi_x$/1.5 Co heterostructures, where the easy axis of 1.5 nm-thick Co thin film lies in the

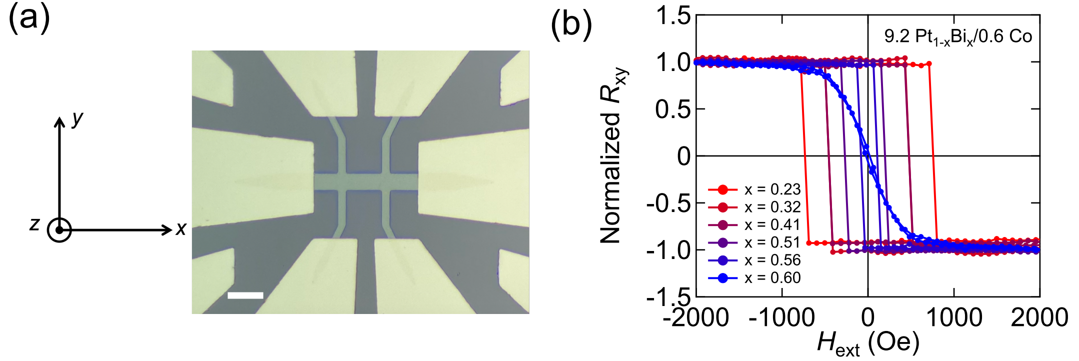

Figure 5.3: (a) Optical image of the micro-fabricated Hall bar device and the coordinate system defined in the transport measurement. The scale bar represents 20 μm. (b) Normalized Hall resistance R_{xy} hysteresis loops for 9.2 $Pt_{1-x}Bi_x$/0.6 Co/MgO trilayers with different x. The loops were obtained under an external field applied perpendicular to the film plane H_z.

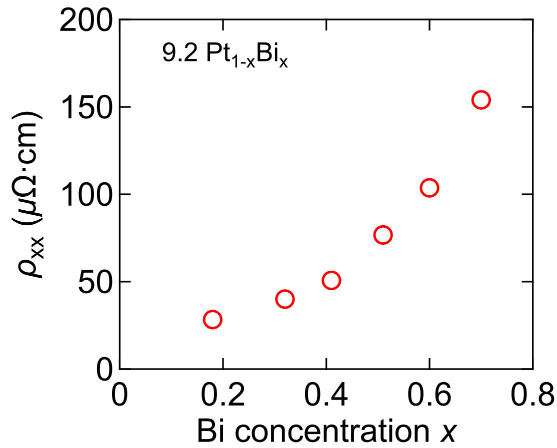

Figure 5.4: Bi doping level x dependence of resistivity ρ_{xx} of 9.2 $Pt_{1-x}Bi_x$ thin films.

film plane. The current-induced spin-orbit torque (SOT) in 9.2 $Pt_{1-x}Bi_x$/1.5 Co heterostructures is characterized using the harmonic Hall resistance technique. The amplitude and frequency ($\omega/2\pi$) of the applied AC current in the measurements were 3 mA_{rms} and 17.5 Hz, respectively. Bi concentration de-

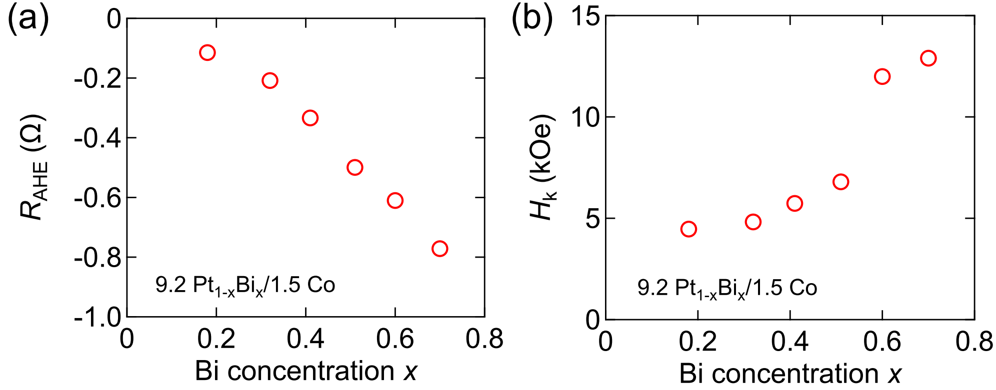

Figure 5.5: Bi doping level x dependence anomalous Hall resistance R_{AHE} (a) and out-of-plane anisotropy field H_k (b) of 9.2 $\mathrm{Pt}_{1-x}\mathrm{Bi}_x$/1.5 Co heterostructures.

pendence of the resistivity of the $\mathrm{Pt}_{1-x}\mathrm{Bi}_x$ layer (ρ_{xx}) is shown in Fig. 5.4. ρ_{xx} of a $\mathrm{Pt}_{0.82}\mathrm{Bi}_{0.18}$ thin film possesses a value of $28.4\,\mu\mathrm{m}\cdot\mathrm{cm}$, comparable to that of pure Pt thin film [135]. ρ_{xx} increases with increasing Bi doping. For $x \geq 0.60$, the resistivity is close to that reported in PtBi_2 single crystal [136]. Typically, the resistivity of materials increases in sputtered sample because of the enhanced scattering from the higher density of impurity. Thus, we suggest that the phase segregation of Pt and PtBi_2 occurs and Pt considerably contributes to conduction in this regime. R_{AHE} and the out-of-plane anisotropy H_k for 9.2 $\mathrm{Pt}_{1-x}\mathrm{Bi}_x$/1.5 Co heterostructures are determined by the AHE measurements. The values of R_{AHE} and H_k are plotted as a function of x in Figs. 5.5(a) and (b), respectively. $|R_{\mathrm{AHE}}|$ increases monotonically with increasing x, which is attributed to the reduction of current shunting into the PtBi layer. H_k increases with increasing x; while there is an abrupt jump for $x \geq 0.6$, which is likely to be related to the phase transition in the $\mathrm{Pt}_{1-x}\mathrm{Bi}_x$ layer.

The harmonic Hall resistance of 9.2 $\mathrm{Pt}_{1-x}\mathrm{Bi}_x$/1.5 Co heterostructures was measured under H_{ext} with different strength (from 1 to 80 kOe) applied along the film plane. The angle between H_{ext} and the x-axis is defined as φ. Representative φ dependence of the first harmonic Hall resistance R_ω for a 9.2 $\mathrm{Pt}_{0.30}\mathrm{Bi}_{0.70}$/1.5 Co heterostructure is presented in Fig. 5.6(a). The φ-dependent R_ω is hardly influenced by the strength of H_{ext} and can be fitted using Eq. 2.28. From the fitting parameter, we obtain planar Hall resistance R_{PHE}, which is plotted as a function of x in Fig. 5.6(b). $|R_{\mathrm{PHE}}|$ increases with increasing x for $x \leq 0.6$. This trend is attributed to the reduced current shunting into the $\mathrm{Pt}_{1-x}\mathrm{Bi}_x$ layer with increasing x $|R_{\mathrm{PHE}}|$ slightly decreases for $x \sim 0.6$. We

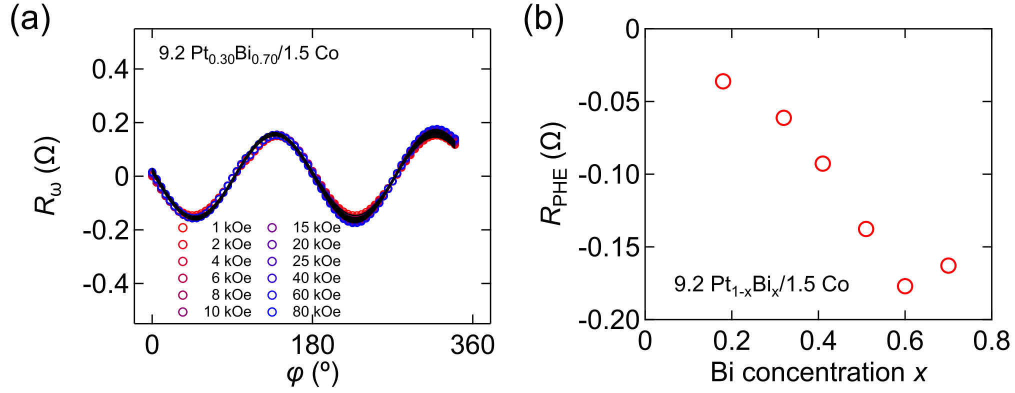

Figure 5.6: (a) Representative azimuthal angle φ dependence of R_ω signals for 9.2 $Pt_{0.40}Bi_{0.60}$/1.5 Co heterostructure measured under different external magnetic field H_{ext} applied along the film plane. (b) Planar Hall resistance R_{PHE} for 9.2 $Pt_{1-x}Bi_x$/1.5 Co heterostructures as a function of Bi doping level x.

infer that such a decrease is associated with the phase transition (formation of $PtBi_2$).

Figures 5.7(a) and (b) show representative φ dependence of the second harmonic Hall resistance $R_{2\omega}$ for 9.2 $Pt_{0.82}Bi_{0.18}$/1.5 Co and 9.2 $Pt_{0.40}Bi_{0.60}$/1.5 Co heterostructures, respectively. The black lines are the best fitting results using Eq. 2.27. Unlike the results of BiSb alloy/CoFeB and carrier-doped Bi/CoFeB heterostructures, the sign of A, which is the prefactor of $\cos\varphi$ component in $R_{2\omega}$, does not change in the high field regime, indicating that contribution from the ordinary Nernst effect (ONE) on $R_{2\omega}$ is small. Thus, we simplify Eq. 2.29 by removing the ONE contribution term, giving

$$A = R_{\text{AHE}} \frac{H_{\text{DL}}}{H_{\text{ext}} + H_k} + \frac{\alpha w \Delta T}{I_0}. \tag{5.1}$$

The A of $R_{2\omega}$ in 9.2 $Pt_{1-x}Bi_x$/1.5 Co heterostructures with different x is plotted as a function of $1/\left(H_{\text{ext}} + H_k\right)$ in Fig. 5.7(c). All the data can be fitted with a linear line. The B of R_ω, which is the amplitude of $\cos 2\varphi \cos\varphi$ component in $R_{2\omega}$, in 9.2 $Pt_{1-x}Bi_x$/1.5 Co heterostructures with different x is plotted as a function of $1/H_{\text{ext}}$ in Fig. 5.7(d). The proportional relationship between B and $1/H_{\text{ext}}$ is illustrated by the linear fitting. The effective fields associated with the damping-like spin-orbit torque (DL-SOT) H_{DL} and the field-like spin-orbit torque (FL-SOT) H_{FL} in 9.2 $Pt_{1-x}Bi_x$/1.5 Co heterostructures are obtained

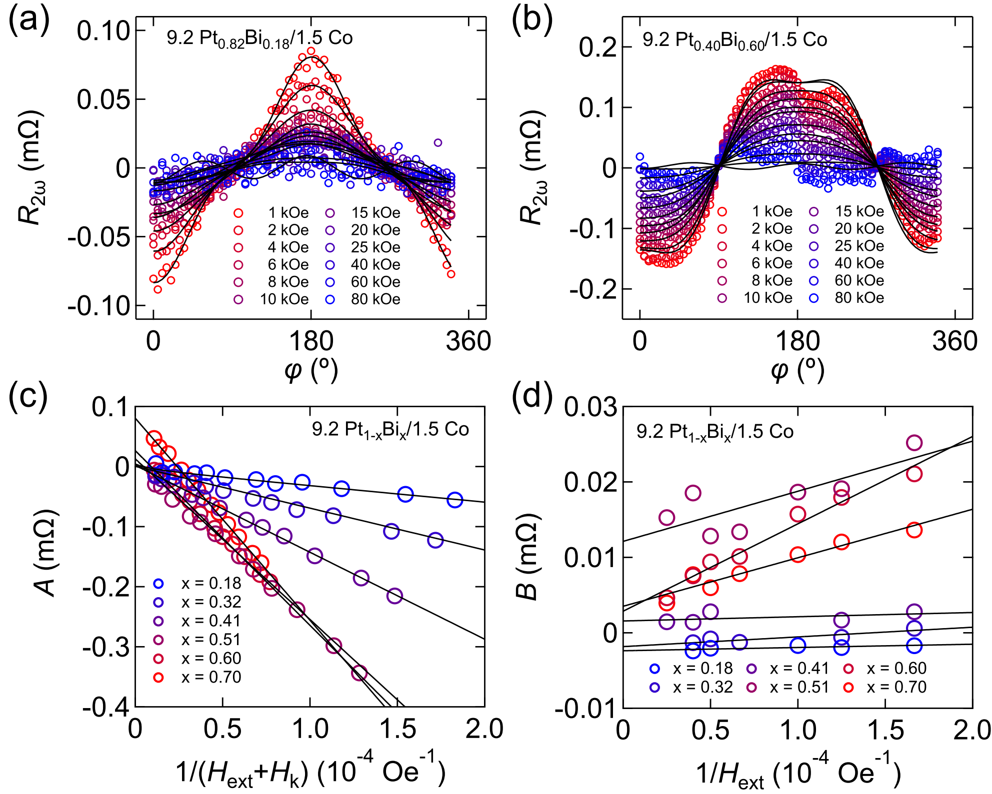

Figure 5.7: (a,b) Representative φ dependence of second harmonic Hall resistance $R_{2\omega}$ for 9.2 $Pt_{0.82}Bi_{0.18}$/1.5 Co (a) and 9.2 $Pt_{0.40}Bi_{0.60}$/1.5 Co (b) heterostructures measured under different external field H_{ext}. The bad fitting in (b) may be due to local asymmetry of devices induced during deposition or fabrication. (c) $1/(H_{\mathrm{ext}} + H_{\mathrm{k}})$ dependence of $\cos\varphi$ part, A, in $R_{2\omega}$ for samples with different x. (d) $\cos 2\varphi \cos\varphi$ part, B, in $R_{2\omega}$ for samples with different x plotted as a function of $1/H_{\mathrm{ext}}$.

from these fitting using Eq. 5.1 and Eq. 2.30. Current-induced Oersted field can be estimated based on the Ampère's law (see Chap. 2). We estimate the efficiency of DL-SOT ξ_{DL} and the efficiency FL-SOT ξ_{FL} by substituting the H_{DL} (or H_{FL}), the current density in $Pt_{1-x}Bi_x$ layers and $M_{\mathrm{s}}{\cdot}t_{\mathrm{eff}}$ (given by the VSM measurement) into Eq. 2.38. The spin Hall conductivity (SHC) σ_{SH} and the field-like spin Hall conductivity (FL-SHC) σ_{FL} are determined using Eq. 2.39.

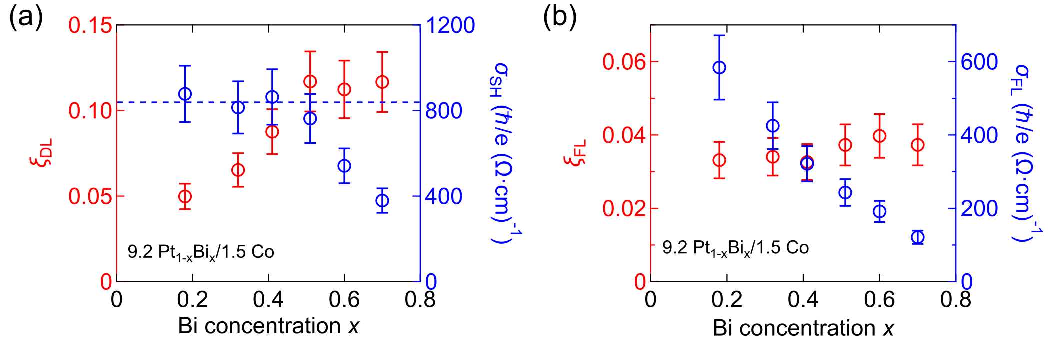

Figure 5.8: Bi doping level x dependence of the efficiency of DL-SOT ξ_{DL} with corresponding spin Hall conductivity σ_{SH} (a) and efficiency of FL-SOT ξ_{FL} with corresponding FL-SHC σ_{FL} (b) of 9.2 $\mathrm{Pt}_{1-x}\mathrm{Bi}_x$/1.5 Co heterostructures. Blue dashed line in (a) represents the average value of σ_{SH} in $\mathrm{Pt}_{1-x}\mathrm{Bi}_x$ for $x \leq 0.51$.

ξ_{DL} and σ_{SH} in $\mathrm{Pt}_{1-x}\mathrm{Bi}_x$ are plotted as a function of x in Fig. 5.8(a). ξ_{DL} increases with increasing x for $x \leq 0.51$ and saturates beyond $x \sim 0.51$. σ_{SH} exhibits a plateau for $x \leq 0.51$ and drops when x is larger than $\sim$0.51. The average value of the SHC in the plateau is ~ 830 $(\hbar/e)$ $\Omega^{-1}\cdot\mathrm{cm}^{-1}$, illustrated by blue dashed line in Fig. 5.8(a). The value and sign of σ_{SH} are similar to those of Pt/NiFe [32, 137] and Pt/Co(Fe) [33, 138] heterostructures. For $x > 0.60$, XRD spectra have shown that the film is a Pt-PtBi_2 mixture. As mentioned above, PtBi_2 has been predicted and confirmed as a three-dimensional Dirac semimetal [131, 132]. Therefore, the topological surface state (TSS), referred to as Fermi arcs in Dirac semimetals [139], exist in PtBi_2. It has been reported that the spin-momentum locking property of Fermi arcs can generate current induced spin accumulation in Weyl semimetal WTe_2 [140] and Dirac semimetal $\mathrm{Cd}_3\mathrm{As}_2$ [141]. We thus infer that the current-spin conversion in $\mathrm{Pt}_{1-x}\mathrm{Bi}_x$ thin films with $x > 0.51$ may include such contribution. Further studies are required to understand the origin of current-spin conversion in $\mathrm{Pt}_{1-x}\mathrm{Bi}_x$ with $x > 0.51$.

ξ_{FL} and σ_{FL} of 9.2 $\mathrm{Pt}_{1-x}\mathrm{Bi}_x$/1.5 Co heterostructures are plotted as a function of x in Fig. 5.8(b). ξ_{FL} hardly depends of x, whereas σ_{FL} decreases monotonically with increasing x. The average value of ξ_{FL} is ~ 0.03, which is consistent with that of Pt/CoFeB heterostructures [104]. ξ_{DL} and ξ_{FL} exhibit different trend against x, suggesting the DL-SOT and the FL-SOT in $\mathrm{Pt}_{1-x}\mathrm{Bi}_x$/Co heterostructures may originate from different sources.

For $x \leq\sim 0.51$, σ_{SH} of $\mathrm{Pt}_{1-x}\mathrm{Bi}_x$ is robust regardless of the change of ρ_{xx} (by a factor of ~ 3) when x is increased from 0.18 to 0.51. These results indicate that the DL-SOT in $\mathrm{Pt}_{1-x}\mathrm{Bi}_x$/Co heterostructures with x smaller than ~ 0.51 is likely attributed to the intrinsic SHE of Pt. Note that Ta in the seed layer possesses a strong SHE, which can generate spin current flowing into $\mathrm{Pt}_{1-x}\mathrm{Bi}_x$/Co bilayers. However, the sign of the spin Hall angle in Ta is opposite to that of Pt [31]. The spin diffusion length in Pt is $\sim 1.5\,\mathrm{nm}$ [137], which is smaller than the thickness of the $\mathrm{Pt}_{1-x}\mathrm{Bi}_x$ layer. Such short diffusion length indicates that the spin current from the Ta layer is reduced within the $\mathrm{Pt}_{1-x}\mathrm{Bi}_x$ layer before flowing into the Co layer. Thus, we consider the Ta seed layer plays little role in the SOT of $\mathrm{Pt}_{1-x}\mathrm{Bi}_x$/Co heterostructures. The enhancement of ξ_{DL} upon doping Bi is simply due to the increase in the resistivity with larger x. Similar enhancement of ξ_{DL} in Pt by tuning the resistivity has been reported in Pt-Al/Co and Pt-Hf/Co heterostructures [37]. However, the SHC of Pt-Al and Pt-Hf is found to decrease with increasing Al or Hf doping. These results indicate that introducing Bi into Pt provides means to modify the current-spin conversion efficiency in Pt without reducing the intrinsic SHE property.

5.6 Conclusion

In conclusion, we have studied the structure, magnetic anisotropy and current-spin conversion in $\mathrm{Pt}_{1-x}\mathrm{Bi}_x$/Co/MgO trilayer system with different Bi doping level x. Pt and Bi form a solid-solution thin film for $x \leq\sim 0.5$. When x is larger than ~ 0.6, formation of crystalized $P\bar{3}$ PtBi_2 is observed in $\mathrm{Pt}_{1-x}\mathrm{Bi}_x$ thin film in the matrix of Pt. The PMA of an ultrathin Co layer in $\mathrm{Pt}_{1-x}\mathrm{Bi}_x$/Co/MgO trilayer is sensitive to the structure of $\mathrm{Pt}_{1-x}\mathrm{Bi}_x$; the magnetic easy axis of Co layer changes from out-in-plane to in-plane at $x \sim 0.6$. The resistivity of Pt-rich $\mathrm{Pt}_{1-x}\mathrm{Bi}_x$ thin film increases with increasing Bi doping. Nevertheless, the SHC of $\mathrm{Pt}_{1-x}\mathrm{Bi}_x$ remains a constant against the change of x, resulting in an enhancement of the current-spin conversion efficiency in $\mathrm{Pt}_{1-x}\mathrm{Bi}_x$ by increasing x. The value of SHC for Pt-rich $\mathrm{Pt}_{1-x}\mathrm{Bi}_x$ is also consistent with previous studies on Pt, indicating the SOT in $\mathrm{Pt}_{1-x}\mathrm{Bi}_x$/Co for $x \leq\sim 0.5$ is likely attributed to the intrinsic SHE of Pt. These results suggest the doping of Bi is a reliable method to enhance current-spin conversion efficiency in Pt.

Chapter 6

Summary & Outlook

In this thesis, I presented my studies on the characterization of current-induced spin-orbit torque (SOT) in Bi-based material/ferromagnetic metal (FM) heterostructures to estimate the current-spin conversion efficiency.

After a brief introduction (Chap. 1) and description of the experimental methods (Chap. 2), in Chap. 3, I show systematical studies on current-induced SOT in polycrystalline $Bi_{1-x}Sb_x$ alloy/CoFeB thin film heterostructures. The spin Hall conductivity (SHC) of $Bi_{1-x}Sb_x$ increases with increasing $Bi_{1-x}Sb_x$ thickness before it saturates, indicating that the spin Hall effect (SHE) predominantly dominates the current-spin conversion in $Bi_{1-x}Sb_x$. The SHC of $Bi_{1-x}Sb_x$ exhibits a plateau for Bi-rich compositions, i.e., $x \leq 0.35$, and decreases with increasing Sb concentration x. This trend and the value of SHC are consistent with calculations based on a tight-binding model, suggesting the intrinsic contribution is dominant. The SHC is independent of the film facet orientation of $Bi_{1-x}Sb_x$ thin films, implying the topological surface state (TSS) contribution, if present, plays little role in the current-spin conversion. Unexpectedly, the current-spin conversion efficiency (ξ_{DL}) and SHC of $Bi_{1-x}Sb_x$ increase with increasing temperature. For example, the ξ_{DL} of $Bi_{0.83}Sb_{0.17}$ exhibits a twofold enhancement from 5 K to 300 K, reaching ~ 1.2 at room temperature. The enhancement indicates that the thermally-excited massive Dirac electrons in the L valley are responsible for the SHE in Bi-based alloys.

Since the L-valley Dirac-like states are associated with Bi, the effect of Fermi-level positioning on SHC is studied in Bi. These results are presented in Chap. 4. The Fermi level of Bi is controlled by electron and hole doping via Te and Sn substitution. The SHC exhibits a plateau when E_{F} is close to the Dirac point and drops dramatically by increasing electron and hole concentration. These results provide evidence of Fermi level-dependent current-spin conversion in Bi. For pristine Bi with E_{F} close to the Dirac point, the current-spin conversion efficiency reaches a maximum of $\sim$2.7, which is one to two orders of

magnitude larger than that reported in previous studies. The value of SHC in the plateau is consistent with calculations based on the tight-binding model. In addition, the SHC of pristine Bi is shows little dependence on crystallographic orientations and variation in the resistivity. These results further support the notion that the intrinsic SHE, induced by the gapped Dirac band of Bi at the L point, dominates the current-spin conversion in Bi. It should be noted that the SHC of heavily doped Bi decreases monotonically with increasing x. For example, the SHC of Bi_2Te_3 is ~ 40 $(\hbar/e)$ $\Omega^{-1}\cdot\mathrm{cm}^{-1}$, which is in agreement with that of bulk Bi_2Te_3 in previous report, indicating the current-spin conversion is likely not dominated by the TSS of Bi_2Te_3.

In Chap. 5, I discuss the results on the structure, magnetic anisotropy and current-spin conversion in $Pt_{1-x}Bi_x$/Co/MgO trilayers with different Bi doping level x. In Pt-rich $Pt_{1-x}Bi_x$ with $x \leq\sim 0.5$, the film is a Pt-Bi solid solution. In this regime, PMA is found for ultrathin Co layer. Crystallization of $PtBi_2$ is observed for x larger than ~ 0.6 and $Pt_{1-x}Bi_x$ forms a Pt-$PtBi_2$ mixture. The easy axis of the ultrathin Co layer of this phase points along the film plane. The SHC of $Pt_{1-x}Bi_x$ with $x \leq\sim 0.5$ exhibits a plateau against x despite a threefold change in the longitudinal resistivity, resulting in an enhancement of ξ_{DL} with increasing x. The value of SHC in the plateau is in accordance with previous studies on Pt thin films, implying the current-spin conversion in $Pt_{1-x}Bi_x$ originated from the SHE of Pt. These results suggest introducing Bi into Pt is a reliable method to enhance the current-spin conversion efficiency in Pt.

To summarize, I have demonstrated significant current-spin conversion efficiency in BiSb alloy and Bi, unveiling the important role of the electrons Dirac character on the spin Hall effect experimentally for the first time. The non-zero Berry curvature induced by Dirac character gives the transverse anomalous velocity to the electrons, converting charge current into spin current. I have also established a Bi-based system, i.e., $Pt_{1-x}Bi_x$/Co/MgO trilayer, exhibiting PMA and strong current-spin conversion efficiency. These results provide solid understanding on current-spin conversion in materials with Dirac-like carriers. These results open pathways to explore material systems with strong SHE, e.g., Weyl semimetals with broken inversion symmetry and/or time-reversal symmetry.

There are several unsolved issues to be addressed. First, the origin of the field-like spin-orbit torque (FL-SOT) we find in our samples is not well understood. It has been predicted that a Rashba-like effective field in an asymmetric system can generate the FL-SOT [42–46]. This prediction has been confirmed in different systems [109, 142–144]. A careful quantitative characterization of the FL-SOT in Bi(Sb)/FM/oxide trilayer with tunable structural inversion

asymmetry, e.g., varying the oxide layer type, may provide better understanding. Second, the effect of $PtBi_2$ in $Pt_{1-x}Bi_x$/Co/MgO trilayer remain elusive. Whether the Dirac semimetal character of $PtBi_2$ prevails in sputtered polycrystalline thin films and its influence on current-spin conversion is of great interest, both for scientific and technological point of view of topological materials. The structural optimization of $PtBi_2$ thin film and characterization of TSS are required.

Acknowledgments

It is my great pleasure to express my special gratitude to the following people for their kind help during doctoral program.

First of all, I would like to express my deepest gratitude to my supervisor Prof. Masamitsu Hayashi for giving me the chance to study and research in a laboratory with such comfortable environment. I am thankful to him for giving me sufficient freedom to plan my PhD project. Without his kind guidance, valuable advice, and continuous encouragement throughout the three years, my PhD studies would never have been accomplished.

I have to express my great thanks to my Mater supervisor Prof. Atsushi Fujimori, who have guided me to the exciting and splendid world of condensed matter physics. I would like to thank his continuous encouragement throughout my Master and PhD study.

I acknowledge staff members in Hayashi group: Dr. Yong-Chang Lau for his kind guidance on the experimental methods, a lot of advice on data analysis, enlightening discussions and help on the AFM measurement of BiSb alloy thin film samples, Dr. Masashi Kawaguchi for managing all the equipments in the lab and his fruitful discussions on the results.

I am very grateful to Dr. Xiandong Xu, Dr. Tadakatsu Ohkubo, and Dr. Kazuhiro Hono in NIMS for their help on the TEM measurement of BiSb thin film samples.

I would like to thank all the former and current members in the Hayashi group: Mr. Guanxiong Qu, Mr. Yukihiro Marui, Mr. Yuto Ishikuro, Mr. Takuya Kawada, Ms. Hana Hirose, Mr. Hiroki Matsumoto, Mr. Riku Kajiyama and Mr. Shunya Matsumoto. Good luck in the future.

I would like to thank my vice supervisor Prof. Yukitoshi Motome during the four years of MERIT course. His kindness and advice in theory supports my research a lot.

I would like to thank Ms. Mayuko Niwata for dealing with a lot of business stuff and giving me encouragement during the five-year life aboard.

I thank staff members in NIMS: Dr. Seiji Mitani for taking care of me during my stay in NIMS, Dr. Yuya Sakuraba for providing me with the con-

necting box for transport experiments, Dr. Takao Furubayashi for his help on XRD measurement, and Ms. Akiko Tomaru for helping me on the reservation of nap room.

I acknowledge Dr. Toshihiro Kujirai, Dr. Akinori Asahara and Mr. Yu Kitano for taking care of me during the internship in Hitachi.

I would like to thank for the financial support during the four years from the Materials Education program for the future leaders in Research, Industry, and Technology (MERIT) of the MEXT "Program for Leading Graduate Schools" and JSR Fellowship, The University of Tokyo.

Finally, I would like to thank my parents for supporting my student life and research activities.

December 2020

Zhendong Chi

List of publications

1. K. W. Wakabayashi, Y. Nonaka, Y. Takeda, S. Sakamoto, K. Ikeda, **Z. Chi**, G. Shibata, A. Tanaka, Y. Saito, H. Yamagami, M. Tanaka, A. Fujimori, and R. Nakane
   Electronic structure and magnetic properties of magnetically dead layers in epitaxial $CoFe_2O_4/Al_2O_3$ /Si(111) films studied by x-ray magnetic circular dichroism.
   Physical Review B **96**, 104410 (2017)

2. S. Sakamoto, K. Srinivasan, R. Zhang, O. Krupin, K. Ikeda, G. Shibata, Y. Nonaka, **Z. Chi**, M. Sakamaki, K. Amemiya, A. Fujimori, and A. Ajan
   Effects of cobalt sustitution in $L1_0$-(Fe,Co)Pt thin films.
   Physical Review B **96**, 144437 (2017)

3. G. Shibata, M. Kitamura, M. Minohara, K. Yoshimatsu, T. Kadono, K. Ishigami, T. Harano, Y. Takahashi, S. Sakamoto, Y. Nonaka, K. Ikeda, **Z. Chi**, M. Furuse, S. Fuchino, M. Okano, J. -i. Fujihira, A. Uchida, K. Watanabe, H. Fujihira, S. Fujihira, A. Tanaka, H. Kumigashira, T. Koide, and A. Fujimori
   Anisotropic spin-density distribution and magnetic anisotropy of strained $La_{1-x}Sr_xMnO_3$ thin films: Angle-dependent x-ray magnetic circular dichroism.
   npj Quantum Materials **3**, 3 (2018)

4. Y. Nonaka, G. Shibata, R. Koborinai, K. Ishigami, S. Sakamoto, K. Ikeda, **Z. Chi**, T. Koide, A. Tanaka, T. Katsufuji, and A. Fujimori
   Electronic states and possible origin of the orbital-glass state in a nearly metallic spinel cobalt vanadate: An x-ray magnetic circular dichroism study.
   Physical Review B **97**, 205126 (2018)

5. Y. K. Wakabayashi, Y. Nonaka, Y. Takeda, S. Sakamoto, K. Ikeda, **Z. Chi**, G. Shibata, A. Tanaka, Y. Saitoh, H. Yamagami, M. Tanaka,

A. Fujimori, and R. Nakane
Cation distribution and magnetic properties in ultrathin $(Ni_{1-x}Co_x)Fe_2O_4$ (x=0-1) layers on Si(111) studied by soft x-ray magnetic circular dichroism.
Physical Review Materials **2**, 104416 (2018)

6. Y.-C. Lau, **Z. Chi**, T. Taniguchi, M. Kawaguchi, G. Shibata, N. Kawamura, M. Suzuki, S. Fukami, A. Fujimori, H. Ohno, and M. Hayashi
Giant perpendicular magnetic anisotropy in Ir/Co/Pt multilayers.
Physical Review Materials **3**, 104419 (2019)

7. S. Sakamoto, L. D. Anh, P. N. Hai, Y. Takeda, M. Kobayashi, R. Nakane, Y. W. Wakabayashi, Y. Nonaka, K. Ikeda, **Z. Chi**, Y. Wan, M. Suzuki, Y. Saito, H. Yamagami, M. Tanaka, and A. Fujimori
Magnetization Process of the insulation ferromagnetic semiconductor (Al,Fe)Sb.
Physical Review B **101**, 075204 (2020)

8. **Z. Chi**, Y.-C. Lau, X.-D. Xu, T. Ohkubo, K. Hono, and M. Hayashi
The spin Hall effect in Bi-Sb alloys driven by thermal excited Dirac-like electrons.
Science Advances **6**, eaay2324 (2020)

9. M. Kawaguchi, H. Hirose, **Z. Chi**, Y.-C. Lau, F. Freimuth, and M. Hayashi
Giant inverse Faraday effect in Dirac semimetals.
Submitted

10. S. Sakamoto, G. Q. Zhao, G. Shibata, Z. Deng, K. Zhao, B. J. Chen, Y. Nonaka, K. Ikeda, **Z. Chi**, Y.-X. Wan, M. Suzuki, T. Koide, A. Tanaka, S. Maekawa, Y. J. Uemura, C. Q. Jin and A. Fujimori
Anisotropic spin distribution and perpendicular magnetic anisotropy in the layered ferromagnetic semiconductor $(Ba,K)(Zn,Mn)_2As_2$.
Submitted

11. **Z. Chi**, Y.-C. Lau, V. L. Zhang, G. Shibata, S. Sakamoto, Y. Nonaka, K. Ikeda, Y.-X. Wan, Masahiro Suzuki, M. Suzuki-Sakamaki, K. Amemiya, N. Kawamura, M. Mizumaki, Motohiro Suzuki, H.-S. Yang, M. Hayashi, and A. Fujimori
Magnetocrystalline anisotropy, Dzyaloshinskii-Moriya interaction, and orbital moment anisotropy in W/Co/Pt trilayers.
In preparation

12. **Z. Chi**, Y.-C. Lau, M. Kawaguchi, K. Takanashi, and M. Hayashi
    Tunable charge-to-spin conversion in bismuth via Dirac band engineering.
    In preparation

13. **Z. Chi**, Y.-C. Lau, M. Kawaguchi, and M. Hayashi
    Structure, magnetic anisotropy, and spin-orbit torque in $Pt_{1-x}Bi_x$/Co heterostructures.
    In preparation

References

[1] M. N. Baibich, J. M. Broto, A. Fert, F. N. V. Dau, F. Petroff, P. Etienne, G. Creuzet, A. Friederich, and J. Chazelas, Giant Magnetoresistance of (001)Fe/(001)Cr Magnetic Superlattices. *Physical Review Letters* **61**, 2472 (1988).

[2] G. Binasch, P. Grünberg, F. Saurenbach, and W. Zinn, Enhanced magnetoresistance in layered magnetic structures with antiferromagnetic interlayer exchange. *Physical Review B* **39**, 4828(R) (1989).

[3] J. C. Slonczewski, Current-driven excitation of magnetic multilayers. *Journal of Magnetism and Magnetic Materials* **159**, L1-L7 (1996).

[4] L. Berger, Emission of spin waves by a magnetic multilayer traversed by a current. *Physical Review B* **54**, 9353 (1996).

[5] S. Zhang, P. M. Levy, and A. Fert, Mechanisms of Spin-Polarized Current-Driven Magnetization Switching. *Physical Review Letters* **88**, 236601 (2002).

[6] D. C. Ralph and M. D. Stiles, Spin transfer torques. *Journal of Magnetism and Magnetic Materials* **320**, 1190-1216 (2008).

[7] E. B. Myers, D. C. Ralph, J. A. Katine, R. N. Louie, and R. A. Buhrman, Current-Induced Switching of Domains in Magnetic Multilayer Devices. *Science* **285**, 867-870 (1999).

[8] S. Mangin, D. Ravelosona, J. A. Katine, M. J. Carey, B. D. Terris, and E. E. Fullerton, Current-induced magnetization reversal in nanopillars with perpendicular anisotropy. *Nature Materials* **5**, 210-215 (2006).

[9] J. Z. Sun, Spin-current interaction with a monodomain magnetic body: A model study. *Physical Review B* **62**, 570 (2000).

[10] D. A. Allwood, G. Xiong, M. D. Cooke, C. C. Faulkner, D. Atkinson, N. Vernier, and R. P. Cowburn, Submicrometer Ferromagnetic NOT Gate and Shift Register. *Science* **296**, 2003-2006 (2002).

[11] D. Atkinson, D. A. Allwood, G. Xiong, M. D. Cooke, C. C. Faulkner, and R. P. Cowburn, Magnetic domain-wall dynamics in a submicrometre ferromagnetic structure. *Nature Materials* **2**, 85-87 (2003).

[12] A. Yamaguchi, T. Ono, S. Nasu, K. Miyake, K. Mibu, and T. Shinjo, Real-Space Observation of Current-Driven Domain Wall Motion in Submicron MagneticWires. *Physical Review Letters* **92**, 077205 (2004).

[13] F. Cayssol, D. Ravelosona, C. Chappert, J. Ferré, and J. P. Jamet, Domain Wall Creep in Magnetic Wires. *Physical Review Letters* **92**, 107202 (2004).

[14] D. Ravelosona, D. Lacour, J. A. Katine, B. D. Terris, and C. Chappert, Nanometer Scale Observation of High Efficiency Thermally Assisted Current-Driven Domain Wall Depinning. *Physical Review Letters* **95**, 117203 (2005).

[15] M. Hayashi, L. Thomas, R. Moriya, C. Rettner, and S. S. P. Parkin, Current-Controlled Magnetic Domain-Wall Nanowire Shift Register. *Science* **320**, 209-211 (2008).

[16] S. S. P. Parkin, M. Hayashi, and L. Thomas, Magnetic Domain-Wall Racetrack Memory. *Science* **320**, 190 (2008).

[17] J. Sinova, S. O. Valenzuela, J. Wunderlich, C. H. Back, and T. Jungwirth, Spin Hall effects. *Reviews of Modern Physics* **87**, 1213–1260 (2015).

[18] M. I. Dyakonov and V. I. Perel, Possibility of Orienting Electron Spins with Current. *JEPT Letters* **13**, 467 (1971).

[19] J. E. Hirsch, Spin Hall Effect. *Physical Review Letters* **83**, 1834–1837 (1999).

[20] N. Nagaosa, J. Sinova, S. Onoda, A. H. MacDonald, and N. P. Ong, Anomalous Hall effect. *Review of Modern Physics* **82**, 1539 (2010).

[21] M. V. Berry, Quantal Phase Factors Accompanying Adiabatic Changes. *Proceedings of the Royal Society of London A: Mathematical, Physical and Engineering Sciences* **392**, 45-57 (1984).

[22] S. Murakami, N. Nagaosa, and S.-C. Zhang, Dissipationless Quantum Spin Current at Room Temperature. *Science* **301**, 1348-1351 (2003).

[23] J. Sinova, D. Culcer, Q. Niu, N. A. Sinitsyn, T. Jungwirth, and A. H. MacDonald, Universal Intrinsic Spin Hall Effect. *Physical Review Letters* **92**, 126603 (2004).

[24] E. Sagasta, Y. Omori, M. Isasa, M. Gradhand, L. E. Hueso, Y. Niimi, Y. Otani, and F. Casanova, Tuning the spin Hall effect of Pt from the moderately dirty to the super clean regime. *Physical Review B* **94**, 060412(R) (2016).

[25] E. Sagasta, Y. Omori, S. Vélez, R. Llopis, C. Tollan, A. Chuvilin, L. E. Hueso, M. Gradhand, Y. Otani, and F. Casanova, Unveiling the mechanisms of the spin Hall effect in Ta. *Physical Review B* **98**, 060410 (2018).

[26] Y. K. Kato, R. C. Myers, A. C. Gossard, and D. D. Awschalom, Observation of the Spin Hall Effect in Semiconductors. *Science* **306**, 1910-1913 (2004).

[27] E. Saitoh, M. Ueda, M. H, and G. Tatara, Conversion of spin current into charge current at room temperature: Inverse spin Hall effect. *Applied Physics Letters* **88**, 182509 (2006).

[28] S. O. Valenzuela and M. Tinkham, Direct electronic measurement of the spin Hall effect. *Nature* **442**, 176-179 (2006).

[29] I. M. Miron, K. Garello, G. Gaudin, P.-J. Zermatten, M. V. Costache, S. Auffret, S. Bandiera, B. Rodmacq, A. Schuhl, and P. Gambardella, Perpendicular switching of a single ferromagnetic layer induced by inplane current injection. *Nature* **476**, 189 (2011).

[30] L. Liu, C.-F. Pai, Y. Li, H. W. Tseng, D. C. Ralph, and R. A. Buhrman, Spin-Torque Switching with the Giant Spin Hall Effect of Tantalum. *Science* **336**, 555-558 (2012).

[31] T. Tanaka, H. Kontani, M. Naito, T. Naito, D. S. Hirashima, K. Yamada, and J. Inoue, Intrinsic spin Hall effect and orbital Hall effect in 4d and 5d transition metals. *Physical Review B* **77**, 165117 (2008).

[32] L. Liu, T. Moriyama, D. C. Ralph, and R. A. Buhrman, Spin-Torque Ferromagnetic Resonance Induced by the Spin Hall Effect. *Physical Review Letters* **106**, 036601 (2011).

[33] L. Liu, O. J. Lee, T. J. Gudmundsen, D. C. Ralph, and R. A. Buhrman, Current-Induced Switching of Perpendicularly Magnetized Magnetic Layers Using Spin Torque from the Spin Hall Effect. *Physical Review Letters* **106**, 036601 (2011).

[34] C. F. Pai, L. Q. Liu, Y. Li, H. W. Tseng, D. C. Ralph, and R. A. Buhrman, Spin transfer torque devices utilizing the giant spin Hall effect of tungsten. *Applied Physics Letters* **101**, 122404 (2012).

[35] J. Kim, J. Sinha, S. Mitani, M. Hayashi, S. Takahashi, S. Maekawa, M. Yamanouchi, and H. Ohno, Anomalous temperature dependence of current-induced torques in CoFeB/MgO heterostructures with Ta-based underlayers. *Physical Review B* **89**, 174424 (2014).

[36] M.-H. Nguyen, D. C. Ralph, and R. A. Buhrman, Spin torque study of the spin Hall conductivity and spin diffusion length in platinum thin films with varying Resistivity. *Physical Review Letters* **116**, 126601 (2016).

[37] M.-H. Nguyen, M. Zhao, D. C. Ralph, and R. A. Buhrman, Enhanced spin Hall torque efficiency in $Pt_{100-x}Al_x$ and $Pt_{100-x}Hf_x$ alloys arising from the intrinsic spin Hall effect. *Applied Physics Letters* **108**, 242407 (2016).

[38] J. Kim, J. Sinha, M. Hayashi, M. Yamanouchi, S. Fukami, T. Suzuki, S. Mitani, and H. Ohno, Layer thickness dependence of the current-induced effective field vector in Ta|CoFeB|MgO. *Nature Materials* **12**, 240-245 (2013).

[39] K. Garello, I. M. Miron, C. O. Avci, F. Freimuth, Y. Mokrousov, S. Blügel, S. Auffret, O. Boulle, G. Gaudin, and P. Gambardella, Symmetry and magnitude of spin-orbit torques in ferromagnetic heterostructures. *Nature Nanotechnology* **8**, 587–593 (2013).

[40] M. Kawaguchi, K. Shimamura, S. Fukami, F. Matsukura, H. Ohno, T. Moriyama, D. Chiba, and T. Ono, Current-Induced Effective Fields Detected by Magnetotrasport Measurements. *Applied Physics Express* **6**, 113002 (2013).

[41] M. Hayashi, J. Kim, M. Yamanouchi, and H. Ohno, Quantitative characterization of the spin-orbit torque using harmonic Hall voltage measurements. *Physical Review B* **89**, 144425 (2014).

[42] A. Manchon and S. Zhang, Theory of nonequilibrium intrinsic spin torque in a single nanomagnet. *Physical Review B* **78**, 212405 (2008).

[43] A. Manchon and S. Zhang, Theory of spin torque due to spin-orbit coupling. *Physical Review B* **79**, 094422 (2009).

[44] K. Obata and G. Tatara, Current-induced domain wall motion in Rashba spin-orbit system. *Physical Review B* **80**, 214429 (2008).

[45] A. Matos-Abiague and R. L. Rodríguez-Suárez, Spin-orbit coupling mediated spin torque in a single ferromagnetic layer. *Physical Review B* **80**, 094424 (2009).

[46] P. M. Haney, H.-W. Lee, K.-J. Lee, A. Manchon, and M. D. Stiles, Current induced torques and interfacial spin-orbit coupling: Semiclassical modeling.. *Physical Review B* **87**, 174411 (2013).

[47] H. Nakayama, M. Althammer, Y.-T. Chen, K. Uchida, Y. Kajiwara, D. Kikuchi, T. Ohtani, S. Gepraäs, M. Opel, S. Takahashi, R. Gross, G. E. W. Bauer, S. T. B. Goennenwein, and E. Saitoh, Spin Hall magnetoresistance induced by a nonequilibrium Proximity Effect. *Physical Review Letters* **110**, 206601 (2013).

[48] J. C. Rojas-Sánchez, N. Reyren, P. Laczkowski, W. Savero, J. P. Attane, C. Deranlot, M. Jamet, J. M. George, L. Vila, and H. Jaffres, Spin Pumping and Inverse Spin Hall Effect in Platinum: The Essential Role of Spin-Memory Loss at Metallic Interfaces. *Physical Review Letters* **112**, 106602 (2014).

[49] Y. T. Chen, S. Takahashi, H. Nakayama, M. Althammer, S. T. B. Goennenwein, E. Saitoh, and G. E. W. Bauer, Theory of spin Hall magnetoresistance. *Physical Review B* **87**, 144411 (2013).

[50] L. Q. Liu, C. F. Pai, D. C. Ralph, and R. A. Buhrman, Magnetic Oscillations Driven by the Spin Hall Effect in 3-Terminal Magnetic Tunnel Junction Devices. *Physical Review Letters* **109**, 186602 (2012).

[51] J. Kim, P. Sheng, S. Takahashi, S. Mitani, and M. Hayashi, Spin Hall Magnetoresistance in Metallic Bilayers. *Physical Review Letters* **116**, 097201 (2016).

[52] Y. L. Chen, J.-H. Chu, J. G. Analytis, Z. K. Liu, K. Igarashi, H.-H. Kuo, X. L. Qi, S. K. Mo, R. G. Moore, D. H. Lu, M. Hashimoto, T. Sasagawa, S. C. Zhang, I. R. Fisher, Z. Hussain, and Z. X. Shen, Massive Dirac Fermion on the Surface of a Magnetically Doped Topological Insulator. *Science* **329**, 659-662 (2010).

[53] D. Hsieh, Y. Xia, D. Qian, L. Wray, J. H. Dil, F. Meier, J. Osterwalder, L. Patthey, J. G. Checkelsky, N. P. Ong, A. V. Fedorov, H. Lin, A. Bansil, D. Grauer, Y. S. Hor, R. J. Cava, and M. Z. Hasan, A tunable topological insulator in the spin helical Dirac transport regime. *Nature* **460**, 11011105 (2009).

[54] M. Z. Hasan, Colloquium: Topological insulators. *Review of Modern Physics* **82**, 3045 (2010).

[55] X.-L. Qi and S.-C. Zhang, Topological insulators and superconductors. *Review of Modern Physics* **83**, 1057 (2011).

[56] A. A. Burkov and D. G. Hawthorn, Spin and charge transport on the surface of a topological insulator. *Physical Review Letters* **105**, 066802 (2010).

[57] D. Culcer, E. H. Hwang, T. D. Stanescu, and S. Das Sarma, Two-dimensional surface charge transport in topological insulators. *Physical Review B* **82**, 155457 (2010).

[58] D. Pesin and A. H. MacDonald, Spintronics and pseudospintronics in graphene and topological insulators. *Nature Materials* **11**, 409-416 (2012).

[59] M. H. Fischer, A. Vaezi, A. Manchon, and E.-A. Kim, Spin-torque generation in topological insulator based heterostructures. *Physical Review B* **93**, 125303 (2016).

[60] X.-L. Qi, T. L. Hughes, and S.-C. Zhang, Topological field theory of time-reversal invariant insulators. *Physical Review B* **78**, 195424 (2008).

[61] H. Zhang, C.-X. Liu, X.-L. Qi, X. Dai, Z. Fang, and S.-C. Zhang, Topological insulators in Bi_2Se_3, Bi_2Te_3 and Sb_2Te_3 with a single Dirac cone on the surface. *Nature Physics* **5**, 438-442 (2009).

[62] C.-X. Liu, X.-L. Qi, H. Zhang, X. Dai, Z. Fang, and S.-C. Zhang, Model Hamiltonian for topological insulators. *Physical Review B* **82**, 045122 (2010).

[63] D. Hsieh, D. Qian, L. Wray, Y. Xia, Y. S. Hor, R. J. Cava, and M. Z. Hasan, A topological Dirac insulator in a quantum spin Hall phase. *Nature* **452**, 970-974 (2008).

[64] D. Hsieh, Y. Xia, L. Wray, D. Qian, A. Pal, J. H. Dil, J. Osterwalder, F. Meier, G. Bihlmayer, C. L. Kane, Y. S. Hor, R. J. Cava, and M. Z. Hasan, Observation of Unconventional Quantum Spin Textures in Topological Insulators. *Science* **323**, 919-922 (2009).

[65] Y. L. Chen, J. G. Analytis, J.-H. Chu, Z. K. Liu, S.-K. Mo, X. L. Qi, H. J. Zhang, D. H. Lu, X. Dai, Z. Fang, S. C. Zhang, I. R. Fisher, Z. Hussain, and Z.-X. Shen, Experimental Realization of a Three-Dimensional Topological Insulator, Bi2Te3. *Science* **325**, 178-181 (2009).

[66] Y. Xia, D. Qian, D. Hsieh, L. Wray, A. Pal, H. Lin, A. Bansil, D. Grauer, Y. S. Hor, R. J. Cava, and M. Z. Hasan, Observation of a large-gap topological-insulator class with a single Dirac cone on the surface. *Nature Physics* **5**, 398402 (2009).

[67] D. Hsieh, Y. Xia, D. Qian, L. Wray, F. Meier, J. H. Dil, J. Osterwalder, L. Patthey, A. V. Fedorov, H. Lin, A. Bansil, D. Grauer, Y. S. Hor, R. J. Cava, and M. Z. Hasan, Observation of Time-Reversal-Protected Single-Dirac-Cone Topological-Insulator States in Bi_2Te_3 and Sb_2Te_3. *Physical Review Letters* **103**, 146401 (2009).

[68] S.-Y. Xu, Y. Xia, L. A. Wray, S. Jia, F. Meier, J. H. Dil, J. Osterwalder, B. Slomski, A. Bansil, H. Lin, R. J. Cava, and M. Z. Hasan, Topological Phase Transition and Texture Inversion in a Tunable Topological Insulator. *Science* **332**, 560-564 (2011).

[69] Z.-H. Pan, E. Vescovo, A. V. Fedorov, D. Gardner, Y. S. Lee, S. Chu, G. D. Gu, and T. Valla, Electronic Structure of the Topological Insulator Bi_2Se_3 Using Angle- Resolved Photoemission Spectroscopy: Evidence for a Nearly Full Surface Spin Polarization. *Physical Review Letters* **106**, 257004 (2011).

[70] Y. A. Bychkov and E. I. Rashba, Properties of a 2D electron gas with a lifted spectrum degeneracy. *JETP Letter* **39**, 78-81 (1984).

[71] V. M. Edelstein, Spin polarization of conduction electrons induced by electric current in two-dimensional asymmetric electron systems. *Solid State Communications* **73**, 233-235 (1990).

[72] J. Han, A. Richardella, S. A. Siddiqui, J. Finley, N. Samarth, and L. Liu, Room-Temperature Spin-Orbit Torque Switching Induced by a Topological Insulator. *Physical Review Letters* **119**, 077702 (2017).

[73] K. Yasuda, A. Tsukazaki, R. Yoshimi, K. Kondou, K. S. Takahashi, Y. Otani, M. Kawasaki, and Y. Tokura, Current-Nonlinear Hall Effect and Spin-Orbit Torque Magnetization Switching in a Magnetic Topological Insulator. *Phys. Rev. Lett.* **119**, 137204 (2017).

[74] A. R. Mellnik, J. S. Lee, A. Richardella, J. L. Grab, P. J. Mintun, M. H. Fischer, A. Vaezi, A. Manchon, E.-A. Kim, N. Samarth, and D. C. Ralph, Spin-transfer torque generated by a topological insulator. *Nature* **511**, 449–451 (2014).

[75] Y. Fan, P. Upadhyaya, X. Kou, M. L. S. Takei, Z. Wang, J. Tang, L. He, L.-T. Chang, M. M. G. Yu, W. Jiang, T. Nie, R. N. Schwartz, Y. Tserkovnyak, and K. L. Wang, Magnetization switching through giant spinorbit torque in a magnetically doped topological insulator heterostructure. *Nature Materials* **13**, 699-704 (2014).

[76] K. Kondou, R. Yoshimi, A. Tsukazaki, Y. Fukuma, J. Matsuno, K. S. Takahashi, M. Kawasaki, Y. Tokura, and Y. Otani, Fermi-level-dependent charge-to-spin current conversion by Dirac surface states of topological insulators. *Nature Physics* **12**, 1027-1031 (2016).

[77] Y. Wang, D. Zhu, Y. Wu, Y. Yang, J. Yu, R. Ramaswamy, R. Mishra, S. Shi, M. Elyasi, K.-L. Teo, Y. Wu, and H. Yang, Room temperature magnetization switching in topological insulator-ferromagnet heterostructures by spin-orbit torques. *Nature Communications* **8**, 1364 (2017).

[78] Y. F. Li, Q. L. Ma, S. X. Huang, and C. L. Chien, Thin films of topological Kondo insulator candidate SmB6: Strong spin-orbit torque without exclusive surface conduction. *Science Advances* **4**, eaap8294 (2018).

[79] M. DC, R. Grassi, J.-Y. Chen, M. Jamali, D. R. Hickey, D. Zhang, Z. Zhao, H. Li, P. Quarterman, Y. Lv, M. Li, A. Manchon, K. A. Mkhoyan, T. Low, and J.-P. Wang, Room-temperature high spin-orbit torque due to quantum confinement in sputtered $Bi_xSe_{(1-x)}$ films. *Nature Materials* **17**, 800-807 (2018).

[80] P. de Marcillac, N. Coron, G. Dambier, J. Leblanc, and J.-P. Moalic, Experimental detection of α-particles from the radioactive decay of natural bismuth. *Nature* **422**, 876-878 (2003).

[81] Y. Fuseya, M. Ogata, and H. Fukuyama, Transport Properties and Diamagnetism of Dirac Electrons in Bismuth. *Journal of the Physical Society of Japan* **84**, 012001 (2015).

[82] J. P. Michenaud and J. P. Issi, Electron and hole transport in bismuth. *Journal of Physics Part C Solid State Physics* **5**, 3061-3072 (1972).

[83] P. A. Wolff, Matrix elements and selection rules for the two-band model of bismuth. *Journal of Physics and Chemistry of Solids* **25**, 1057-1068 (1964).

[84] M. P. Vecchi, J. R. Pereira, and M. S. Dresselhaus, Anomalies in the magnetoreflection spectrum of bismuth in the low-quantum-number limit. *Physical Review B* **14**, 298 (1976).

[85] Z. Zhu, B. Fauque, Y. Fuseya, and K. Behnia, Angle-resolved Landau spectrum of electrons and holes in bismuth. *Physical Review B* **84**, 115137 (2011).

[86] Y. Fuseya, M. Ogata, and H. Fukuyama, Spin-Hall Effect and Diamagnetism of Dirac Electrons. *Journal of the Physical Society of Japan* **81**, 093704 (2012).

[87] T. Fukazawa, H. Kohno, and J. Fujimoto, Intrinsic and Extrinsic Spin Hall Effects of Dirac Electrons. *Journal of the Physical Society of Japan* **86**, 094704 (2017).

[88] C. Sahin and M. E. Flatté, Tunable Giant Spin Hall Conductivities in a Strong Spin-Orbit Semimetal: $Bi_{1-x}Sb_x$. *Physical Review Letters* **114**, 107201 (2015).

[89] D. Hou, Z. Qiu, K. Harii, Y. Kajiwara, K. Uchida, Y. Fujikawa, H. Nakayama, T. Yoshino, T. An, K. Ando, X. Jin, and E. Saitoh, Interface induced inverse spin Hall effect in bismuth/permalloy bilayer. *Applied Physics Letters* **101**, 042403 (2012).

[90] H. Emoto, Y. Ando, G. Eguchi, R. Ohshima, E. Shikoh, Y. Fuseya, T. Shinjo, and M. Shiraishi, Transport and spin conversion of multicarriers in semimetal bismuth. *Physical Review B* **93**, 174428 (2016).

[91] M. Matsushima, S. Miwa, S. Sakamoto, T. Shinjo, R. Ohshima, Y. Ando, Y. Fuseya, and M. Shiraishi, Sizable spin-transfer torque in the $Bi/Ni_{80}Fe_{20}$ bilayer film. *Applied Physics Letters* **117**, 042407 (2020).

[92] D. Yue, W. Lin, J. Li, X. Jin, and C. L. Chien, Spin-to-Charge Conversion in Bi Films and Bi/Ag Bilayers. *Physical Review Letters* **121**, 037201 (2018).

[93] Y.Feutelais, G.Morgant, J.R.Didry, and J.Schnitter, Thermodynamic evaluation of the system bismuth-antimony. *Calphad* **16**, 111-119 (1992).

[94] L. Fu and C. L. Kane, Topological insulators with inversion symmetry. *Physical Review B* **76**, 045302 (2007).

[95] A. Nishide, A. A. Taskin, Y. Takeichi, T. Okuda, A. Kakizaki, T. Hirahara, K. Nakatsuji, F. Komori, Y. Ando, and I. Matsuda, Direct mapping of the spin-filtered surface bands of a three-dimensional quantum spin Hall insulator. *Physical Review B* **81**, 041309(R) (2010).

[96] J. C. Y. Teo, L. Fu, and C. L. Kane, Surface states and topological invariants in three-dimensional topological insulators: Application to $Bi_{1-x}Sb_x$. *Physical Review B* **78**, 045426 (2008).

[97] H.-J. Zhang, C.-X. Liu, X.-L. Qi, X.-Y. Deng, X. Dai, S.-C. Zhang, and Z. Fang, Electronic structures and surface states of the topological insulator $Bi_{1-x}Sb_x$. *Physical Review B* **80**, 085307 (2009).

[98] N. H. D. Khang, Y. Ueda, and P. N. Hai, A conductive topological insulator with large spin Hall effect for ultralow power spin-orbit torque switching. *Nature Materials* **17**, 808-813 (2018).

[99] N. Roschewsky, E. S. Walker, P. Gowtham, S. Muschinske, F. Hellman, S. R. Bank, and S. Salahuddin, Spin-Orbit Torque and Nernst Effect in Bi-Sb/Co Heterostructures. *Physical Review B* **99**, 195103 (2019).

[100] A. Manchon, S. Pizzini, J. Vogel, V. Uhlîr, L. Lombard, C. Ducruet, S. Auffret, B. Rodmacq, B. Dieny, M. Hochstrasser, and G. Panaccione, X-ray analysis of the magnetic influence of Pt/Co/AlO_x in trilayers. *Journal of Applied Physics* **103**, 07A912 (2008).

[101] A. Manchon, C. Ducruet, L. Lombard, S. Auffret, B. Rodmacq, B. Dieny, S. Pizzini, J. Vogel, V. Uhlîr, M. Hochstrasser, , and G. Panaccione, Analysis of oxygen induced anisotropy Pt/Co/MO_x crossover in trilayers. *Journal of Applied Physics* **104**, 043914 (2008).

[102] A. Manchon, S. Pizzini, J. Vogel, V. Uhlîr, L. Lombard, C. Ducruet, S. Auffret, B. Rodmacq, B. Dieny, M. Hochstrasser, and G. Panaccione, X-ray analysis of oxygen-induced perpendicular magnetic anisotropy in Pt/Co/AlO_x trilayers. *Journal of Magnetism and Magnetic Materials* **320**, 1889-1892 (2008).

[103] C. O. Avci, K. Garello, M. Gabureac, A. Ghosh, A. Fuhrer, S. F. Alvarado, and P. Gambardella, Interplay of spin-orbit torque and thermoelectric effects in ferromagnet/normal-metal bilayers. *Physical Review B* **90**, 224427 (2014).

[104] Y.-C. Lau and M. Hayashi, Spin torque efficiency of Ta, W, and Pt in metallic bilayers evaluated by harmonic Hall and spin Hall magnetoresistance measurements. *Japanese Journal of Applied Physics* **56**, 0802B5 (2017).

[105] X. D. Xu, K. Mukaiyama, S. Kasai, T. Ohkubo, and K. Hono, Impact of boron diffusion at MgO grain boundaries on magneto transport properties of MgO/CoFeB/W magnetic tunnel junctions. *Acta Materialia* **161**, 360-366 (2018).

[106] S. Cho, S. H. C. Baek, K. D. Lee, Y. Jo, and B. G. Park, Large spin Hall magnetoresistance and its correlation to the spin-orbit torque in W/CoFeB/MgO structures. *Scientific Reports* **5**, 14668 (2015).

[107] A. Hoffmann, Spin Hall Effects in Metals. *IEEE Transactions on Magnetics* **49**, 5172-5193 (2013).

[108] Y. Shiomi, K. Nomura, Y. Kajiwara, K. Eto, M. Novak, K. Segawa, Y. Ando, and E. Saitoh, Spin-Electricity Conversion Induced by Spin Injection into Topological Insulators. *Physical Review Letters* **113**, 196601 (2014).

[109] Y. Ou, C.-F. Pai, S. Shi, D. C. Ralph, and R. A. Buhrman, Origin of fieldlike spin-orbit torques in heavy metal/ferromagnet/oxide thin film heterostructures. *Physical Review B* **94**, 140414 (2016).

[110] W. M. Yim and A. Amith, Bi-Sb alloys for magneto-thermoelectric and thermomagnetic cooling. *Solid-State Electronics* **15**, 1141-1144 (1972).

[111] J. Sinha, M. Hayashi, A. J. Kellock, S. Fukami, M. Yamanouchi, M. Sato, S. Ikeda, S. Mitani, S. H. Yang, S. S. P. Parkin, and H. Ohno, Enhanced interface perpendicular magnetic anisotropy in Ta|CoFeB|MgO using nitrogen doped Ta underlayers. *Applied Physics Letters* **102**, 242405 (2013).

[112] X.-G. Zhu and P. Hoffmann, Topological surface states on $Bi_{1-x}Sb_x$: Dependence on surface orientation, termination, and stability. *Physical Review B* **89**, 125402 (2014).

[113] Q. Hao and G. Xiao, Giant spin Hall effect and magnetotransport in a Ta/CoFeB/MgO layered structure: A temperature dependence study. *Physical Review B* **91**, 224413 (2015).

[114] Z. W. Zhu, B. Fauque, K. Behnia, and Y. Fuseya, Magnetoresistance and valley degree of freedom in bulk bismuth. *Journal of Physics: Condensed Matter* **30**, 313001 (2018).

[115] M. N. Ali, J. Xiong, S. Flynn, J. Tao, Q. D. Gibson, L. M. Schoop, T. Liang, N. Haldolaarachchige, M. Hirschberger, N. P. Ong, and R. J.

Cava, Large, non-saturating magnetoresistance in WTe_2. *Nature* **514**, 205-208 (2014).

[116] F. Komori, S. Kobayashi, and W. Sasaki, The anti-localization effect in Bi thin films. *Journal of the Physical Society of Japan* **52**, 368-371 (1983).

[117] O. Oktu and G. A. Saunders, Galvanomagnetic properties of single-crystal antimony between 77 K and 273 K. *Proceedings of the Physical Society of London* **91**, 156-168 (1967).

[118] W.-L. Lee, S. Watauchi, V. L. Miller, R. J. Cava, and N. P. Ong, Dissipationless Anomalous Hall Current in the Ferromagnetic Spinel $CuCr_2Se_{4-x}Br_x$. *Science* **303**, 1647–1649 (2004).

[119] W.-K. Tse and S. Das Sarma, Spin Hall Effect in Doped Semiconductor Structures. *Physical Review Letters* **96**, 056601 (2006).

[120] B. Lenoir, H. Scherrer, and T. Caillat, in *Recent Trends in Thermoelectric Materials Research I*, Vol. 69 of *Semiconductors and Semimetals*, edited by T. M. Tritt (Elsevier, 2001), pp. 101 – 137.

[121] Y. Liu and R. E. Allen, Electronic-structure of the semimetals Bi and Sb. *Physical Review B* **52**, 1566-1577 (1995).

[122] G. Y. Guo, S. Murakami, T. W. Chen, and N. Nagaosa, Intrinsic Spin Hall Effect in Platinum: First-Principles Calculations. *Physical Review Letters* **100**, 096401 (2008).

[123] S. Cho, A. DiVenere, G. K. Wong, J. B. Ketterson, and J. R. Meyer, Thermoelectric transport properties of n-doped and p-doped $Bi_{0.91}Sb_{0.09}$ alloy thin films. *Journal of Applied Physics* **85**, 3655-3660 (1999).

[124] H. Okamoto, *Phase Diagram for Binary Alloys* (ASM, 2000), Vol. 315.

[125] E. Clementi, D. L. Raimondi, and W. P. Reinhardt, Atomic Screening Constants from SCF Functions. II. Atoms with 37 to 86 Electrons. *The Journal of Chemical Physics* **47**, 1300-1307 (1967).

[126] L. Ye, M. Kang, J. Liu, F. von Cube, C. R. Wicker, T. Suzuki, C. Jozwiak, A. Bostwick, E. Rotenberg, D. C. Bell, L. Fu, R. Comin, and J. G. Checkelsky, Massive Dirac fermions in a ferromagnetic kagome metal. *Nature* **555**, 638-642 (2018).

[127] H. Wu, P. Zhang, P. Deng, Q. Lan, Q. Pan, S. A. Razavi, X. Che, L. Huang, B. Dai, K. Wong, X. Han, and K. L. Wang, Room-Temperature Spin-Orbit Torque from Topological Surface States. *Physical Review Letters* **123**, 207205 (2019).

[128] S. Peng, W. Zhao, J. Qiao, L. Su, J. Zhou, H. Yang, Q. Zhang, Y. Zhang, C. Grezes, P. K. Amiri, and K. L. Wang, Giant interfacial perpendicular magnetic anisotropy in MgO/CoFe/capping layer structures. *Applied Physics Letters* **110**, 072403 (2017).

[129] D. Weller, Y. Wu, J. Stöhr, M. G. Samant, B. D. Hermsmeier, and C. Chappert, Orbital magnetic moments of Co in multilayers with perpendicular magnetic anisotropy. *Physical Review B* **49**, 12888 (1994).

[130] N. Nakajima, T. Koide, T. Shidara, H. Miyauchi, H. Fukutani, A. Fujimori, K. Iio, T. Katayama, M. Nývlt, and Y. Suzuki, Perpendicular Magnetic Anisotropy Caused by Interfacial Hybridization via Enhanced Orbital Moment in Co/Pt Multilayers: Magnetic Circular X-Ray Dichroism Study. *Physical Review Letters* **81**, 5229 (1998).

[131] Q. D. Gibson, L. M. Schoop, L. Muechler, L. S. Xie, M. Hirschberger, N. P. Ong, R. Car, and R. J. Cava, Three-dimensional Dirac semimetals: Design principles and predictions of new materials. *Physical Review B* **91**, 205128 (2015).

[132] S. Thirupathaiah, Y. Kushnirenko, E. Haubold, A. V. Fedorov, E. D. L. Rienks, T. K. Kim, A. N. Yaresko, C. G. F. Blum, S. Aswartham, B. Bchner, and S. V. Borisenko, Possible origin of linear magnetoresistance: Observation of Dirac surface states in layered $PtBi_2$. *Physical Review B* **97**, 035133 (2018).

[133] S. Monso, B. Rodmacq, S. Auffret, G. Casali, F. Fettar, B. Gilles, B. Dieny, and P. Boyer, Crossover from in-plane to perpendicular anisotropy in Pt/CoFe/AlO_x sandwiches as a function of Al oxidation: A very accurate control of the oxidation of tunnel barriers. *Applied Physics Letters* **80**, 4157 (2002).

[134] B. Rodmacq, S. Auffret, and B. Dieny, Crossovers from in-plane to perpendicular anisotropy in magnetic tunnel junctions as a function of the barrier degree of oxidation. *Journal of Applied Physics* **93**, 7513 (2003).

[135] V. Vlaminck, J. E. Pearson, S. D. Bader, and A. Hoffmann, Dependence of spin-pumping spin Hall effect measurements on layer thicknesses and stacking order. *Physical Review B* **88**, 064414 (2013).

[136] X. Yang, H. Bai, Z. Wang, Y. Li, Q. Chen, J. Chen, Y. Li, C. Feng, Y. Zheng, and Z. an Xu, Giant linear magneto-resistance in nonmagnetic $PtBi_2$. *Applied Physics Letters* **108**, 252401 (2016).

[137] Y. Wang, P. Deorani, X. P. Qiu, J. H. Kwon, and H. S. Yang, Determination of intrinsic spin Hall angle in Pt. *Applied Physics Letters* **105**, 152412 (2014).

[138] S. Emori, U. Bauer, S.-M. Ahn, E. Martinez, and G. S. D. Beach, Current-driven dynamics of chiral ferromagnetic domain walls. *Nature Materials* **12**, 611 (2013).

[139] N. P. Armitage, E. J. Mele, and A. Vishwanath, Weyl and Dirac semimetals in three-dimensional solids. *Rev. Mod. Phys.* **90**, 015001 (2018).

[140] P. Li, W. Wu, Y. Wen, C. Zhang, J. Zhang, S. Zhang, Z. Yu, S. A. Yang, A. Manchon, and X. xiang Zhang, Spin-momentum locking and spin-orbit torques in magnetic nano-heterojunctions composed of Weyl semimetal WTe_2. *Nature Communication* **9**, 3990 (2018).

[141] B.-C. Lin, S. Wang, A.-Q. Wang, Y. Li, R.-R. Li, K. Xia, D. Yu, and Z.-M. Liao, Electric Control of Fermi Arc Spin Transport in Individual Topological Semimetal Nanowires. *Physical Review Letters* **124**, 116802 (2020).

[142] A. Chernyshov, M. Overby, X. Liu, J. K. Furdyna, Y. Lyanda-Geller, and L. P. Rokhinson, Evidence for reversible control of magnetization in a ferromagnetic material by means of spinorbit magnetic field. *Nature Physics* **5**, 656-659 (2007).

[143] I. M. Miron, G. Gaudin, S. Auffret, B. Rodmacq, A. Schuhl, S. Pizzini, J. Vogel, and P. Gambardella, Current-driven spin torque induced by the Rashba effect in a ferromagnetic metal layer. *Nature Materials* **9**, 230-234 (2010).

[144] S. Emori, T. Nan, A. M. Belkessam, X. Wang, A. D. Matyushov, C. J. Babroski, Y. Gao, H. Lin, and N. X. Sun, Interfacial spin-orbit torque without bulk spin-orbit coupling. *Physical Review B* **93**, 180402(R) (2016).